

## APPENDIX. DATA ANALYSIS

### Supplemental A Material

Magnetotelluric data analysis and borehole electrical geophysical data used to support two- and three-dimensional resistivity modeling appearing in Rodriguez and Sawyer (this volume) follow below.

TABLE A1. APPENDIX FIGURE INDEX

Figures	Description	Profiles
A1-A5	Station plots of observed vs. 2D profile model data	A-A' thru E-E'
A6-A10	Profile plots of tipper strike values	A-A' thru E-E'
A11-A13	2D resistivity profile models with lithologic interpretation.	A-A' thru C-C'
A14-A16	Resistivity sections extracted from 3D forward model	A-A' thru C-C'
A17-A18	2D resistivity profile models with lithologic interpretation.	D-D' and E-E'
A19-A21	Station plots of observed vs. 3D forward model data	A-A'
A22	Station plots of observed vs. 3D forward model data	B-B'
A23-A25	Station plots of observed vs. 3D forward model data	C-C'
A26-A30	Station plots of observed vs. impedance components for 3D inversion	A-A' thru C-C'*
A31-A33	Resistivity sections extracted from 3D inversion	A-A' thru C-C'
A34-A61	Resistivity logs for wells**	not applicable

Notes: \*Data for station 29 from B-B' and station 30 from C-C' were not included in the inversion.

\*\* Figures A53-A55 are oversized and appear in a separate file.

### Magnetotelluric Data Processing

Thirty-eight magnetotelluric soundings (Williams and Rodriguez, 2003a; 2003b; 2005a; 2005b; 2006) along five profiles (Table A2) were acquired between 1999 and 2004 in the study area.

TABLE A2. MAGNETOTELLURIC SOUNDINGS

Station	Longitude	Latitude	UTM N (m)	UTM E (m)	Elevation (m)
<b><u>Profile A-A'</u></b>					
4	-106:12:09	35:35:09	3938490	391060	1905
20	-106:11:36	35:36:16	3940539	391897	1965
8	-106:12:08	35:37:25	3942655	391127	2015
21	-106:11:52	35:38:16	3944249	391560	2015
11	-106:11:19	35:38:47	3945184	392391	2025
5	-106:10:41	35:39:41	3946820	393370	2050
25	-106:10:09	35:40:42	3948914	394185	2100
10	-106:10:05	35:41:53	3950901	394319	2160
23	-106:09:58	35:42:48	3952588	394527	2105
22	-106:09:31	35:43:35	3954039	395225	2040
9	-106:09:31	35:44:24	3955517	395221	2020
27	-106:09:22	35:47:06	3960730	395460	2010
<b><u>Profile B-B'</u></b>					
29	-106:13:34	35:38:09	3944059	388978	1989
14	-106:13:31	35:40:20	3948096	389104	2100
28	-106:13:38	35:42:09	3951444	388978	2037
15	-106:13:43	35:44:37	3956023	388902	2047
<b><u>Profile C-C'</u></b>					
35	-106:28:31	35:49:35	3965476	366739	2767
34	-106:26:18	35:49:38	3965540	370093	2678
33	-106:25:26	35:47:56	3962360	371350	2618
32	-106:24:45	35:47:02	3960693	372338	2535
12	-106:23:20	35:46:03	3958861	374449	2379
31	-106:24:37	35:43:50	3954777	372461	2255
30	-106:23:37	35:42:52	3952970	373947	2073
36	-106:23:00	35:42:40	3952577	374863	2005
17	-106:21:42	35:41:09	3949770	376785	1755
<b><u>Profile D-D'</u></b>					
1	-106:02:02	35:56:50	3978396	406745	1788
3	-105:55:03	35:56:09	3977013	417246	2102
2	-105:48:29	35:59:23	3982900	427161	2498
<b><u>Profile E-E'</u></b>					
E9	-106:41:49	34:45:24	3847169	344680	1486
E10	-106:37:48	34:44:53	3846128	350793	1541
E6	-106:34:39	34:45:32	3847231	355613	1596
E5	-106:34:09	34:45:32	3847226	356384	1603
E4	-106:33:40	34:45:32	3847206	357118	1611
E3	-106:33:13	34:45:38	3847393	357810	1625
E2	-106:32:43	34:45:32	3847188	358562	1645
E1	-106:32:13	34:45:32	3847181	359334	1662
E8	-106:30:14	34:45:21	3846803	362362	1722
E7	-106:28:19	34:45:23	3846813	365278	1866

Notes: Coordinates are referenced to the 1866 Clarke spheroid and North American 1927 Western United States datum (NAD27). Longitude and Latitude format is degrees:minutes:seconds. Universal Transverse Mercator (UTM) North (N) and East (E) units are in Zone 13.

The recorded time-series data are transformed to the frequency domain and processed to determine the impedance tensor, which is used to derive apparent resistivities and phases at each site. A  $1 \times 2$  tensor  $K_z$  relates the vertical ( $H_z$ ) and horizontal ( $H_j$ ) magnetic fields through

$$[H_z] = [K_z] [H_j] \quad (1)$$

For current flow predominantly parallel to the regional strike (x-axis),  $K_{zx} = 0$  for a 2-D Earth or will be a minimum for a 3-D Earth, while  $K_{zy}$  will maximize perpendicular to the regional strike (Wannamaker et al., 2002).  $K_{zy}$  is commonly referred to as the tipper direction and will have an azimuth, in the horizontal plane, in the direction of most rapid conductivity variation (Jones and Vozoff, 1978; Jupp and Vozoff, 1976; Romo et al., 1999).

Typically, for a profile that crosses subperpendicular to the 2-D geologic strike, the observed data are all rotated perpendicular to the profile direction. However, when the observed data indicate a 3-D electromagnetic response (see [Resistivity Profile Models](#) section below) rotating the observed data to match the tipper strike is best when approximating 3-D resistors and conductors with 2-D resistivity profile models while inverting only the transverse magnetic data even when the dominant tipper strike direction is subparallel to the profile orientation (Wannamaker et al., 2002). The observed data (Figs. [A1 to A5](#)) are rotated to match the dominant tipper strike direction along each profile (Figs. [A6 to A10](#)), so that propagation modes for the signals are decoupled into transverse electric and transverse magnetic modes. The dominant tipper strike direction in this part of the Rio Grande rift (Figs. [A6 to A10](#)) is NNE-SSW. Magnetotelluric profiles C-C', D-D', and E-E' are oriented (Fig. 1) subperpendicular to the dominant tipper strike direction (Figs. [A8 to A10](#)), whereas profiles A-A' and B-B' are subparallel to the strike direction (Figs. [A6 and A7](#)).

For profiles C-C', D-D', and E-E', the data are rotated perpendicular to the profile azimuth, while the data for profiles A-A' and B-B' are rotated parallel to the profile azimuth. For profile A-A', magnetotelluric stations 8, 9, 20, and 22 have dominant subperpendicular, E-W, tipper strikes (Fig. [A6](#)) from a conductor below the near-surface resistor (Fig. [A1A](#)). For profile B-B', magnetotelluric stations 15 and 28 have dominant subperpendicular, E-W, tipper strikes (Fig. [A7](#)) confined to lowest frequencies correlating with the base of the conductor (Fig. [A3A](#)). For profile C-C', magnetotelluric stations 12, 17, 31, 32, and 33 have dominant subparallel, NNW-SSE, tipper strikes (Fig. [A8](#)) from the conductor below the near-surface resistor (Fig. [A3A](#)). For profile D-D', magnetotelluric stations 1, 2, and 3 have dominant subparallel, ENE-WSW, tipper strikes (Fig. [A9](#)) from the shallow conductor and resistor (Fig. [A4A](#)). For profile E-E', magnetotelluric stations 1, 4, 5, and 10 have dominant subparallel, ESE-WNW, tipper strikes (Fig. [A10](#)) from the shallow conductor (Fig. [A5A](#)). Stations 3, 4, and 7 also have dominant subparallel tipper strikes at the top of the resistor. We also sorted cross-power files to select optimal signal-to-noise data sets.

## Resistivity Profile Models

The magnetotelluric data were initially inverted using a 2-D inversion of the transverse magnetic mode using the computer algorithm RLM2DI (Mackie et al., 1997; Rodi and Mackie, 2001). The results of the RLM2DI inversion were used as the initial input model for forward modeling using a 2-D finite-element resistivity algorithm (Wannamaker et al., 1985) called

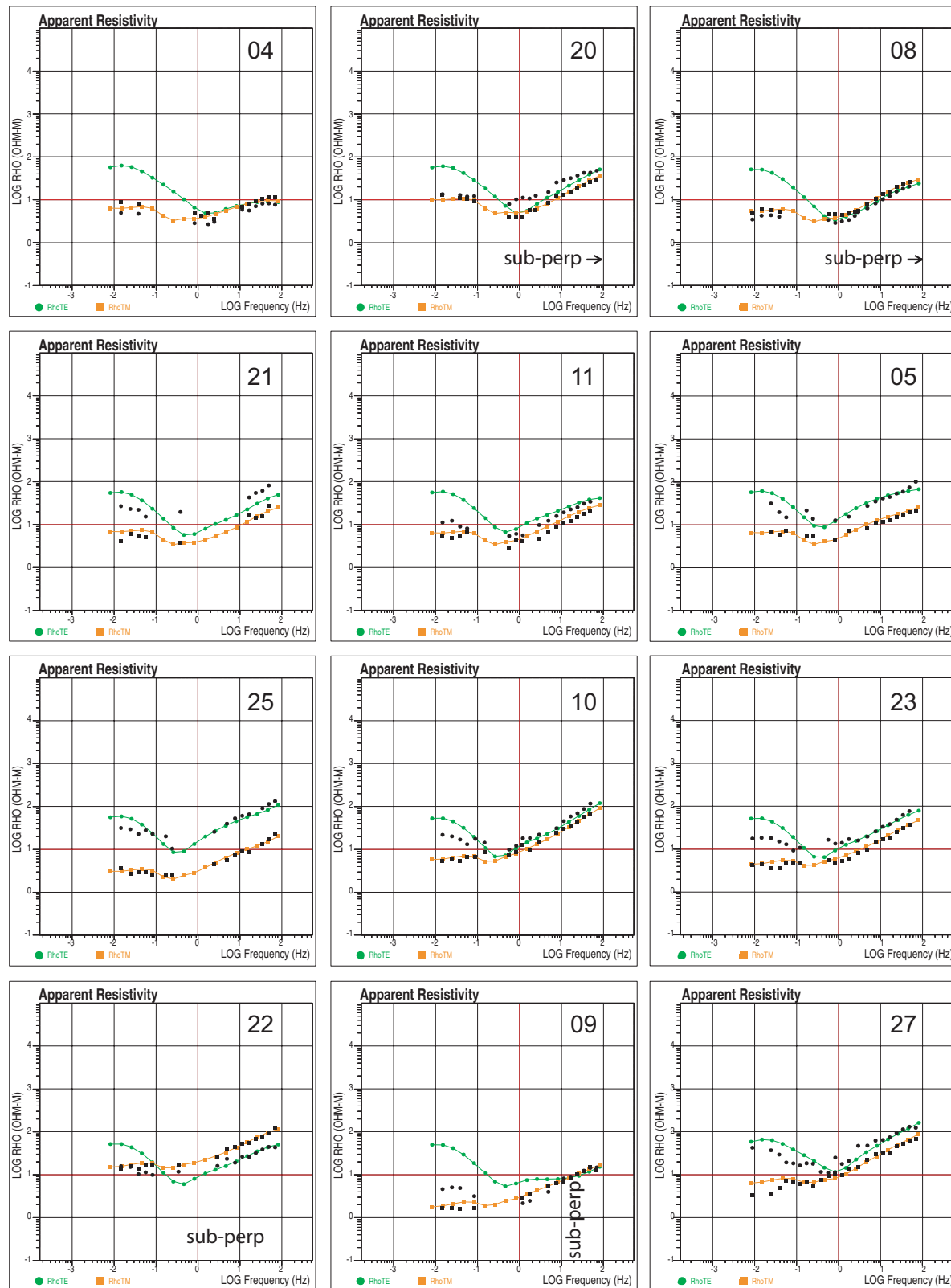


**Figure A1A.** Apparent resistivity plots of observed (black) and modeled (color, Fig. A11) magnetotelluric data for 2-D finite-element resistivity profile A-A' (Fig. 2A). Data rotated parallel to profile A-A' ( $10^{\circ}$  E of N). Tipper strikes (Fig. A6) are dominantly subparallel to profile except as noted with “sub-perp” for subperpendicular to profile.

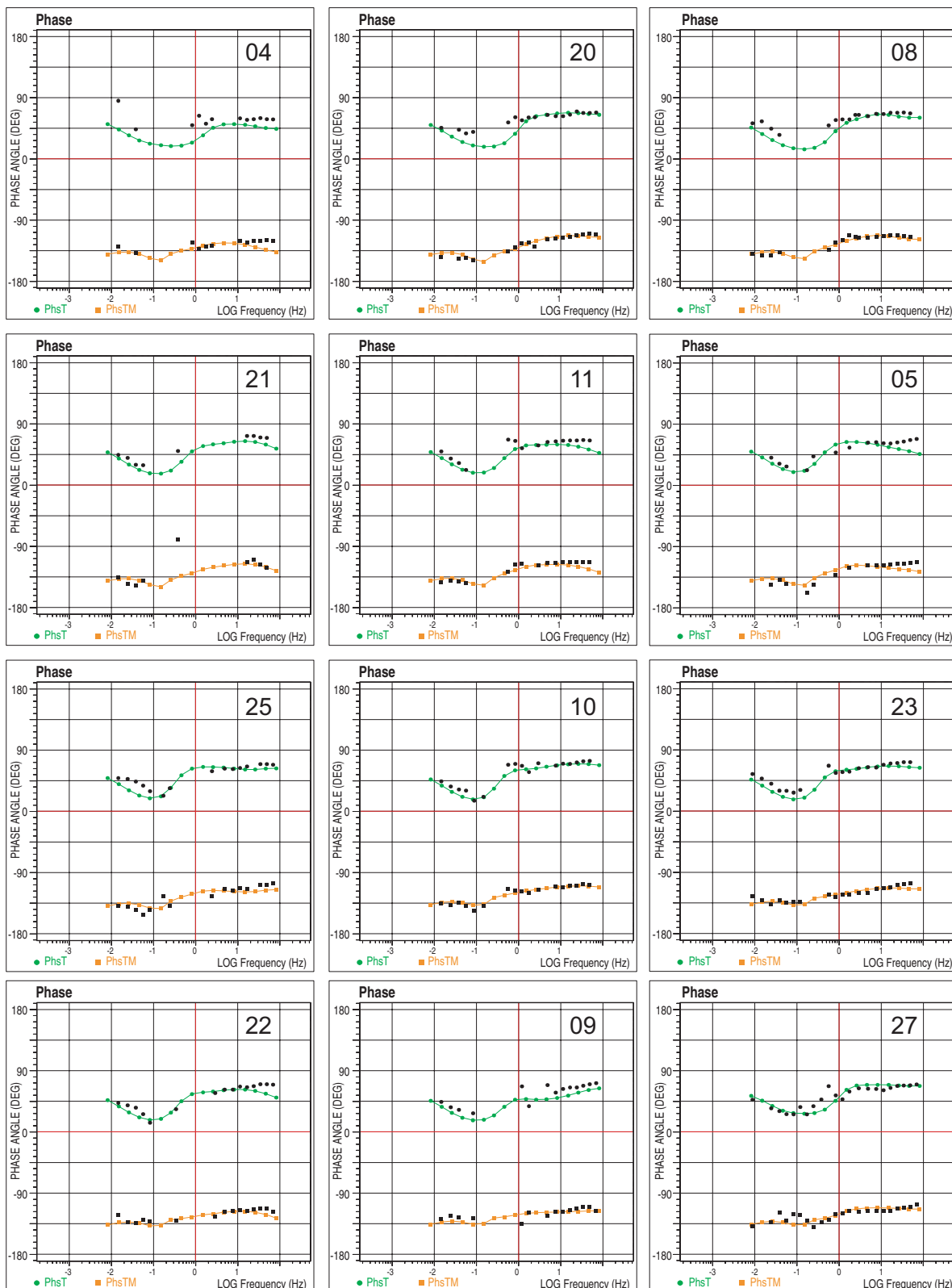


**Figure A1B.** Phase plots of observed (black) and modeled (color, Fig. A11) magnetotelluric data for 2-D finite-element resistivity profile A-A' (Fig. 2A).

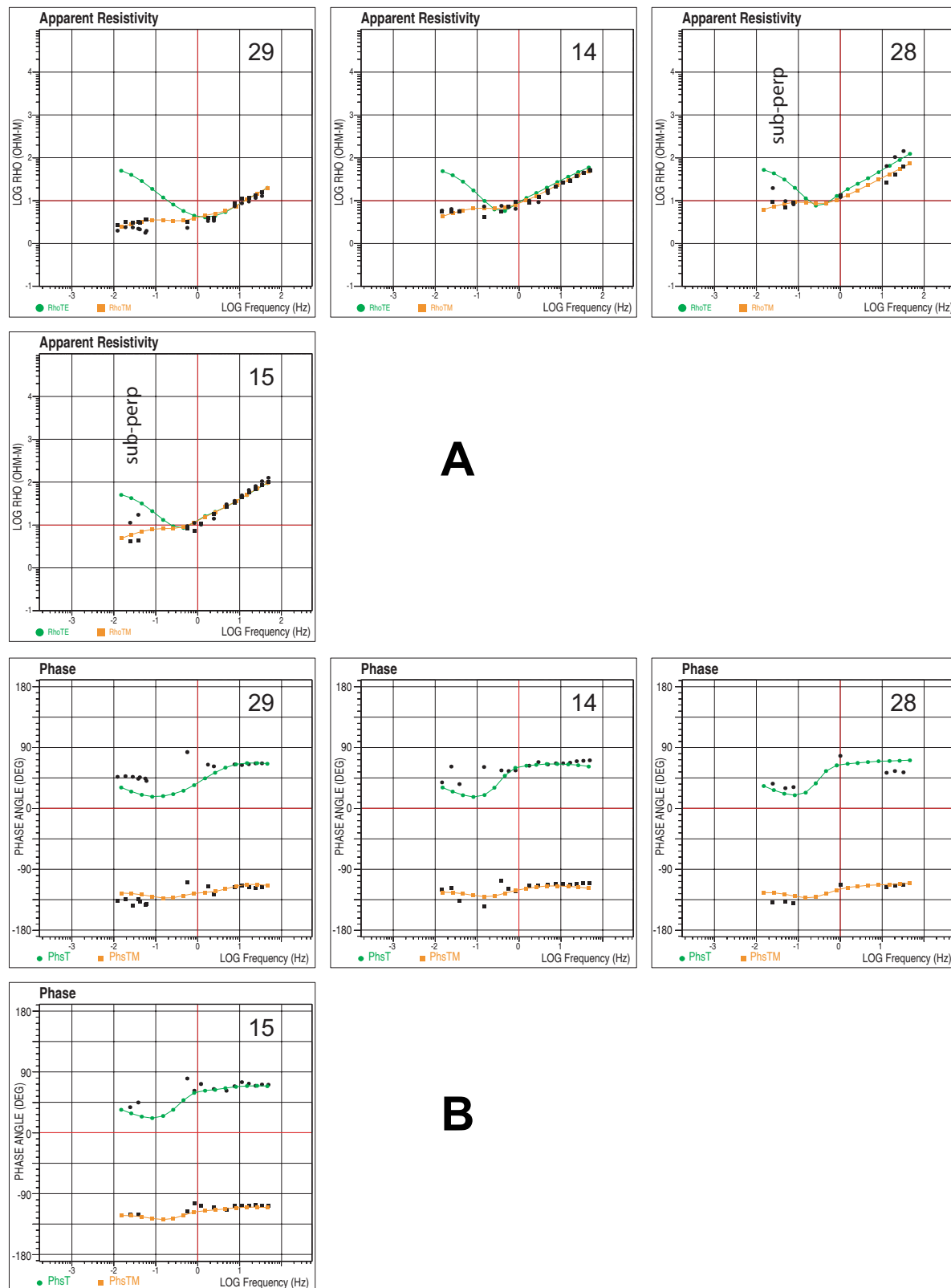


**Figure A2.** Plots of observed (black) and modeled (color, Fig. A12) magnetotelluric data for 2-D finite-element resistivity profile B-B' (Fig. 2A). Data rotated parallel to profile B-B' ( $0^\circ$  from N). *A*, Apparent resistivity. Tipper strikes (Fig. A7) are dominantly subparallel to profile except as noted with “sub-perp” for subperpendicular to profile. *B*, Phase.

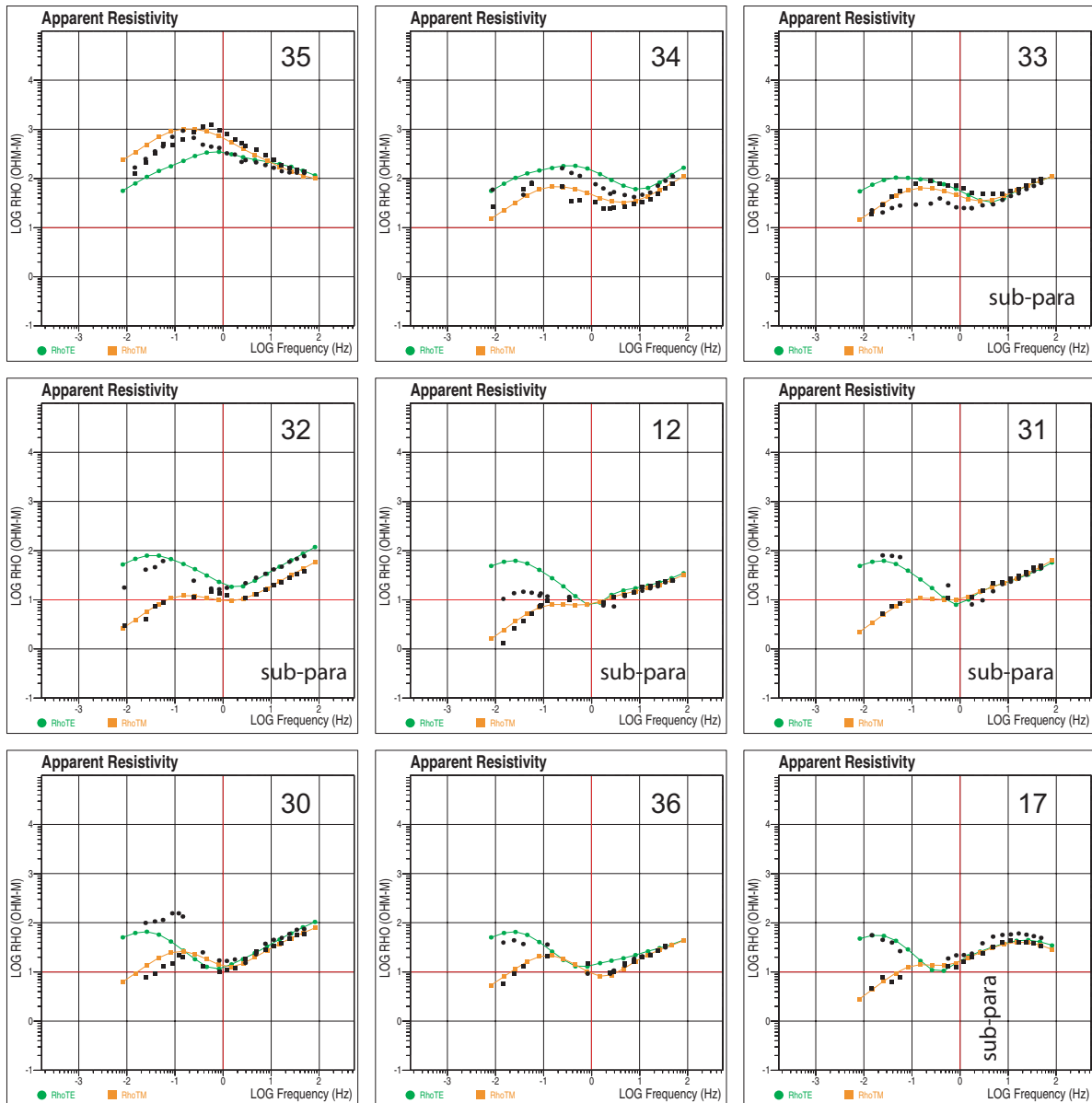


**Figure A3A.** Apparent resistivity plots of observed (black) and modeled (color, Fig. A13) magnetotelluric data for 2-D finite-element resistivity profile C-C' (Fig. 2A). Data rotated perpendicular to profile C-C' ( $45^{\circ}$  E of N). Tipper strikes (Fig. A8) are dominantly subperpendicular to profile except as noted with “sub-para” for subparallel to profile.

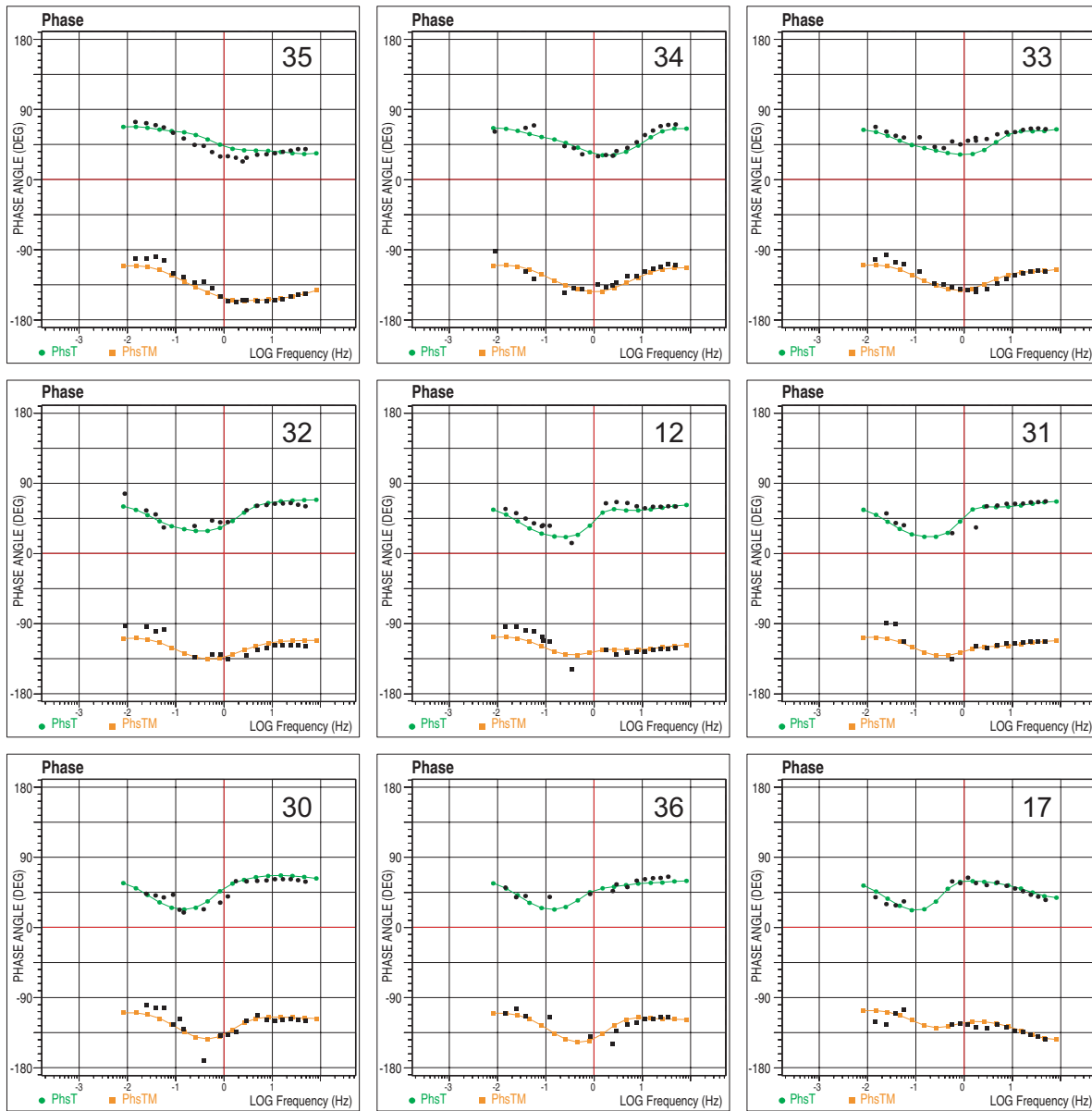
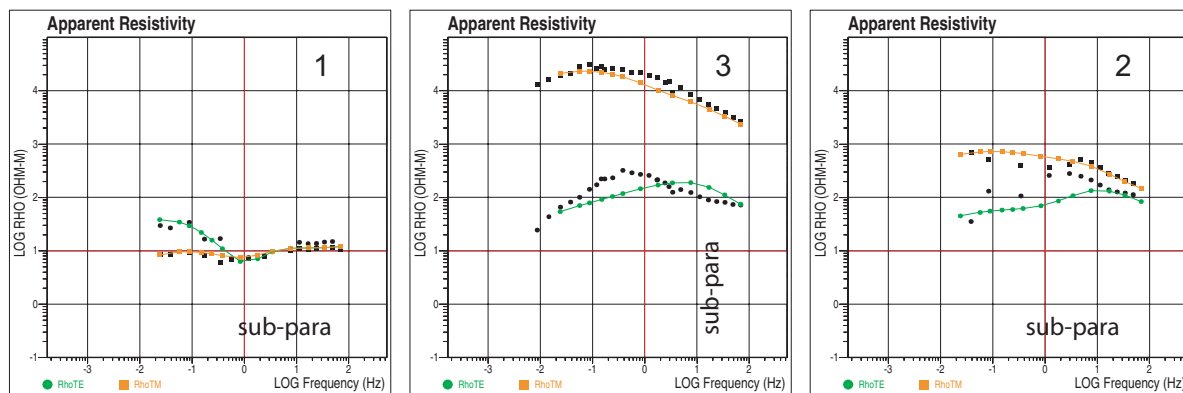


**Figure A3B.** Phase plots of observed (black) and modeled (color, Fig. A13) magnetotelluric data for 2-D finite-element resistivity profile C-C' (Fig. 2A)

**A**



**B**

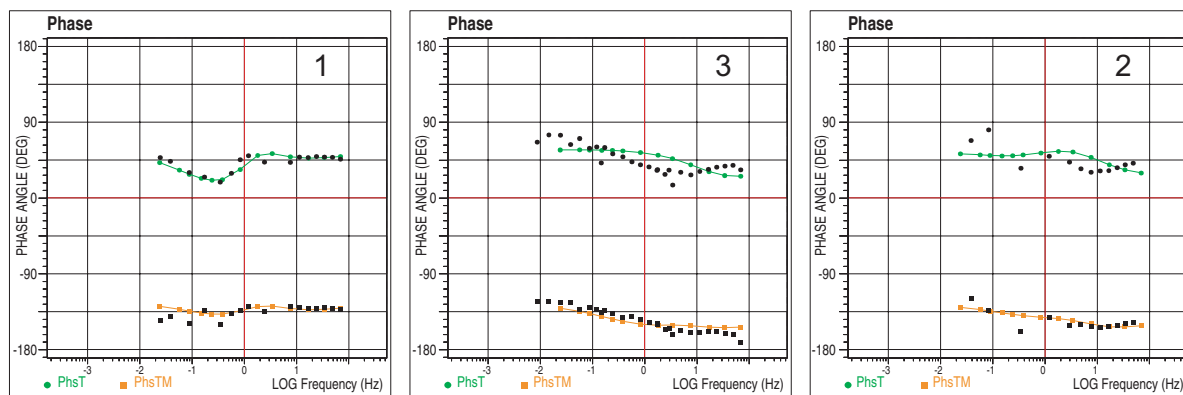


**Figure A4.** Plots of observed (black) and modeled (color, Fig. A17) magnetotelluric data for 2-D finite-element resistivity profile D-D' (Fig. 2A). Data rotated perpendicular to profile D-D' ( $12^\circ$  W of N). *A*, Apparent resistivity. All tipper strikes (Fig. A9) dominantly subperpendicular to profile except as noted with “sub-para” for subparallel to profile. *B*, Phase.

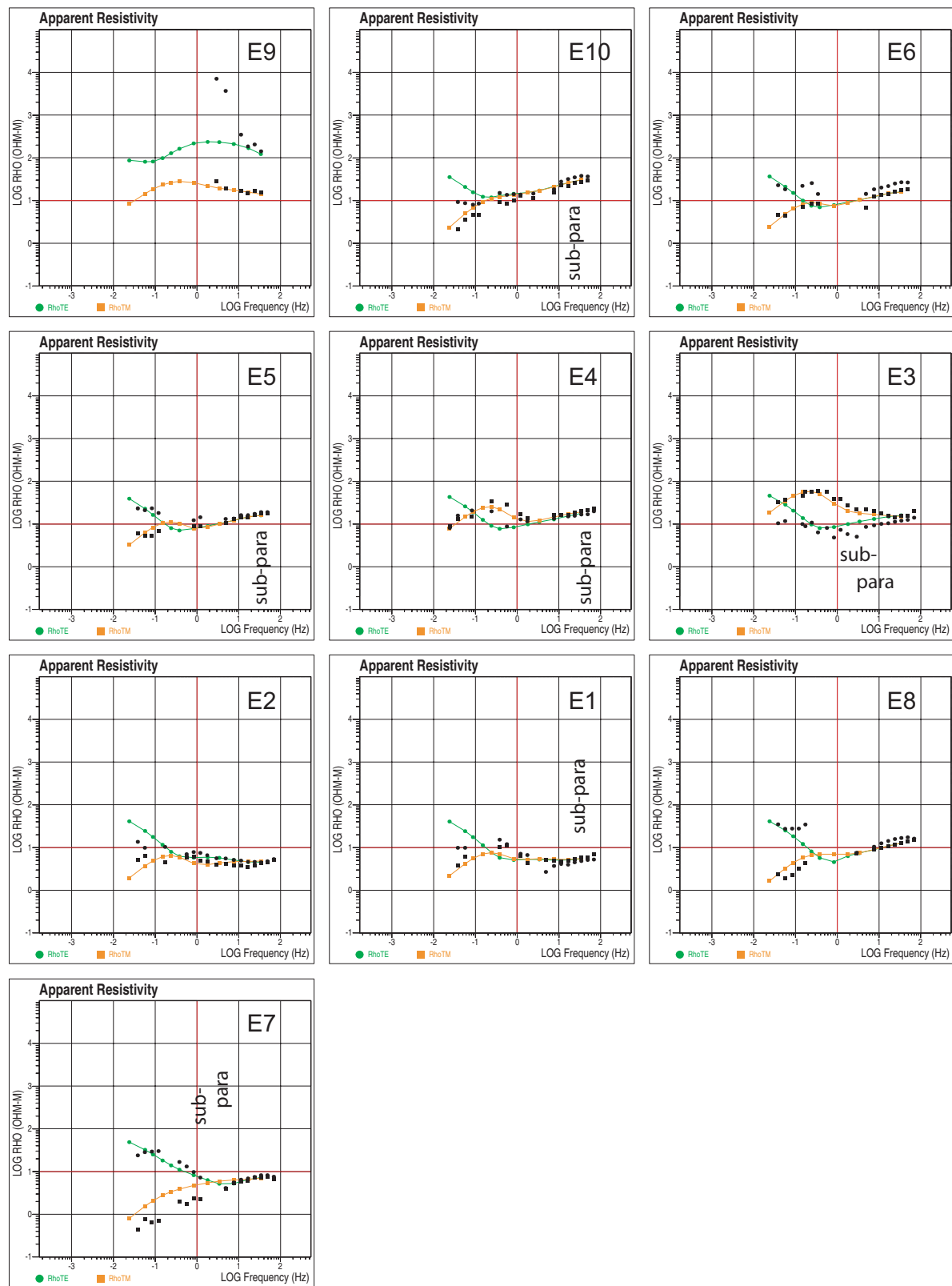


**Figure A5A.** Apparent resistivity plots of observed (black) and modeled (color, Fig. A18) magnetotelluric data for 2-D finite-element resistivity profile E-E' (Fig. 2B). Data rotated perpendicular to profile E-E' ( $0^\circ$  from N). All tipper strikes (Fig. A10) dominantly subperpendicular to profile except as noted with “sub-para” for subparallel to profile.

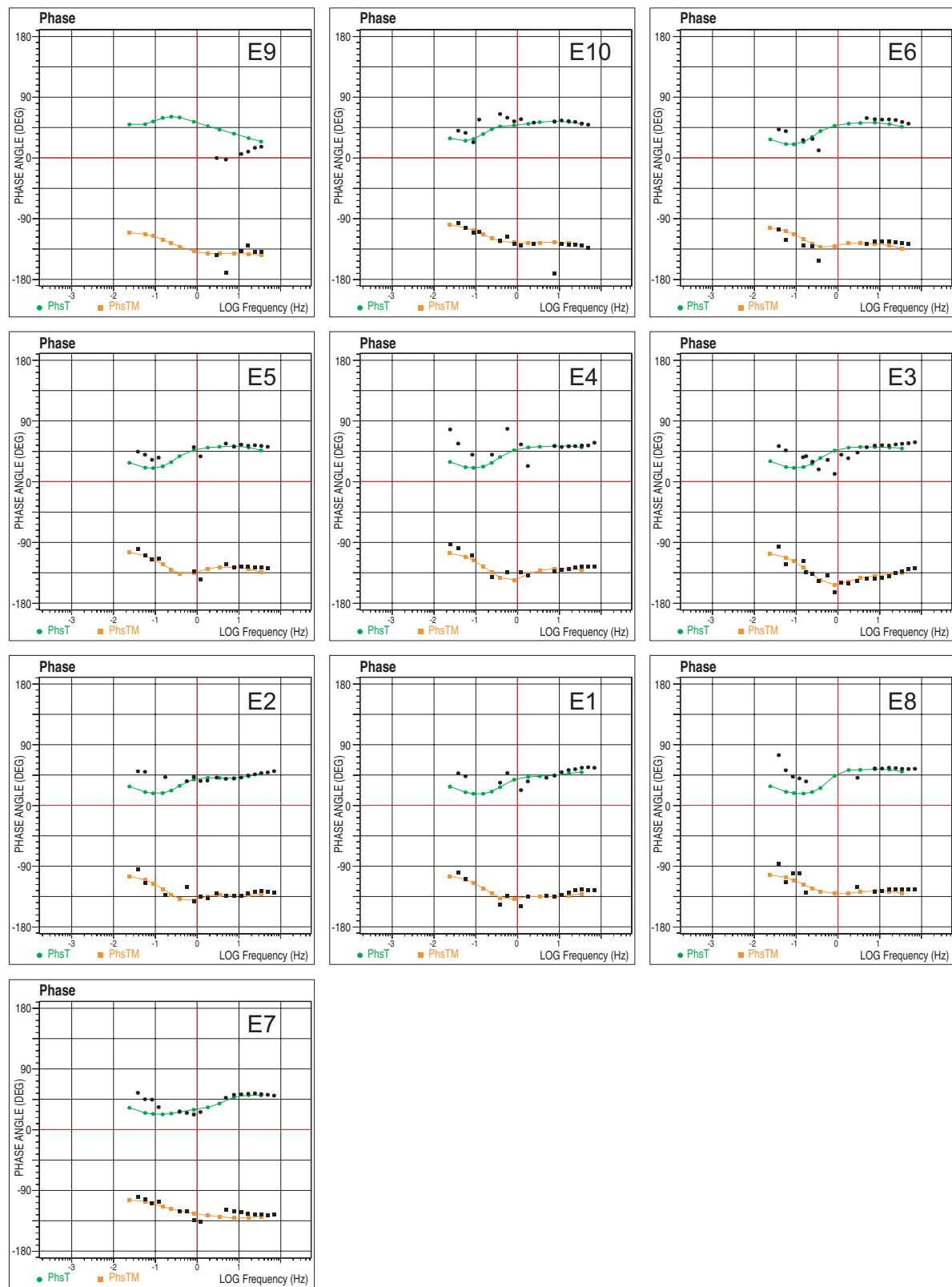


**Figure A5B.** Phase plots of observed (black) and modeled (color, Fig. A18) magnetotelluric data for 2-D finite-element resistivity profile E-E' (Fig. 2B).

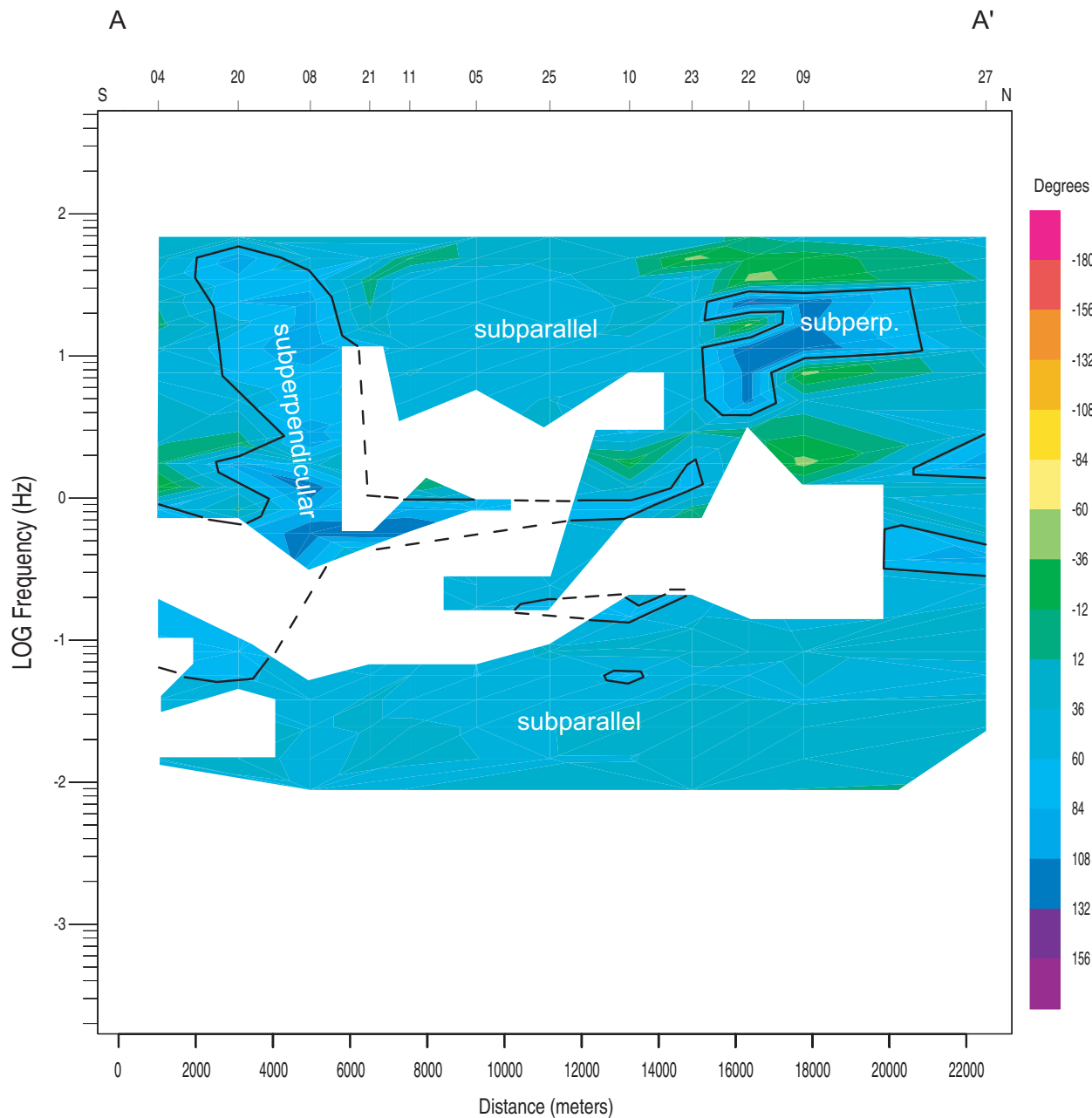


**Figure A6.** Magnetotelluric tipper strike data (degrees relative to North) of profile A-A' (Fig. 2A) determined from 3-D measurement of magnetic field. Numbered labels at top are magnetotelluric station numbers. Black solid lines (dashed where projected) define the boundary between subparallel (within  $45^\circ$  of the  $11^\circ$  profile azimuth) tipper strike angle and subperpendicular (outside  $45^\circ$  of the profile azimuth) strike angle domains. Blank zones are masked areas of poor data quality.

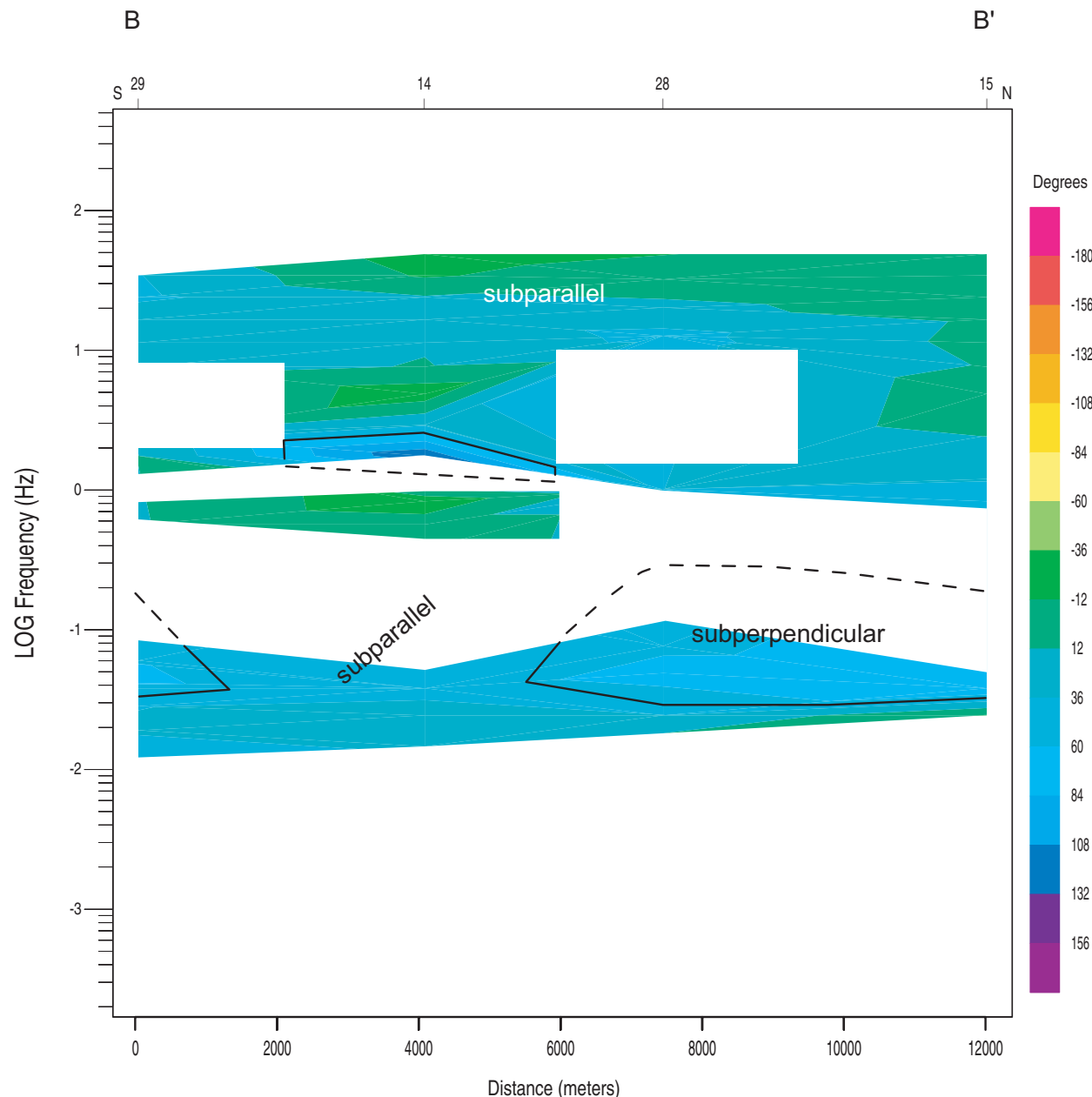


**Figure A7.** Magnetotelluric tipper strike data (degrees relative to North) of profile B-B' (Fig. 2A) determined from 3-D measurement of magnetic field. Black solid lines (dashed where projected) define boundary between subparallel (within 45° of the 0° profile azimuth) tipper strike angle and subperpendicular (outside 45° of the profile azimuth) strike angle domains. All other details same as Figure A6.

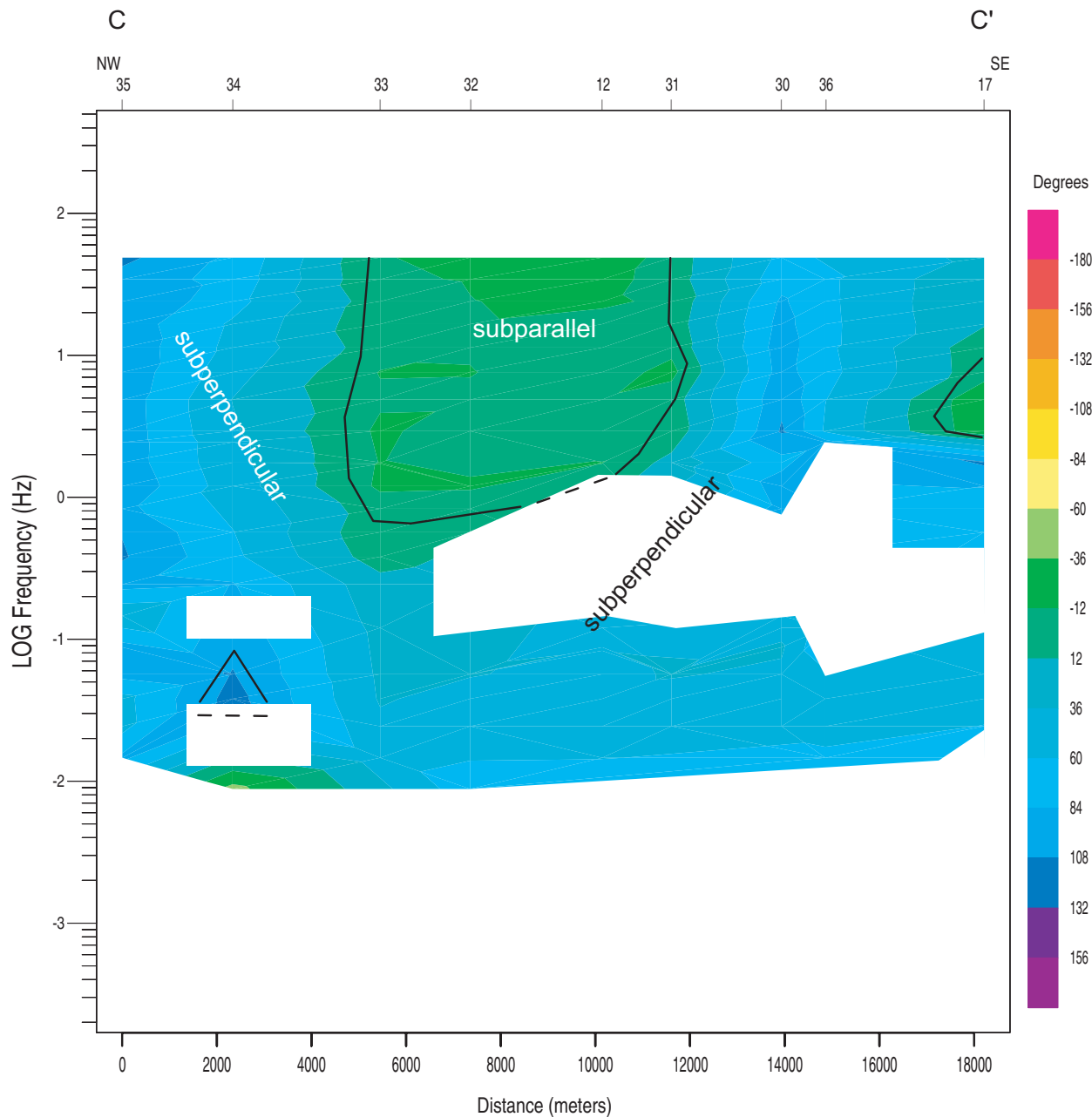


**Figure A8.** Magnetotelluric tipper strike data (degrees relative to North) of profile C-C' (Fig. 2A) determined from 3-D measurement of magnetic field. Black solid lines (dashed where projected) define boundary between subparallel (within 45° of the -45° profile azimuth) tipper strike angle and subperpendicular (outside 45° of the profile azimuth) strike angle domains. All other details same as Figure A6.

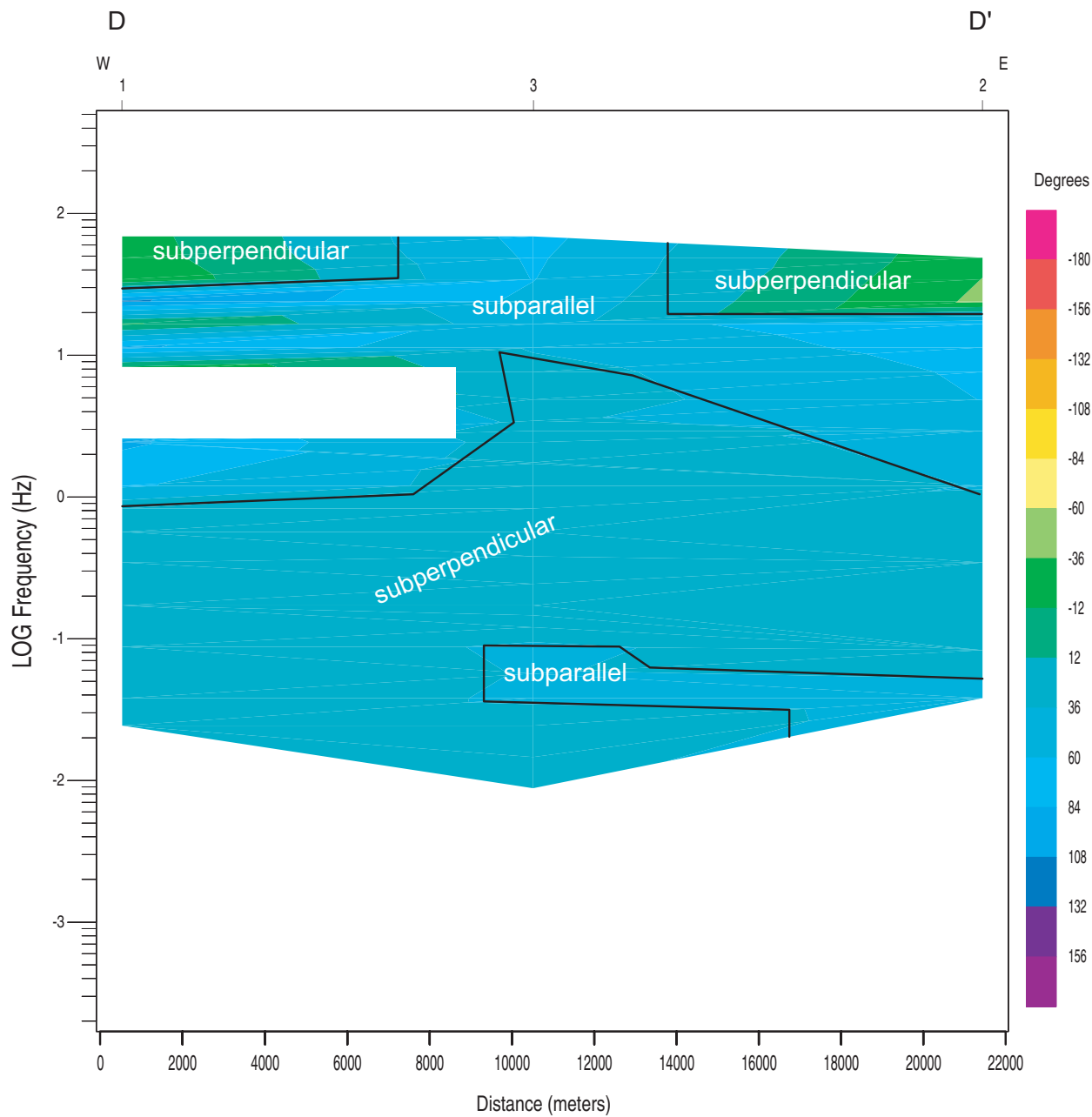


**Figure A9.** Magnetotelluric tipper strike data (degrees relative to North) of profile D-D' (Fig. 2A) determined from 3-D measurement of magnetic field. Black solid lines (dashed where projected) define boundary between subparallel (within  $45^\circ$  of the  $78^\circ$  profile azimuth) tipper strike angle and subperpendicular (outside  $45^\circ$  of the profile azimuth) strike angle domains. All other details same as Figure A6.

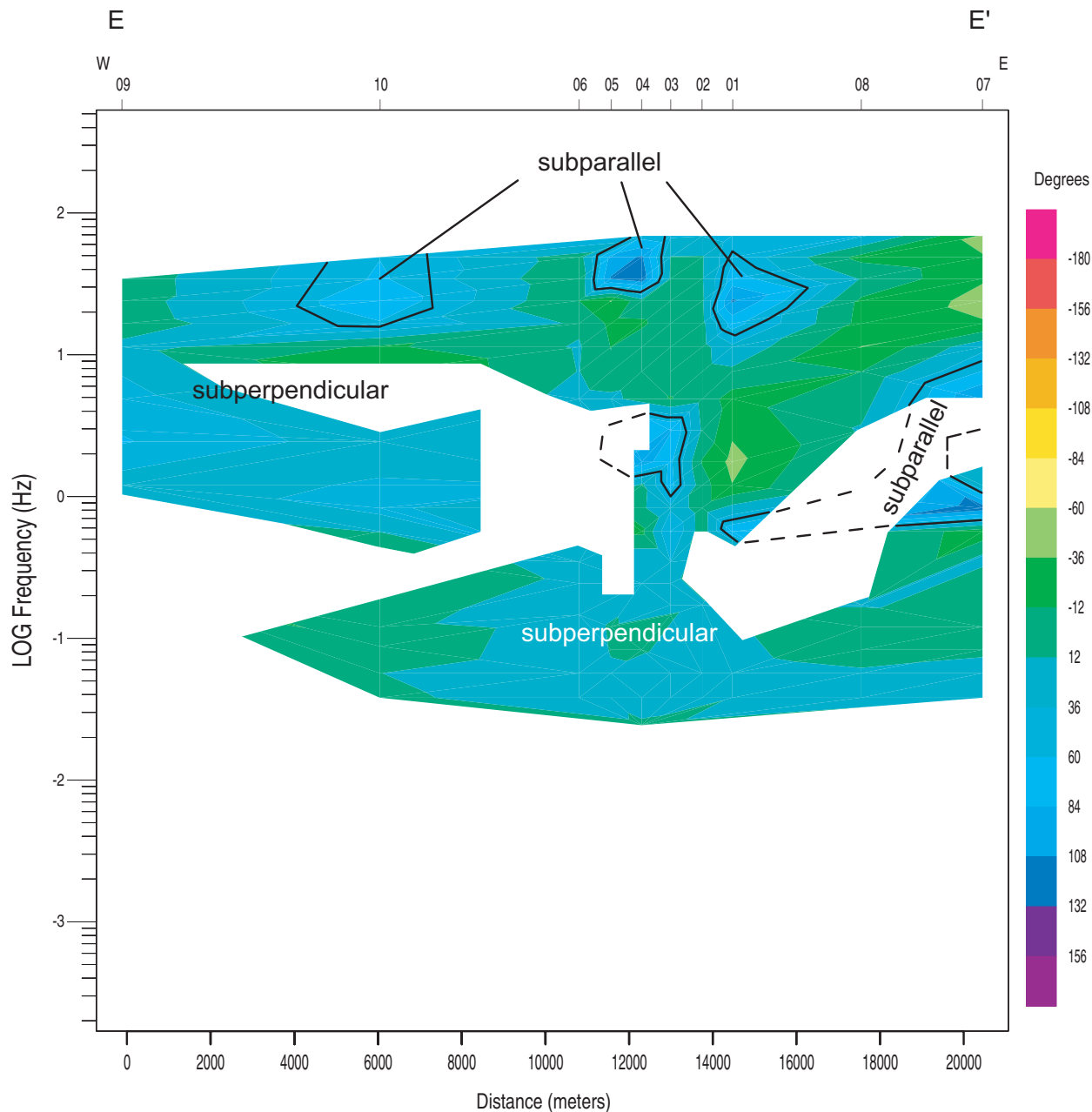


**Figure A10.** Magnetotelluric tipper strike data (degrees relative to North) of profile E-E' (Fig. 2B) determined from 3-D measurement of magnetic field. Black solid lines (dashed where projected) define boundary between subparallel (within  $45^\circ$  of the  $93^\circ$  profile azimuth) tipper strike angle and subperpendicular (outside  $45^\circ$  of the profile azimuth) strike angle domains. All other details same as Figure A6.

PW2D to help improve calculated data fits to the observed data and to test resistivity layer thickness limits. We forward-modeled each 2-D profile model, attempting to fit the calculated response primarily to the transverse magnetic mode observed response (Wannamaker et al., 1984), because the observed data at each magnetotelluric station indicated a 3-D electromagnetic response (Williams and Rodriguez, 2003a; 2003b; 2005a; 2005b; 2006). The transverse magnetic mode over a 2-D structure includes galvanic (boundary charge) terms in its formulation.

### ***Española basin region***

Magnetotelluric profile A-A' trends north-south (Fig. 1). The 2-D finite-element grid used in this model consisted of  $111 \times 112$  cells that extend over 500 km horizontally and 1,000 km vertically. In the finer part of the mesh, the horizontal element size is between 0.2 to 0.4 km. Magnetotelluric profile B-B' trends north-south. The 2-D finite-element grid used in this model consisted of  $79 \times 103$  cells that extend over 2,500 km horizontally and 200 km vertically. In the finer part of the mesh, the horizontal element size is between 0.1 to 0.3 km. Magnetotelluric profile C-C' trends northwest-southeast. The 2-D finite-element grid used in this model consisted of  $96 \times 96$  variable dimension cells that extend over 1,700 km horizontally beyond the profile end points and 300 km vertically. In the finer part of the mesh, the horizontal element size is between 0.2 to 0.4 km. Magnetotelluric profile D-D' trends east-west. The 2-D finite-element grid used in this model consisted of  $91 \times 64$  cells that extend over 800 km horizontally and 800 km vertically. In the finer part of the mesh, the horizontal element size is between 0.2 to 0.5 km. The vertical element size ranged from 10 m near the surface to 1 km below 5 km depth for all of the profile models.

### ***Albuquerque basin region***

Magnetotelluric profile E-E' trends east-west. The 2-D finite-element grid used in this model consisted of  $107 \times 105$  cells that extend over 500 km horizontally and 80 km vertically. In the finer part of the mesh, the horizontal element size is between 0.1 to 0.4 km. The vertical element size ranged from 10 m near the surface to 1 km below 5 km depth for all of the profile models.

### ***Topographic Effects***

Topographic relief along profiles (Table A2) A-A' (Fig. 7) and B-B' (Fig. 9) is insignificant between stations (about 100 m or less) relative to the thickness of the conductive section of each model (1.5 to 2.0 km). Relief along profile C-C' (Fig. 10) is about 100 to 200 m between stations, although the constant rise of 700 m in topographic relief over the entire length of the 18-km long profile produces an apparent southeast dip on the horizontal depth model layers beneath stations 32, 12, 31, and 30, and also stations 34 and 33 along the profile. A relief of about 300 m along profile D-D' (Fig. 11) between stations 1 and 3 increases the apparent west dip on the resistive basement depicted in the depth model. All of the relief along profile E-E' (Fig. 12) is less than 100 m between stations, except at station 7 (about 150 m relief relative to station 8) that places an apparent west dip on the resistive basement in the depth model.

We did not attempt to make topographic corrections to this data set because the topographic relief between stations is small relative to the thickness of the conductive section modeled along each profile, which comprises the bulk of the measured magnetotelluric response in this study area. In general, topographic effects are smaller in 3-D geologic environments than in 2-D cases because of the finite dimensions of the conductors (Vozoff, 1991). True

electromagnetic distortion corrections due to topography require continuous data and the application of more than one correction-modeling scheme (Jiracek, 1990), which is beyond the scope of this study.

## Analysis of 3-D Effects

This study represents the first published 2-D resistivity models for the upper crust in the Rio Grande rift, New Mexico not biased by 3-D effects from inverting transverse electric mode data. Earlier studies that reported magnetotelluric results in this region (Biehler et al., 1991; Hermance and Pedersen, 1980; Jiracek et al., 1987; Quesada, 2004) inverted their transverse electric mode data for the upper crust, which complicated correlations of their 2-D resistivity models to regional borehole resistivity and lithologic data because their 2-D resistivity models would have contained extraneous conductor artifacts related to excess currents in a 3-D modeling space. These conductive artifacts added to the difficulty in making realistic geologic interpretations of their resistivity models. The calculated fits of our 2-D forward resistivity models are shown in figures [A1 to A5](#). We also attempted to achieve a robust resistivity model by minimizing the number of resistivity layers (Figs. 7, 9, 10, 11, and 12), while maintaining calculated data misfits to a minimum, incorporating the expected magnetotelluric response to Rio Grande rift stratigraphy (Figs. 5 and 6) to test depth resolution to the minimum number of resolvable resistivity layers, and integrating nearby well control to constrain the modeled resistivity layer thicknesses.

### **3-D Forward Model**

To test whether our 2-D approximations are valid for the 3-D magnetotelluric data, we calculated the forward response of a 3-D resistivity model using a 3-D resistivity modeling algorithm, called MTD3FWD, by Mackie et al. (1993) and used our 2-D resistivity models in the Española basin for profiles A-A', B-B', and C-C' (Figs. [A11](#), [A12](#), and [A13](#)) as initial input. We modified the 3-D model (Figs. [A14-A16](#)) to improved calculated fits to both 3-D xy and yx (where xy is 0° North and yx is 90° East, and all data are rotated to 0° North) components (Figs. [A19-A25](#)) along each of the three profiles in the Española basin (Figs. [A14-A16](#)).

Our 2-D model along profile A-A' (Fig. [A11](#)) agrees well with the corresponding profile extraction from the 3-D model (Fig. [A14](#)) in the upper km, with the following exceptions: between magnetotelluric stations 10 and 27, where the 3-D model suggests more resistive material indicative of upper Santa Fe Group sediments, and also beneath station 9 where the 3-D resistivity model suggests a 3-D conductive body whose top is within the volcanic overburden (VLCC). We prefer using the basin floor model of Grauch et al. (2009) between stations 4 and 11 delineating the boundary between upper Santa Fe Group sediments (SNTFu) and inferred Espinaso (TOVS) and lower Mancos shale (MNCSI). Below 1 km depth, the 3-D model suggests the inferred Phanerozoic section is about 500 m thinner than the 2-D model beneath stations 9 and 22. Beneath stations 11 and 21 the 2-D and 3-D resistivity models differ significantly on the depth top of the Pennsylvanian (C) and Precambrian (PCMB), but the computed response to the 3-D model at these stations (Figs. [A19-A25](#)) suggest larger depths to these horizons than modeled, so we prefer using the interpreted 2-D model Pennsylvanian and Precambrian horizons for these stations.

Our 2-D model along profile B-B' (Fig. [A12](#)) agrees well with the corresponding profile extraction from the 3-D model (Fig. [A15](#)), except near station 28 where the 3-D resistivity model

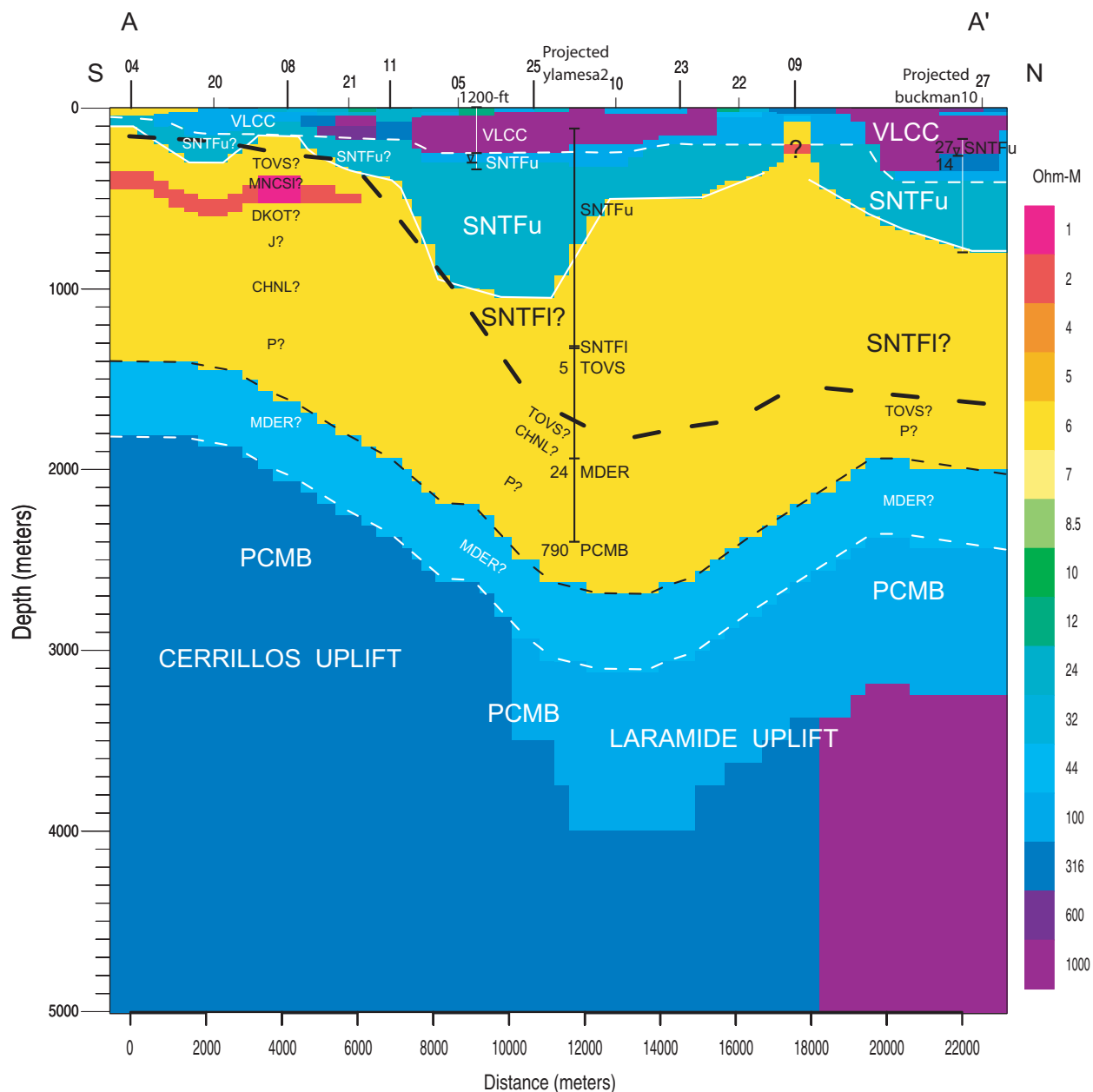


**Figure A11.** Profile A-A' (Fig. 2A) 2-D finite-element resistivity profile model with lithologic interpretation. Numbered labels at top of model are magnetotelluric station numbers. Thick black dashed line is basin floor model from Grauch et al. (2009). Black solid lines are interpreted major geologic boundaries (dashed where poorly constrained by magnetotelluric data). See Table 1 for well shortname key. See Table 2 for geologic symbol key. Vertical exaggeration is about 5.

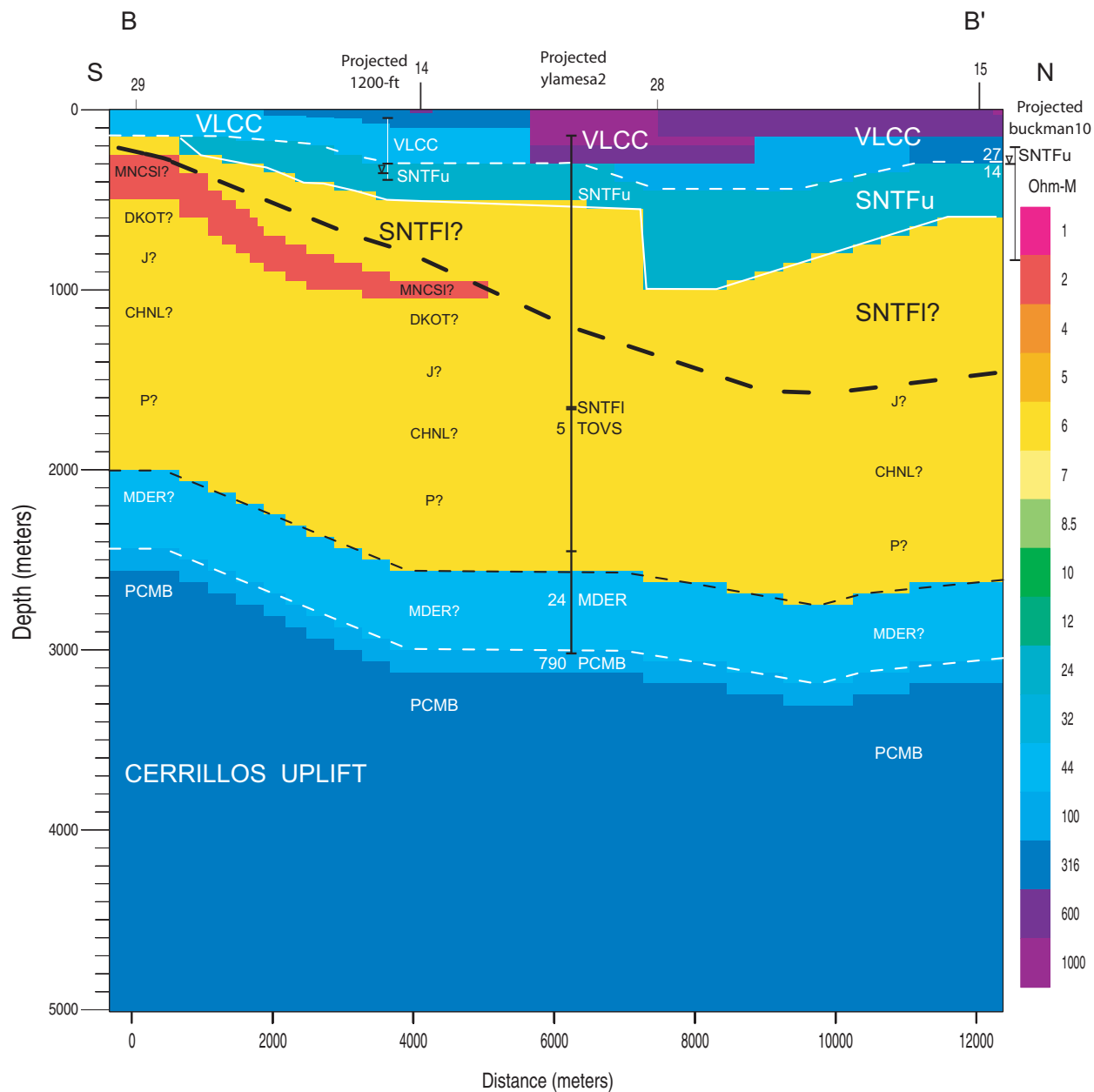


**Figure A12.** Profile B-B' (Fig. 2A) 2-D finite-element resistivity profile model with lithologic interpretation. Vertical exaggeration is about 3. All other details same as Figure A11.

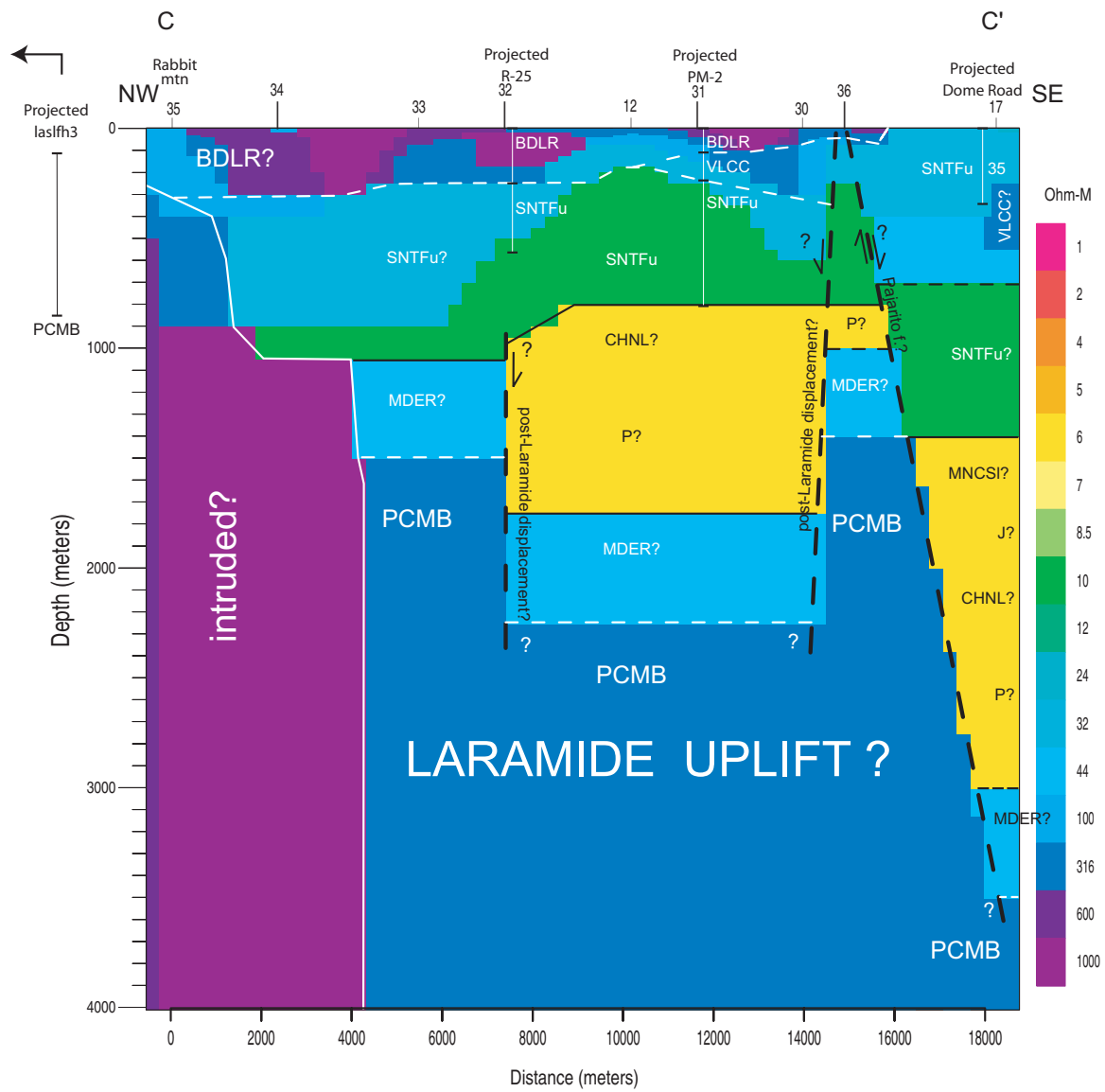


**Figure A13.** Profile C-C' (Fig. 2A) 2-D finite-element resistivity profile model with lithologic interpretation. Subvertical black dashed lines are inferred fault zones. Vertical exaggeration is about 5. All other details same as Figure A11.

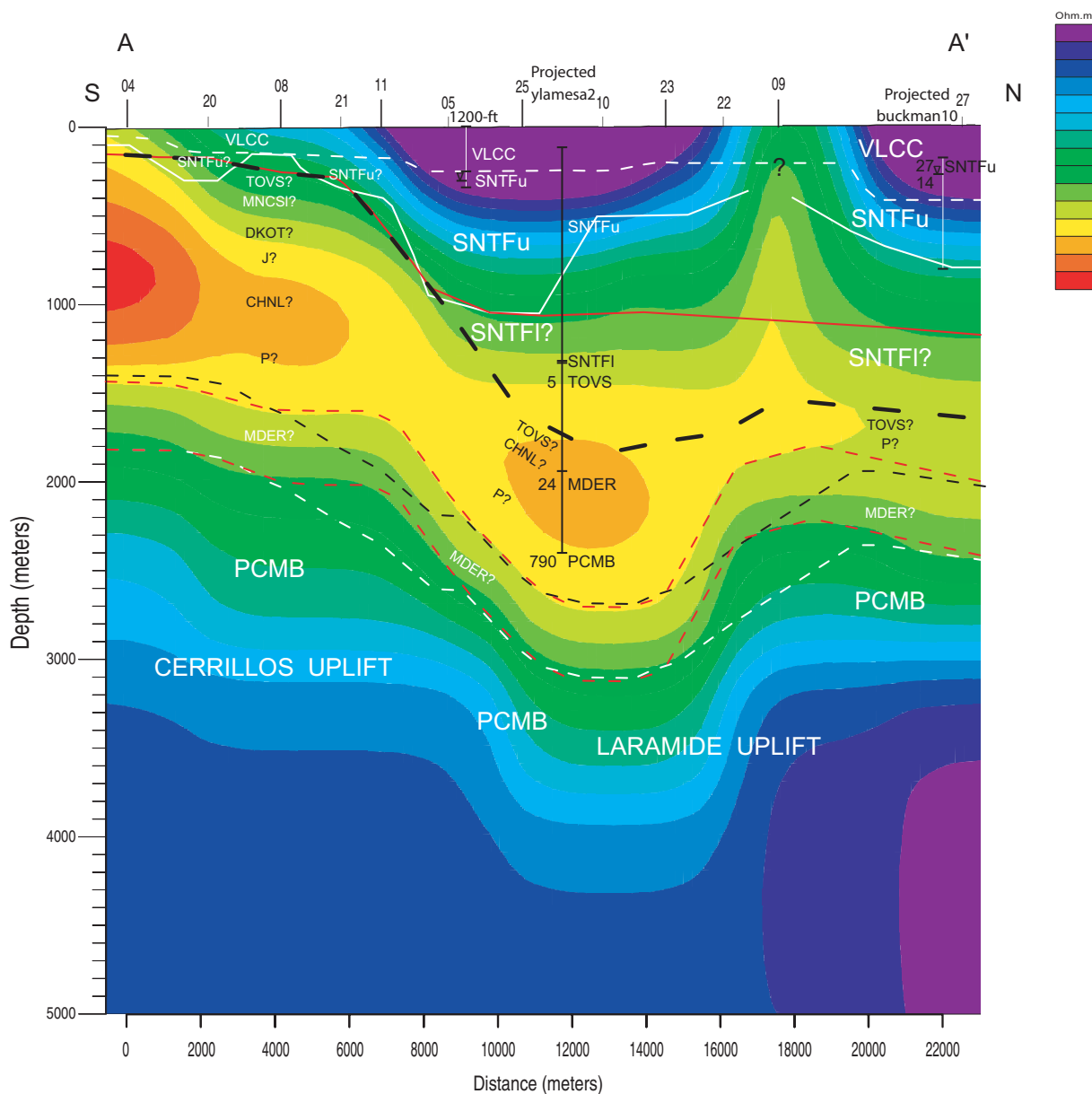


**Figure A14.** Profile A-A' (Fig. 2A) resistivity section extracted from 3-D finite-element resistivity model with lithologic interpretation. Numbered labels at top of model are magnetotelluric station numbers. Thick black dashed line is basin floor model from Grauch et al. (2009). Black solid lines are interpreted major geologic boundaries (dashed where poorly constrained by magnetotelluric data) from 2-D resistivity model (Fig. A11). Red lines are revised interpreted major geologic boundaries (dashed where poorly constrained by magnetotelluric data) from three-dimensional resistivity model. See Table 1 for well shortname key. See Table 2 for geologic symbol key. Vertical exaggeration is about 5.

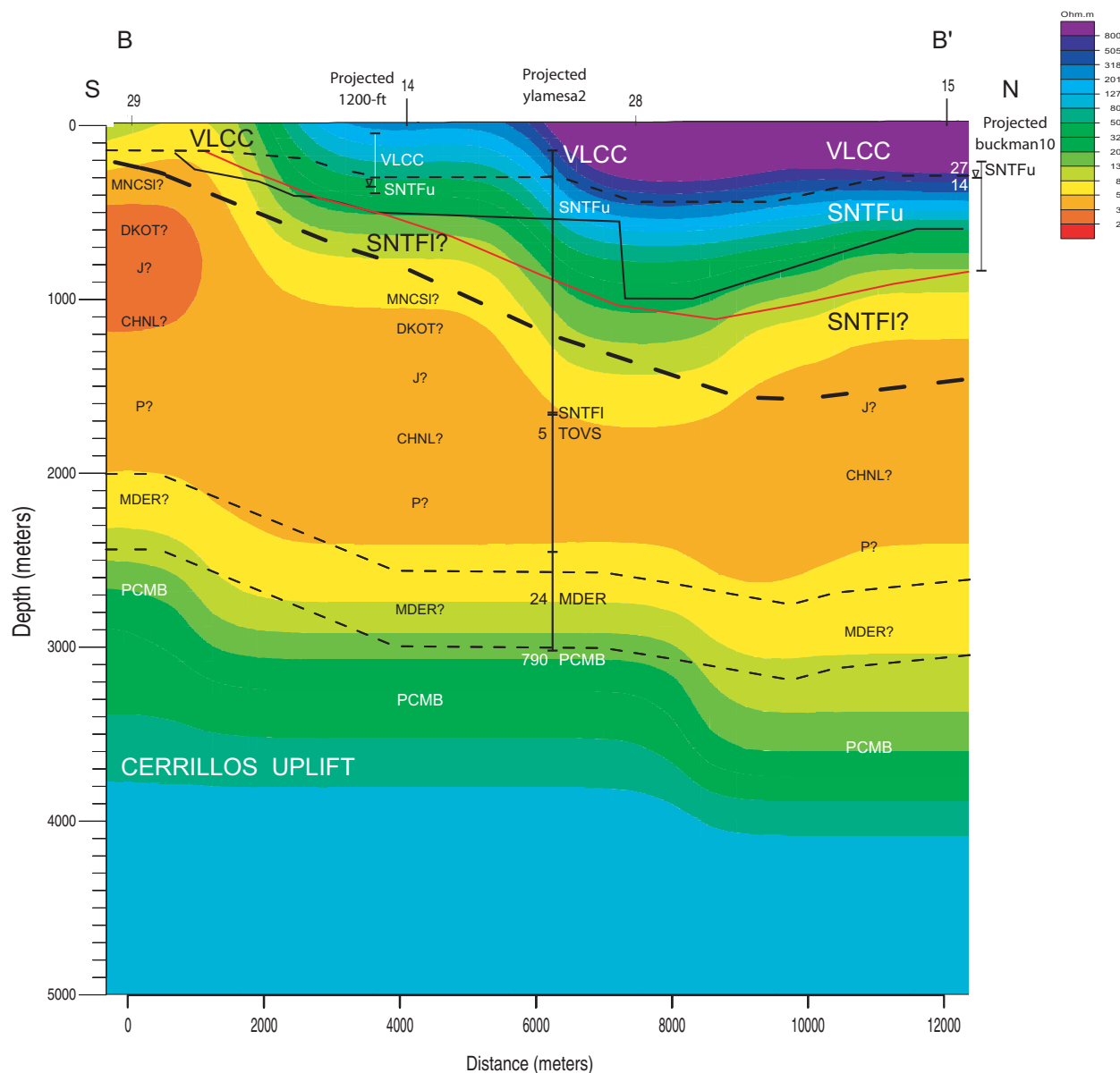


**Figure A15.** Profile B-B' (Fig. 2A) resistivity section extracted from 3-D finite-element resistivity profile model with lithologic interpretation. Black solid lines are interpreted major geologic boundaries (dashed where poorly constrained by magnetotelluric data) from 2-D resistivity model (Fig. A12). Vertical exaggeration is about 3. All other details same as Figure A14.

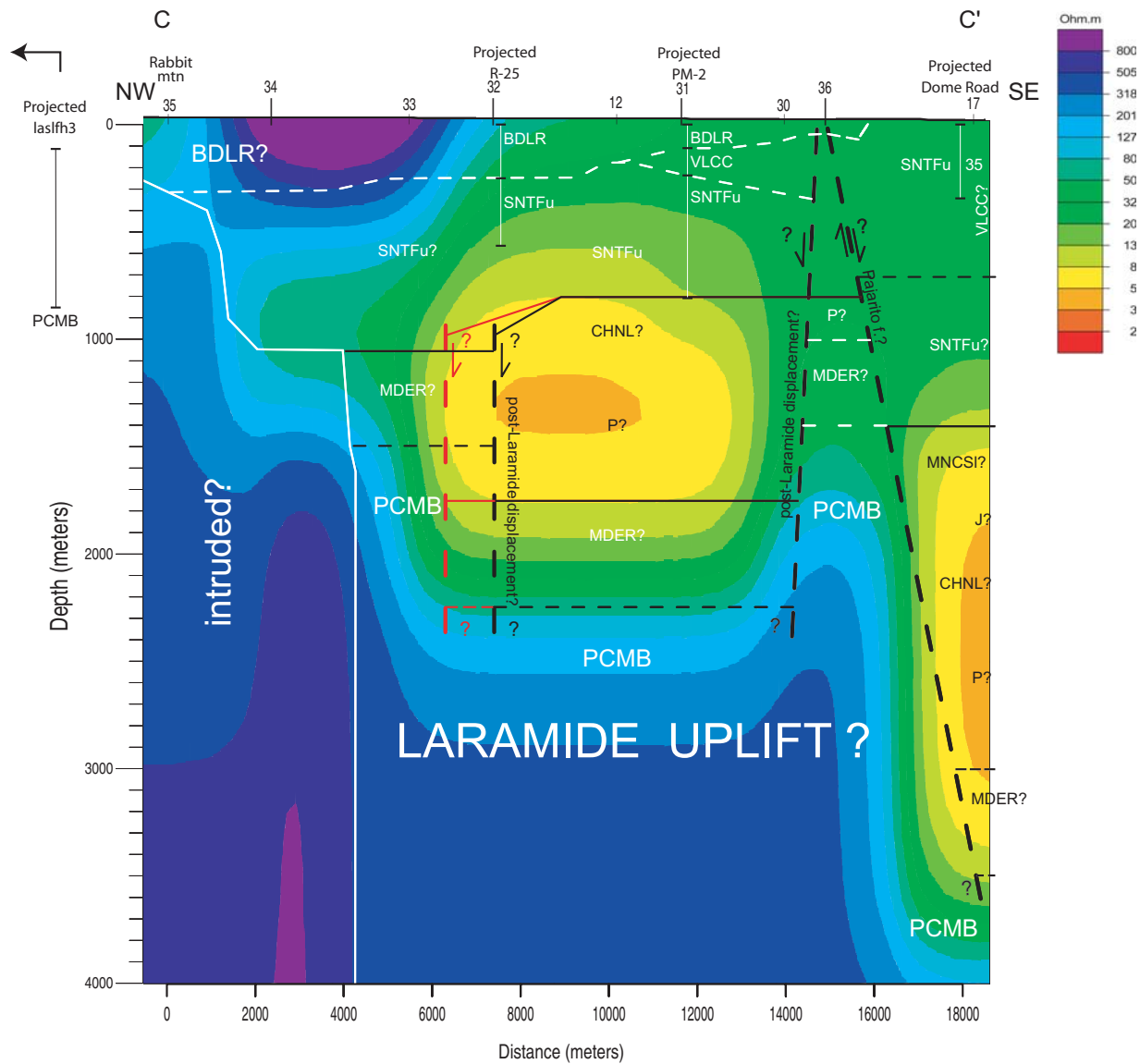


**Figure A16.** Profile C-C' (Fig. 2A) resistivity section extracted from 3-D finite-element resistivity profile model with lithologic interpretation. Subvertical black dashed lines are inferred fault zones. Black solid lines are interpreted major geologic boundaries (dashed where poorly constrained by magnetotelluric data) from 2-D model (Fig. A13). Vertical exaggeration is about 5. All other details same as Figure A14.

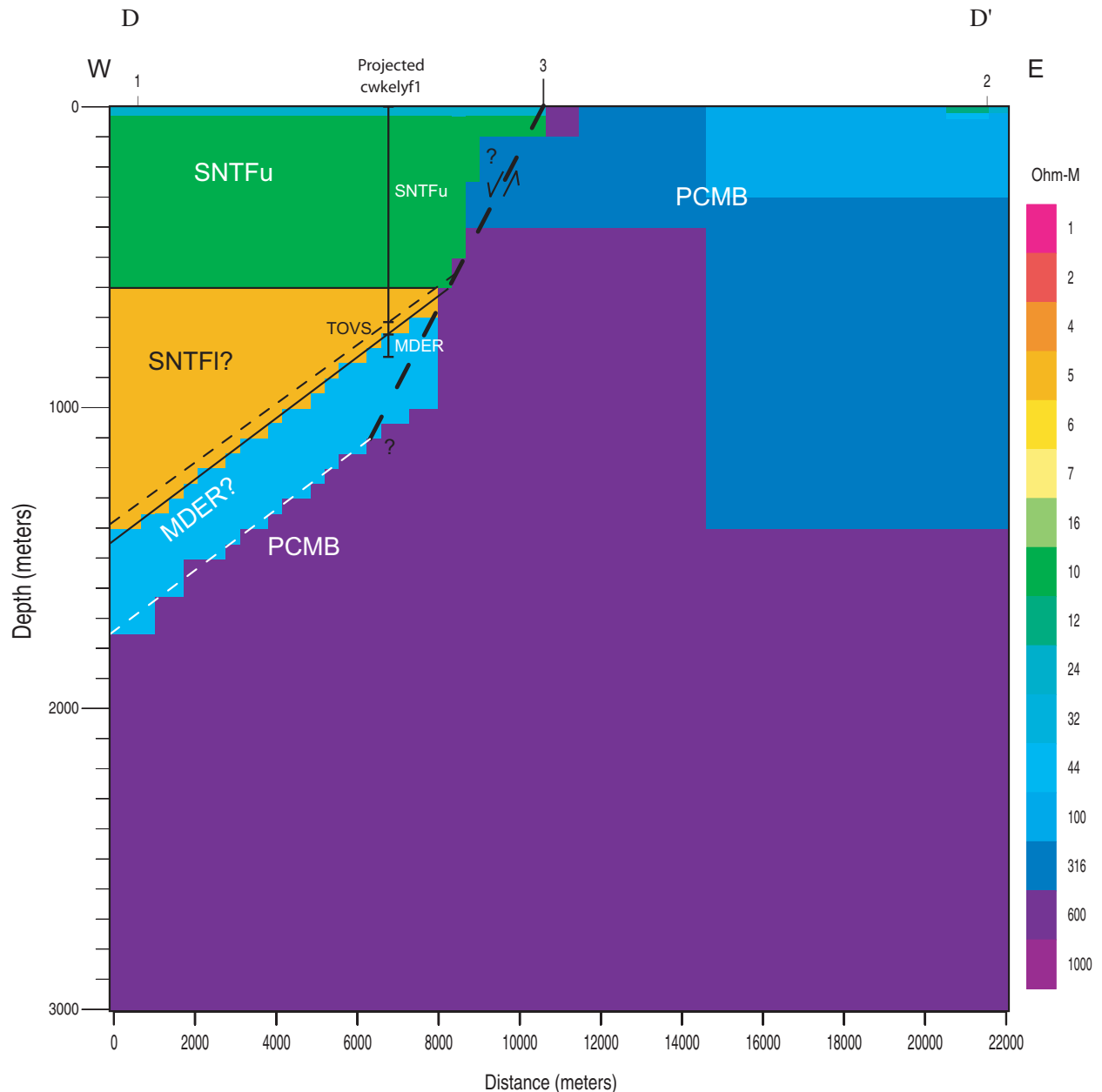


**Figure A17.** Profile D-D' (Fig. 2A) 2-D finite-element resistivity model with lithologic interpretation. Subvertical black dashed line is inferred fault zone. Vertical exaggeration is about 7. All other details same as Figure A11.

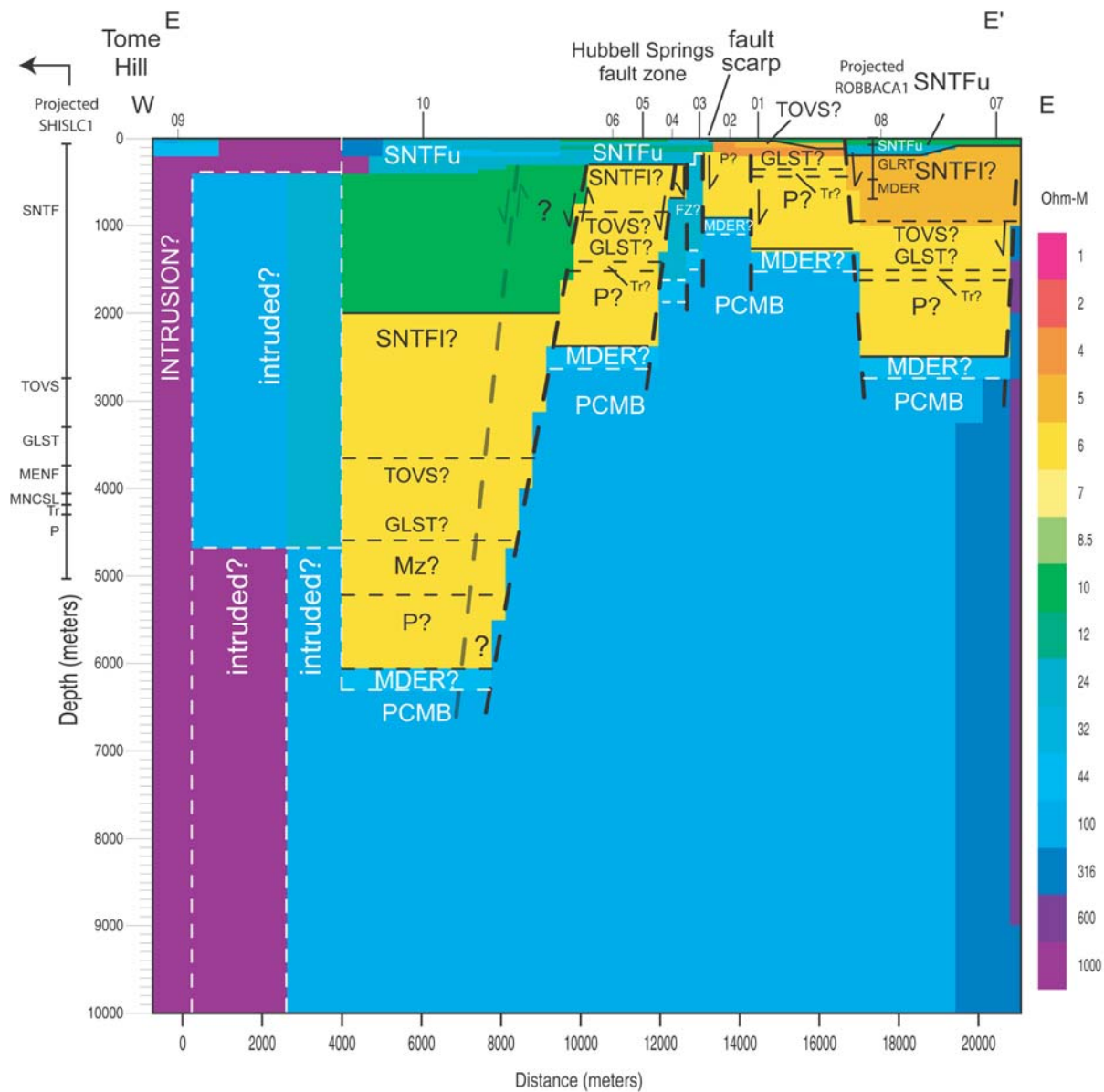


**Figure A18.** Profile E-E' (Fig. 2B) 2-D finite-element resistivity model with lithologic interpretation. Subvertical black dashed lines are inferred fault zones. Subvertical grey dashed line is alternate fault zone. Vertical exaggeration is about 2. Mz includes MENF, MNCSL, and Tr. All other details same as Figure A11.

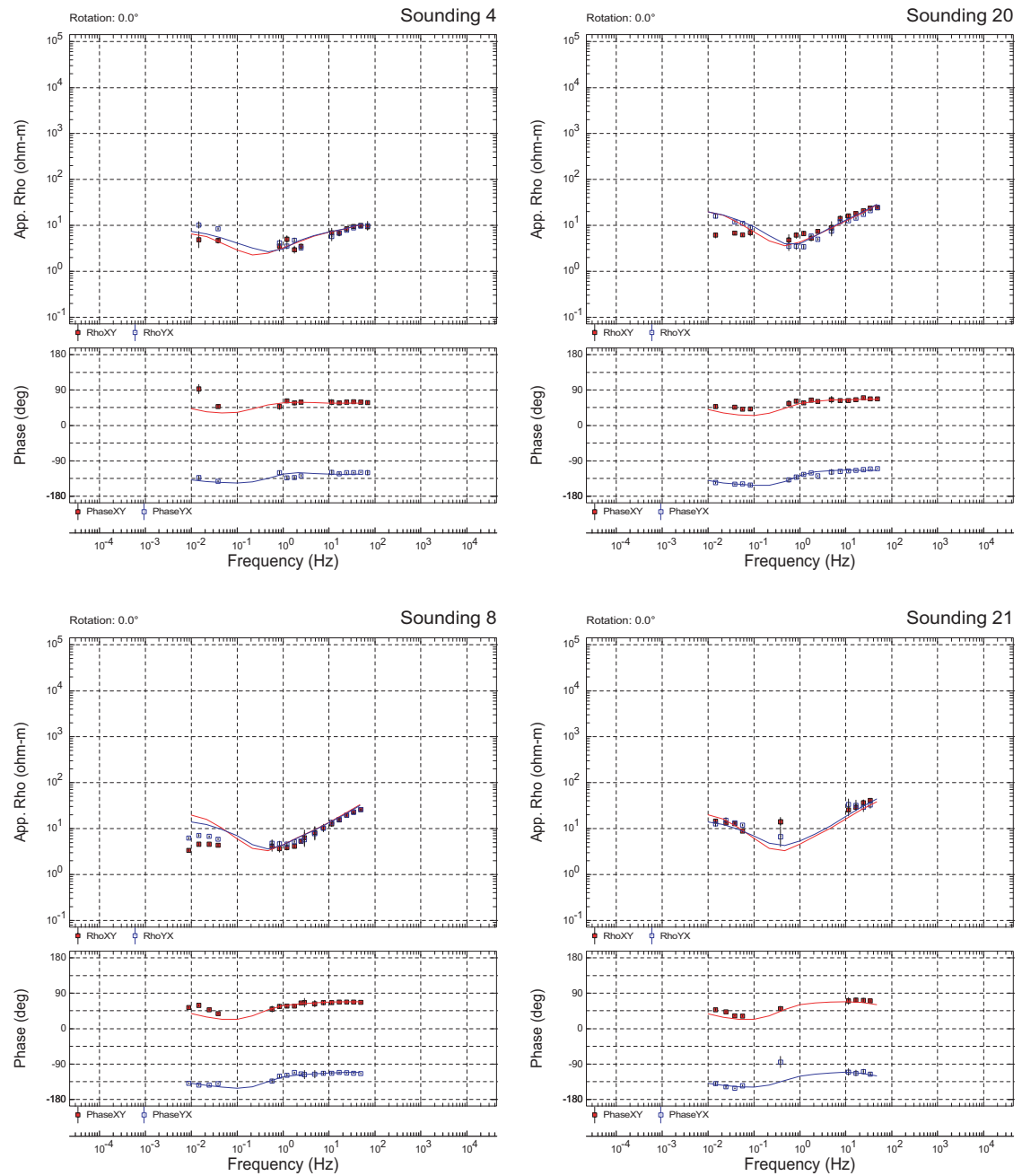


**Figure A19.** Plots of observed (square symbols) and calculated (red and blue lines) magnetotelluric resistivity and phase data at stations 4, 20, 8, and 21 from profile A-A' (Figs. 2A, A14) for 3-D forward finite-element resistivity model. Data rotated to 0° North.

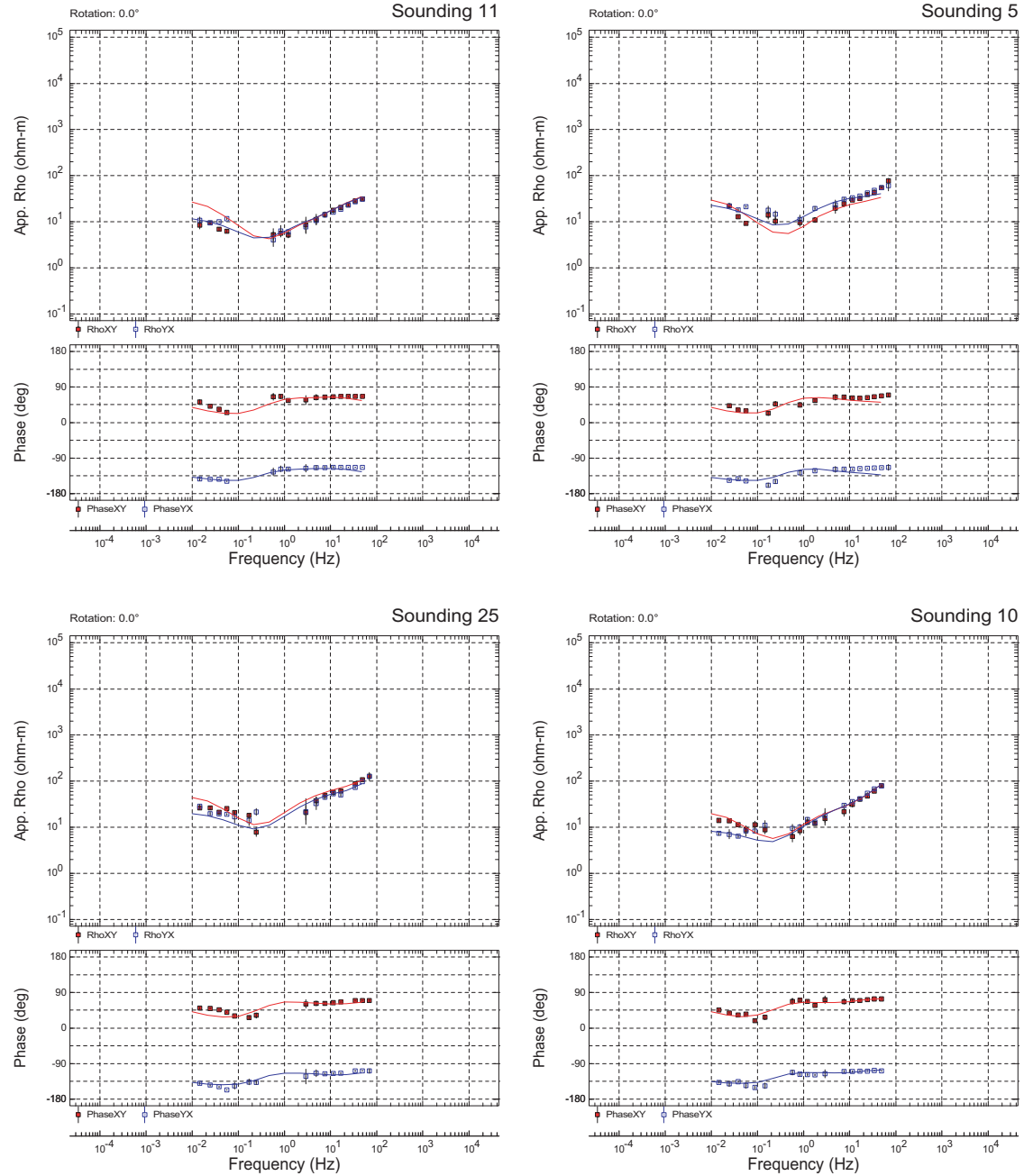


**Figure A20.** Plots of observed (square symbols) and calculated (red and blue lines) magnetotelluric resistivity and phase data at stations 11, 5, 25, and 10 from profile A-A' (Figs. 2A, A14) for 3-D forward finite-element resistivity model. Data rotated to 0° North.

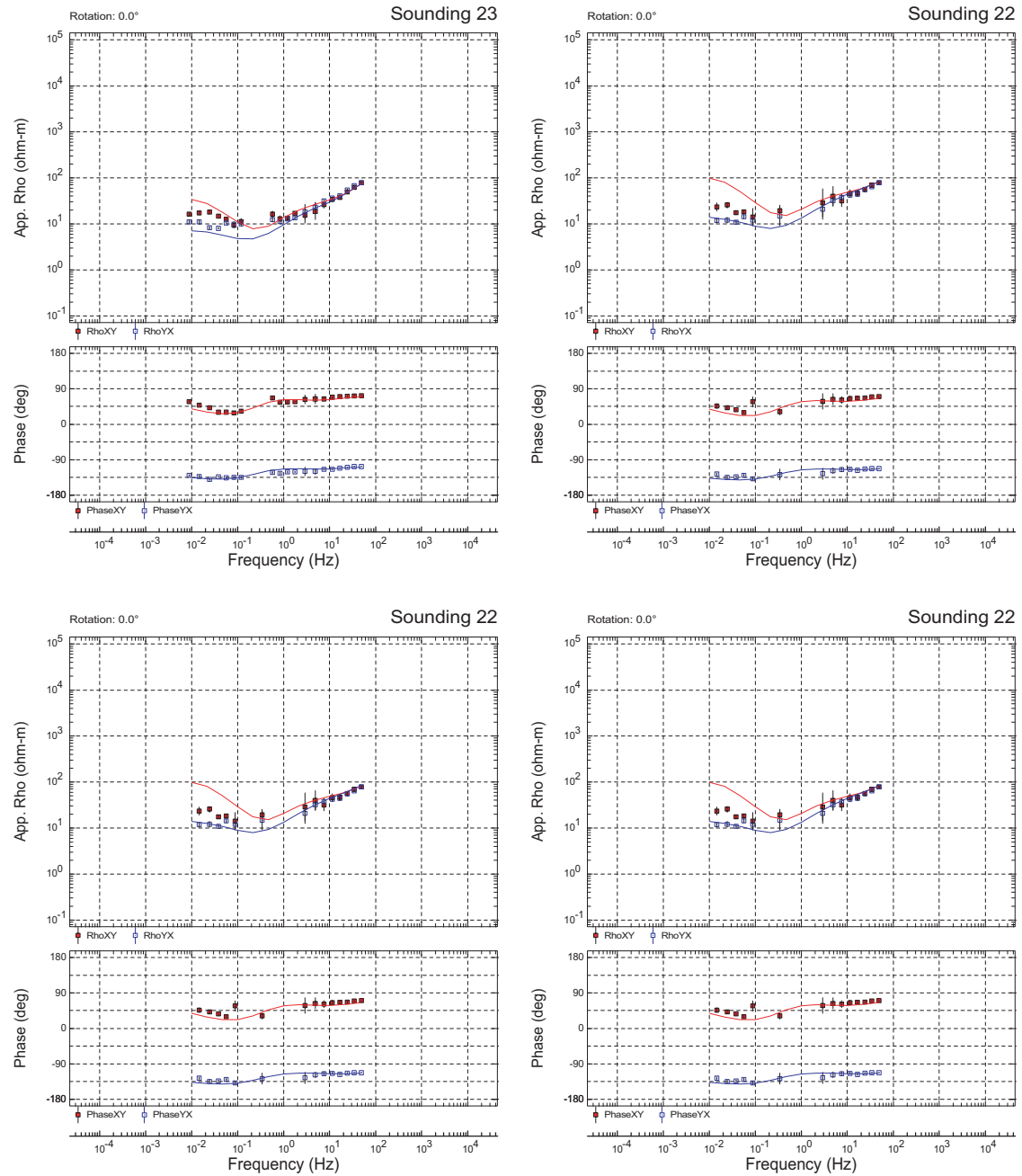


**Figure A21.** Plots of observed (square symbols) and calculated (red and blue lines) magnetotelluric resistivity and phase data at stations 23, 22, 9, and 27 from profile A-A' (Figs. 2A, A14) for 3-D forward finite-element resistivity model. Data rotated to 0° North.

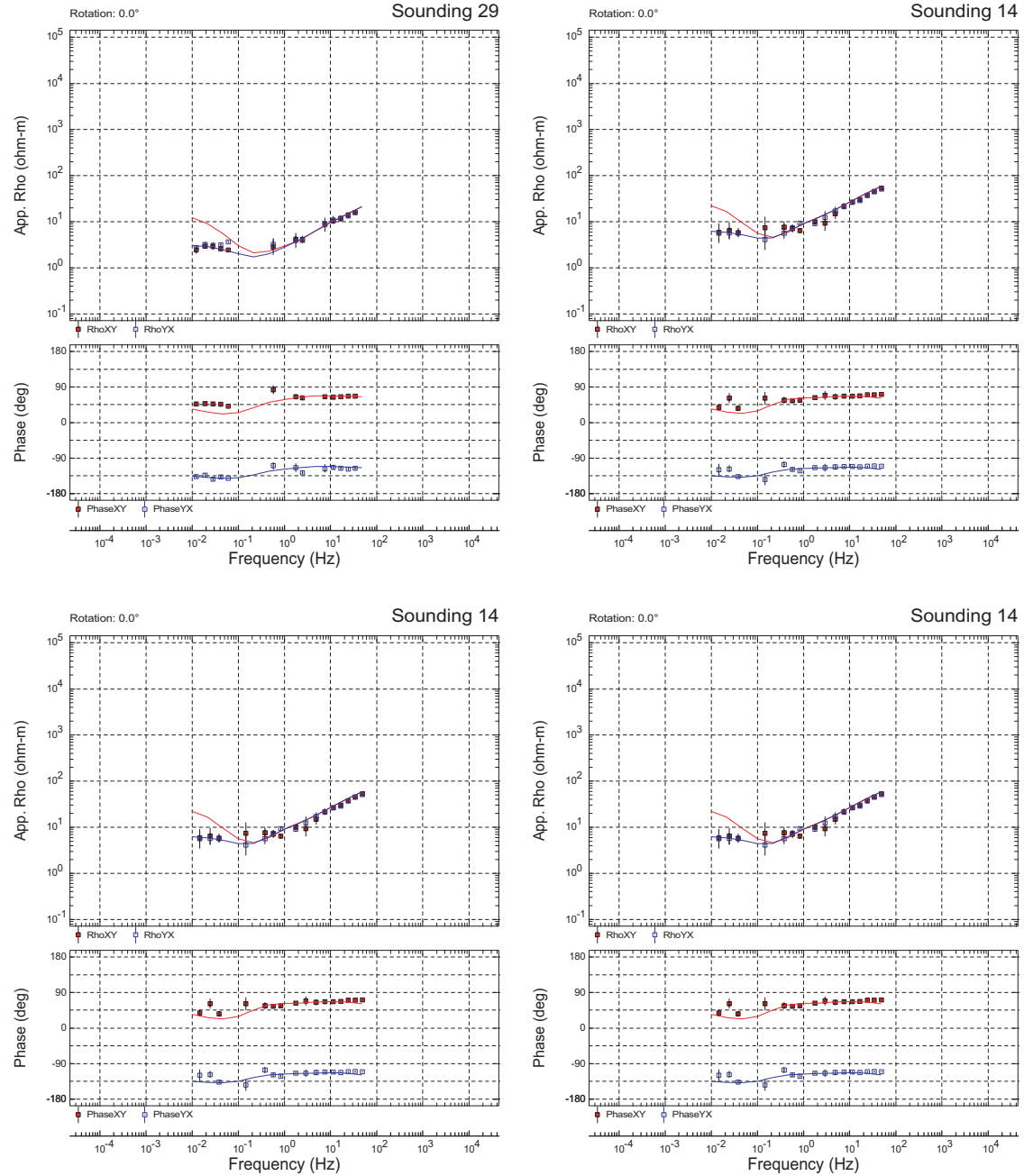


**Figure A22.** Plots of observed (square symbols) and calculated (red and blue lines) magnetotelluric resistivity and phase data at stations 29, 14, 28, and 15 from profile B-B' (Figs. 2A, A15) for 3-D forward finite-element resistivity model. Data rotated to 0° North.

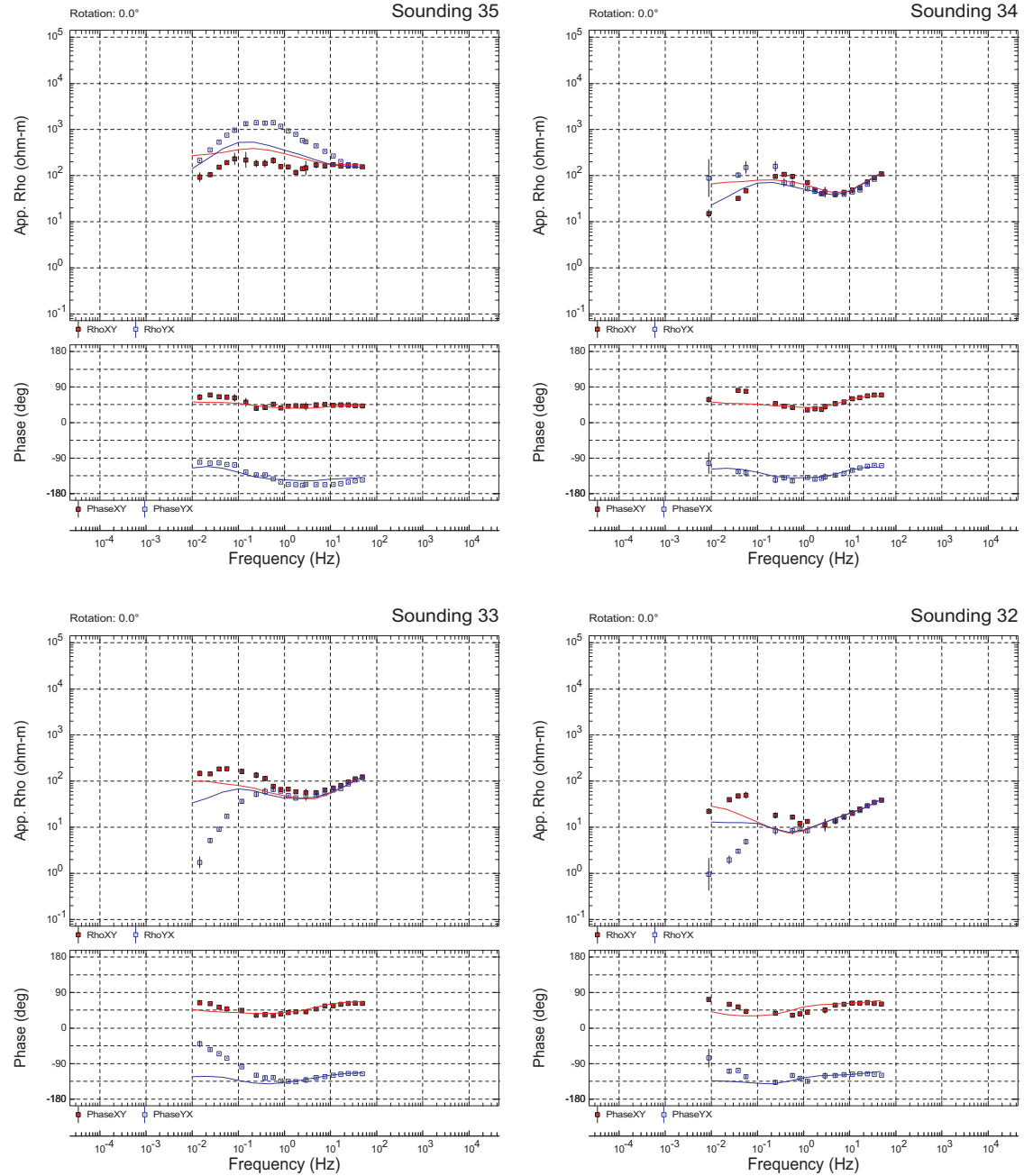


**Figure A23.** Plots of observed (square symbols) and calculated (red and blue lines) magnetotelluric resistivity and phase data at stations 35, 34, 33, and 32 from profile C-C' (Figs. 2A, A16) for 3-D forward finite-element resistivity model. Data rotated to 0° North.

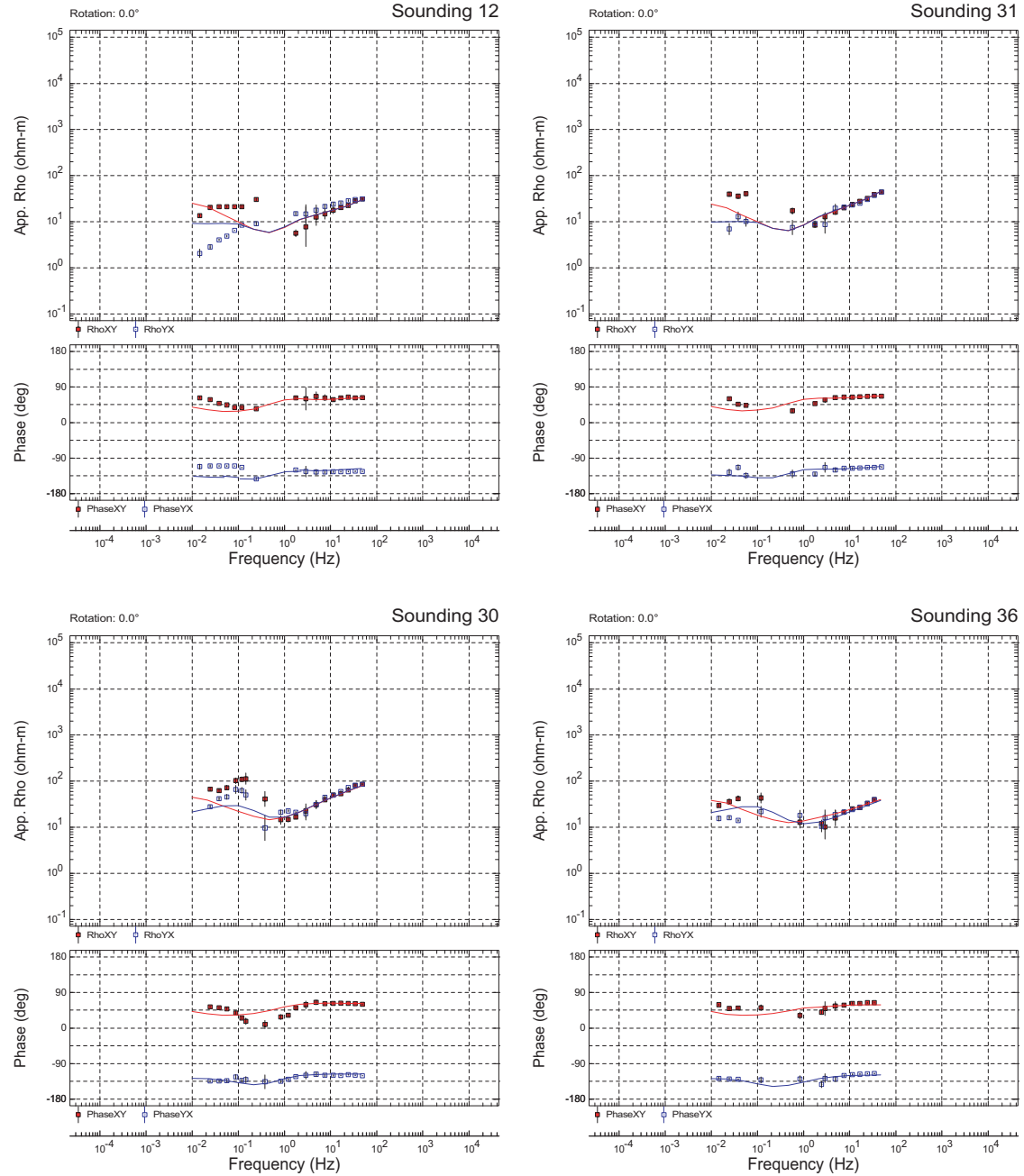


**Figure A24.** Plots of observed (square symbols) and calculated (red and blue lines) magnetotelluric resistivity and phase data at stations 12, 31, 30, and 36 from profile C-C' (Figs. 2A, A16) for 3-D forward finite-element resistivity model. Data rotated to 0° North.

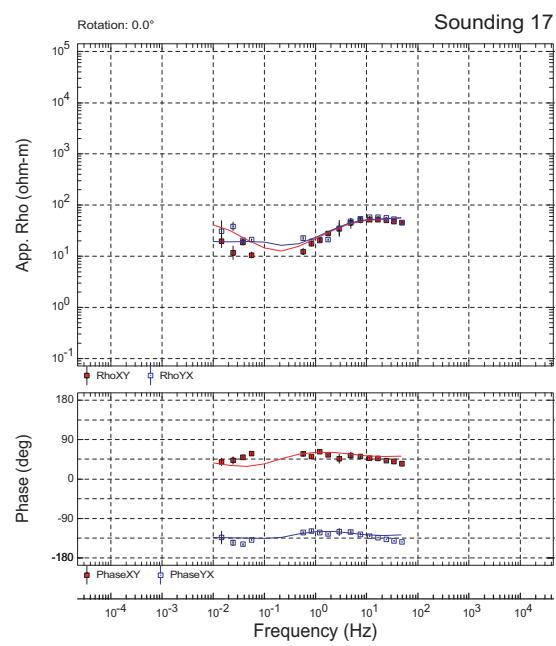


**Figure A25.** Plots of observed (square symbols) and calculated (red and blue lines) magnetotelluric resistivity and phase data at station 17 from profile C-C' (Figs. 2A, A16) for 3-D forward finite-element resistivity model. Data rotated to 0° North.

suggest a north trending ramp instead of an abrupt subvertical structure in the upper km as depicted in the 2-D model and a thicker upper Santa Fe Group (SNTFu) beneath station 15.

Our 2-D model along profile C-C' (Fig. A13) agrees well with the corresponding profile extraction from the 3-D model (Fig. A16), except in the near-surface beneath stations 12, 31, 30, and 36 where the 3-D model suggests more moderate resistivity (about 40 ohm-m) material and more moderate resistivity (about 25 ohm-m) material beneath station 30 from about 1 to 2 km depth. The 3-D model also suggests more conductive (6 ohm-m) material beneath station 32 from about 1 to 2 km depth. The only interpretive change required by these 3-D results is the northwest boundary of the post-Laramide displacement is northwest of station 32 instead of southeast (Fig. 10) and the inferred resistive VLCC in the upper km below station 17 is not required.

In summary, for profiles A-A' and B-B', the primary modifications of the 3-D forward model departure from the initial 2-D model input is a thinning of the conductor sandwich on the northern half of each profile primarily by a deepening of the conductor top, but also a shallowing of the conductor base on profile A-A' (Figs. A14 and A15).

### **3-D Inversion**

To test whether our *a priori* 3-D forward model resistivities are a valid representation beneath each profile, we performed 3-D magnetotelluric inversion using data from profiles A-A', B-B', and C-C'. We used the 3-D magnetotelluric inversion algorithm wsinv3dmt (Siripunvaraporn et al., 2005) using a 100 ohm-m 3-D space for the starting model. It took over 2 months of computation time to invert 12 periods for the 8 tensor impedance components (Real and Imaginary Zxx, Zxy, Zyx, and Zyy), and after 10 iterations the total RMS error reduced by over 700%. With the exception of three magnetotelluric stations, 27, 34, and 35, the off-diagonal impedance, Zxy and Zyx, data misfits are small (Figs. A26 – A30). At station 27 (Fig. A28), data misfits are good for Zyx, but misfits for Zxy at the highest periods inverted are worse. At station 34 (Fig. A29), misfits are also good for Zyx, but worse for Zxy on the highest two-thirds periods inverted. At station 35 (Fig. A28), misfits for both Zxy and Zyx are poor at the highest periods inverted. The misfits for the diagonal impedance components, Zxx and Zyy, are generally larger than the misfits for the off-diagonal components, Zxy and Zyx. At station 34 (Fig. A29) and station 36 (Fig. A30), the worse misfit is at period 0.09 seconds for Zxx at station 34 and Zyy at station 36, where the observed diagonal impedance component is very small. At station 35 (Fig. A28), the worse misfits are at periods 11 to 41 seconds for Zyy. At station 8 (Fig. A26), misfits for both Zxy and Zyy are worse for periods 0.02 to 1.2 seconds.

Overall, off-diagonal impedance, Zxy and Zyx, data misfits are generally good, but larger for the northern stations. Diagonal impedance, Zxx and Zyy, misfits are generally worse and larger for the western stations. In terms of the north-south component, Zxy, of the 3-D resistivity inversion, with the exception of station 27 noted above, the along profile resistivities of profiles A-A' (Fig. A31) and B-B' (Fig. A32) are good representations of the 3-D geology. The high period Zxy misfit undershoot at station 27 (Fig. A28) suggests higher resistivities north of station 27. The off-profile 3-D resistivities are generally poor for all stations and especially poor for the northwest stations, 34 and 35 along profile C-C' (Fig. A33), near the Valles caldera (Fig. 2A). The 3-D resistivity inversion results along profile A-A' (Fig. A31) suggest that the 2-D transverse magnetic mode model and the 3-D forward model are in general agreement except beneath station 27 where the 3-D inversion suggests that the conductor below 1 km depth may be thicker than interpreted by the 2-D transverse magnetic mode model or the 3-D forward model.

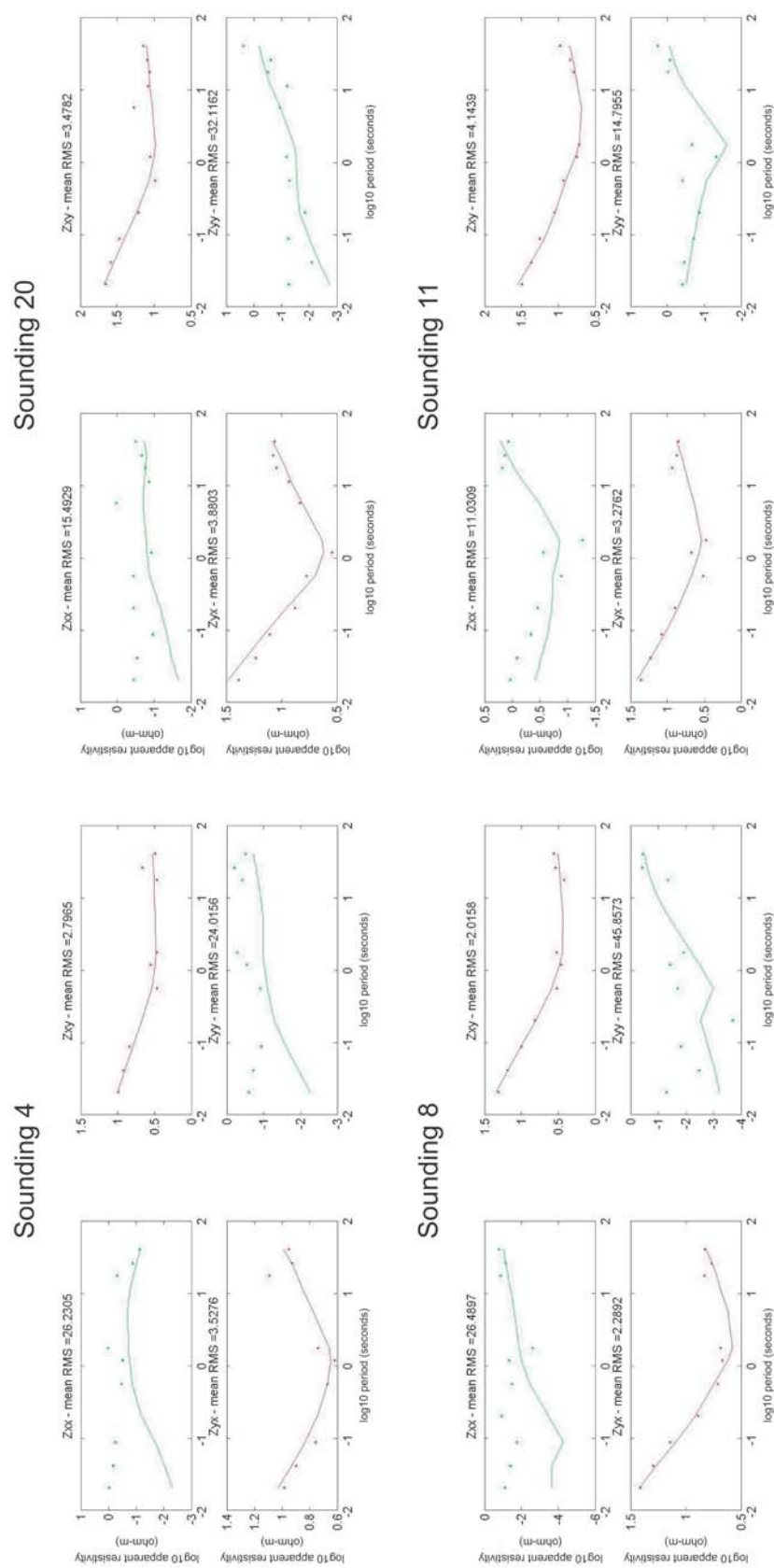


**Figure A26.** Plots of observed (symbols) and inverted response (lines) impedance components ( $Z_{xx}$ ,  $Z_{xy}$ ,  $Z_{yx}$ , and  $Z_{yy}$ ) at stations 4, 20, 8, and 11 from profile A-A' (Figs. 2A, A31) for 3-D inversion resistivity model. Data rotated to 0° North. RMS is root mean square error for each impedance component.

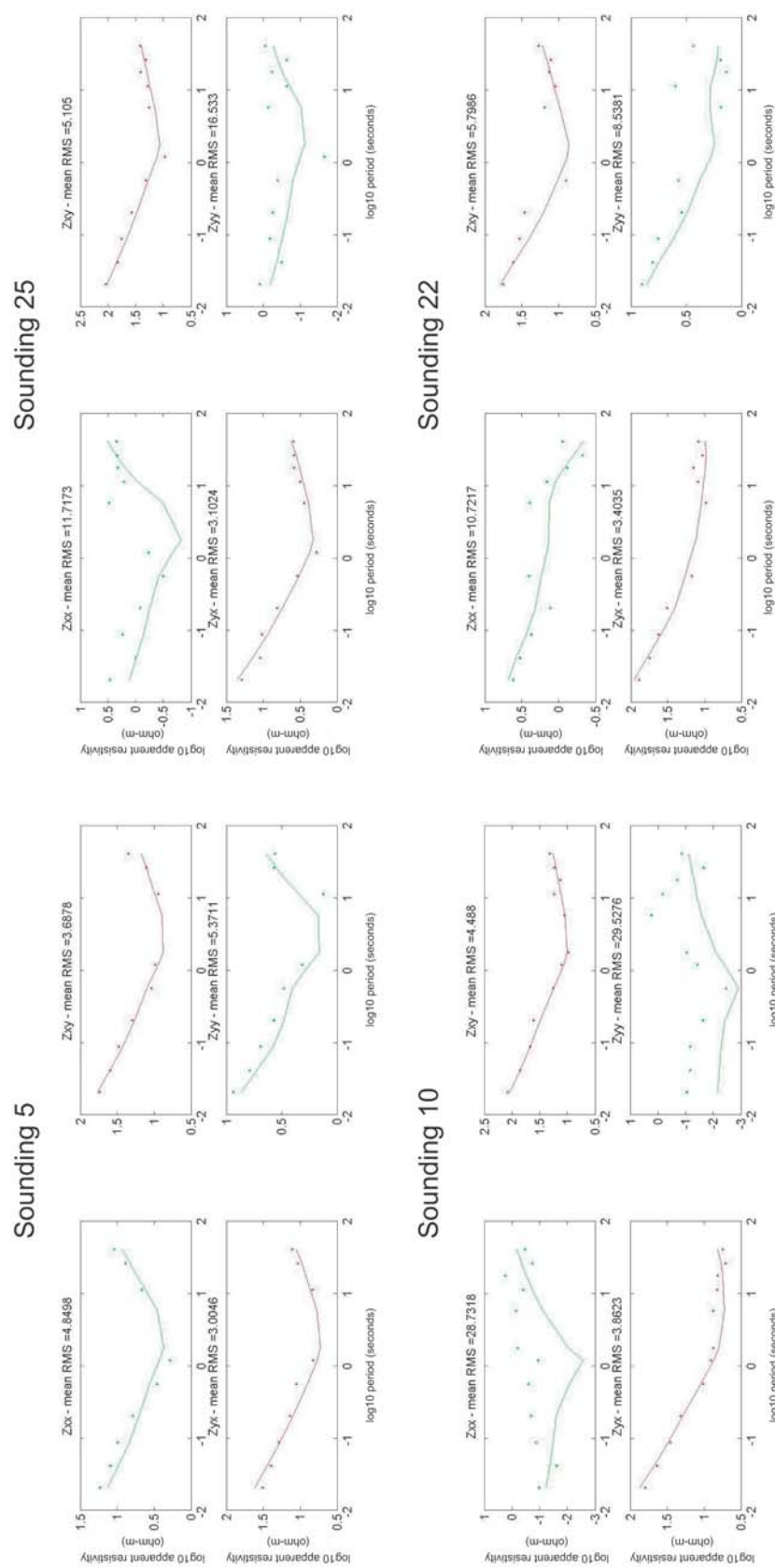


**Figure A27.** Plots of observed (symbols) and inverted response (lines) impedance components ( $Z_{xx}$ ,  $Z_{xy}$ ,  $Z_{yx}$ , and  $Z_{yy}$ ) at stations 5, 10, and 22 from profile A-A' (Figs. 2A, A31) for 3-D inversion resistivity model. All other details same as Figure A26.

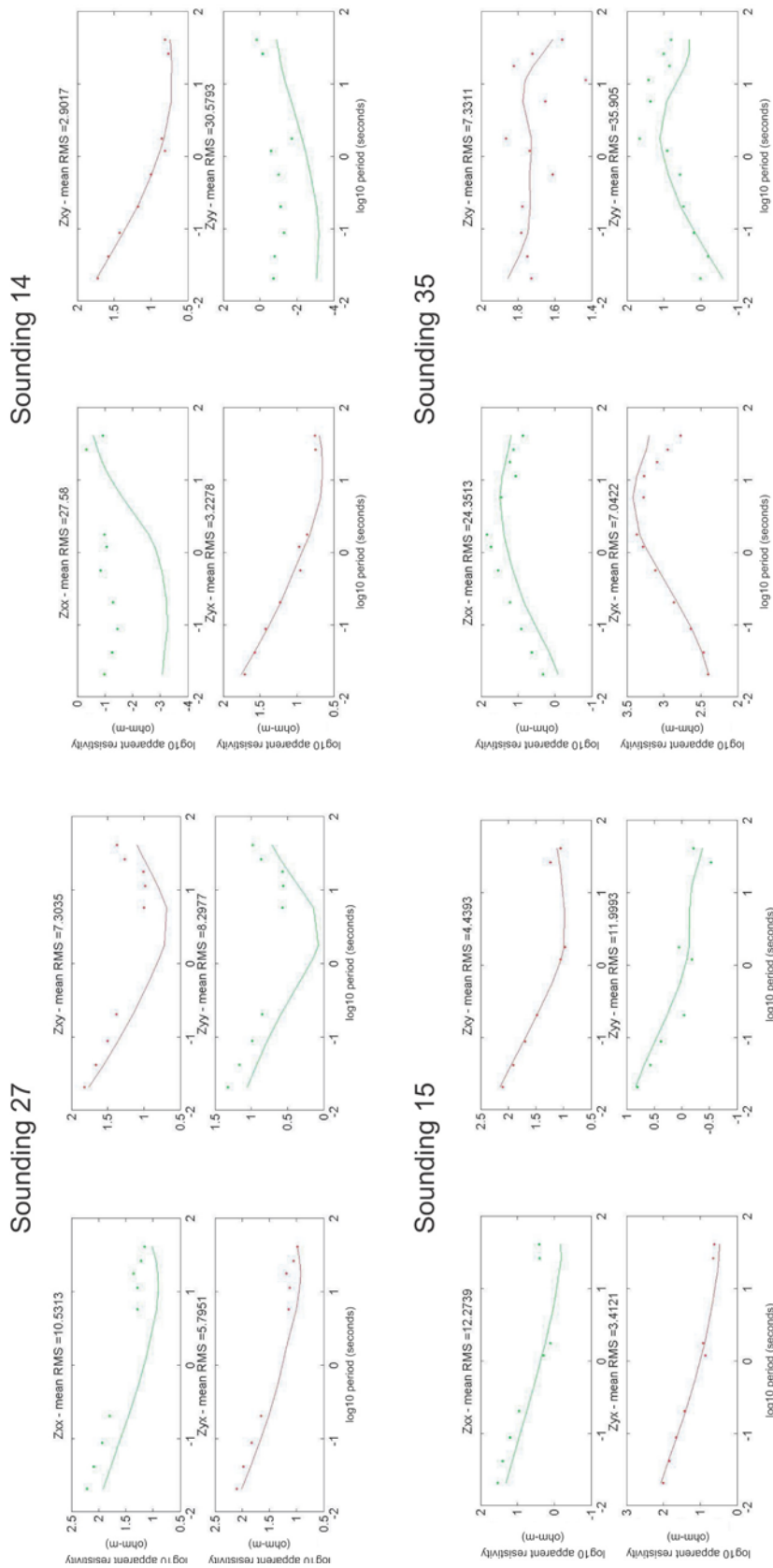


**Figure A28.** Plots of observed (symbols) and inverted response (lines) impedance components ( $Z_{xx}$ ,  $Z_{xy}$ ,  $Z_{yx}$ , and  $Z_{yy}$ ) at station 27 from profile A-A', 14 and 15 from profile B-B', and 35 from profile C-C' (Figs. 2A, A31-A33) for 3-D inversion resistivity model. All other details same as Figure A26.

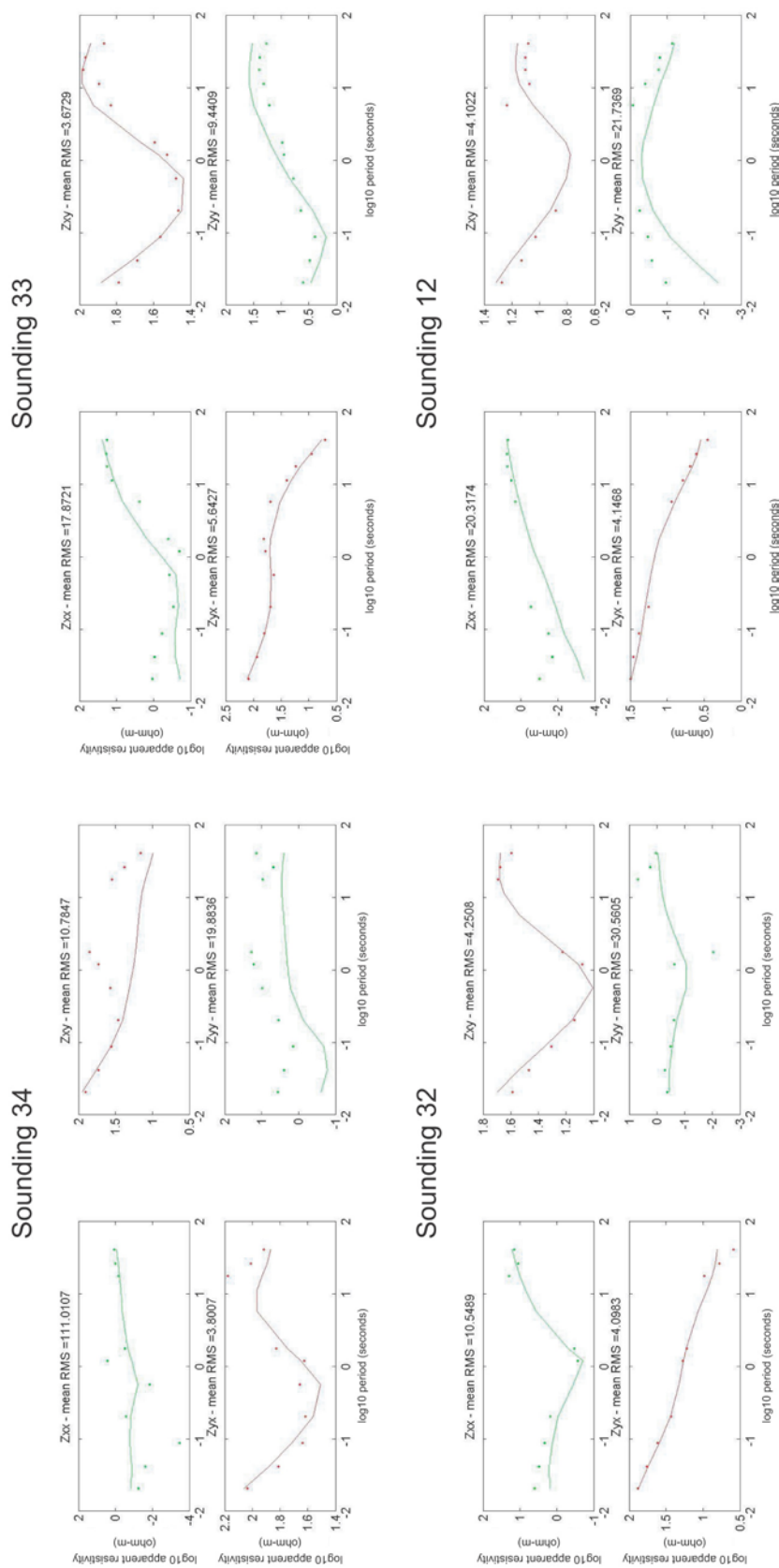


**Figure A29.** Plots of observed (symbols) and inverted response (lines) impedance components ( $Z_{xx}$ ,  $Z_{xy}$ ,  $Z_{yx}$ , and  $Z_{yy}$ ) at stations 34, 33, 32, and 12 from profile C-C' (Figs. 2A, A33) for 3-D inversion resistivity model. All other details same as Figure A26.

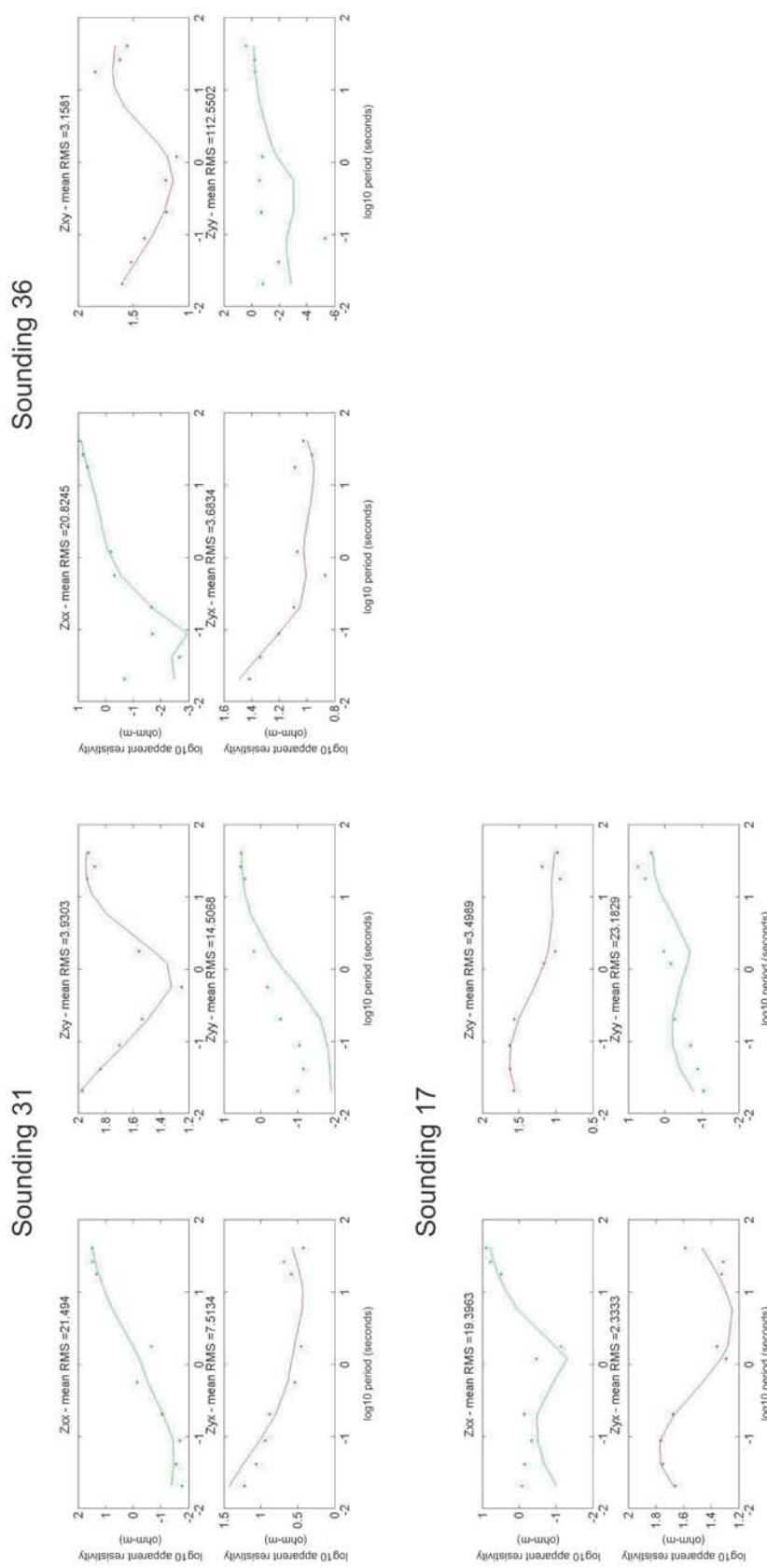


**Figure A30.** Plots of observed (symbols) and inverted response (lines) impedance components ( $Z_{xx}$ ,  $Z_{xy}$ ,  $Z_{yx}$ , and  $Z_{yy}$ ) at stations 31, 36, and 17 from profile C-C' (Figs. 2A, A33) for 3-D inversion resistivity model. All other details same as Figure A26.

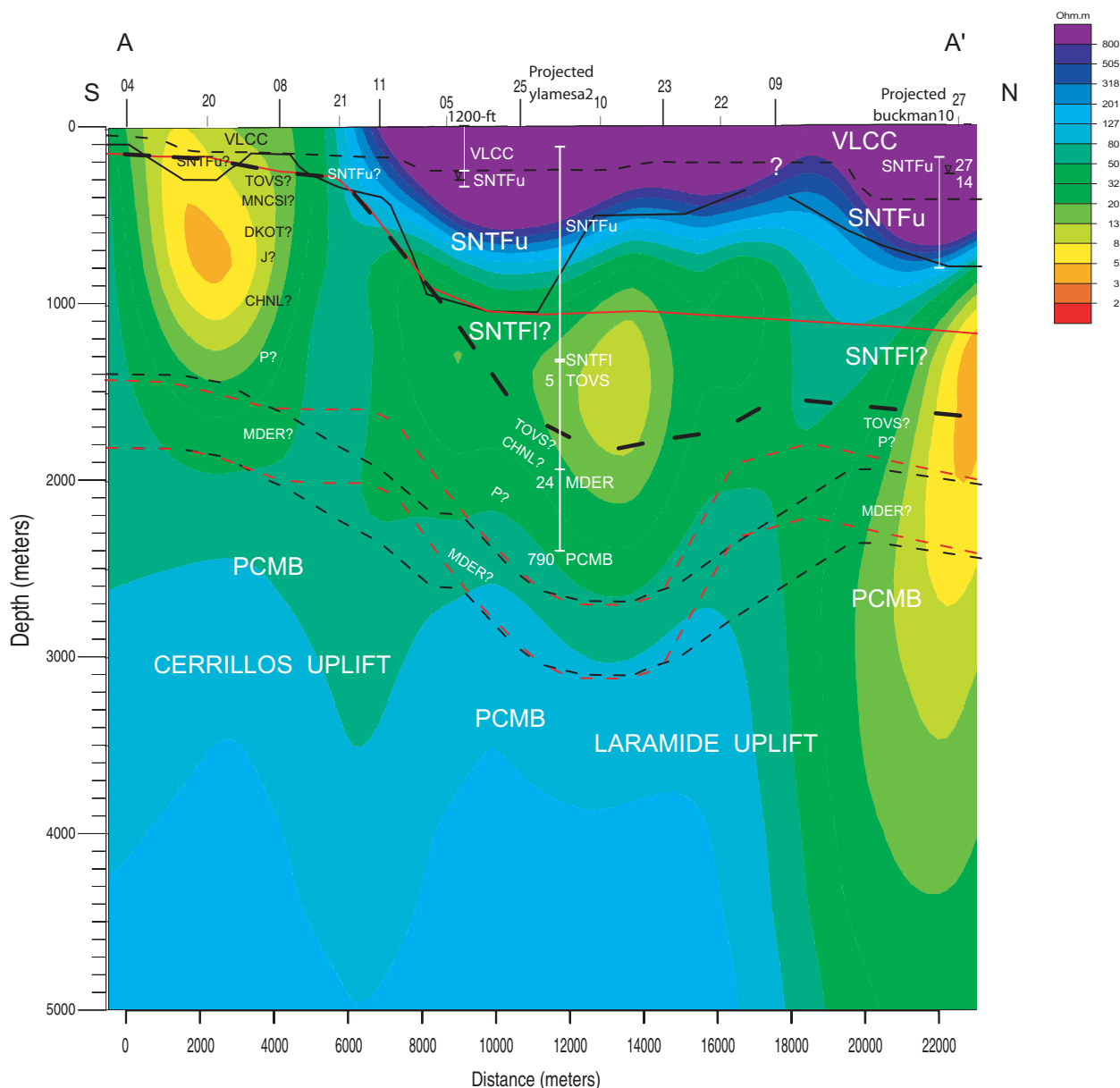


**Figure A31.** Profile A-A' (Fig. 2A) resistivity section extracted from 3-D inversion resistivity model with lithologic interpretation. Numbered labels at top of model are magnetotelluric station numbers. Thick black dashed line is basin floor model from Grauch et al. (2009). Black solid lines are interpreted major geologic boundaries (dashed where poorly constrained by magnetotelluric data) from two-dimensional resistivity model (Fig. A11). Red lines are revised interpreted major geologic boundaries (dashed where poorly constrained by magnetotelluric data) from 3-D forward resistivity model. See Table 1 for well shortname key. See Table 2 for geologic symbol key. Vertical exaggeration is about 5.

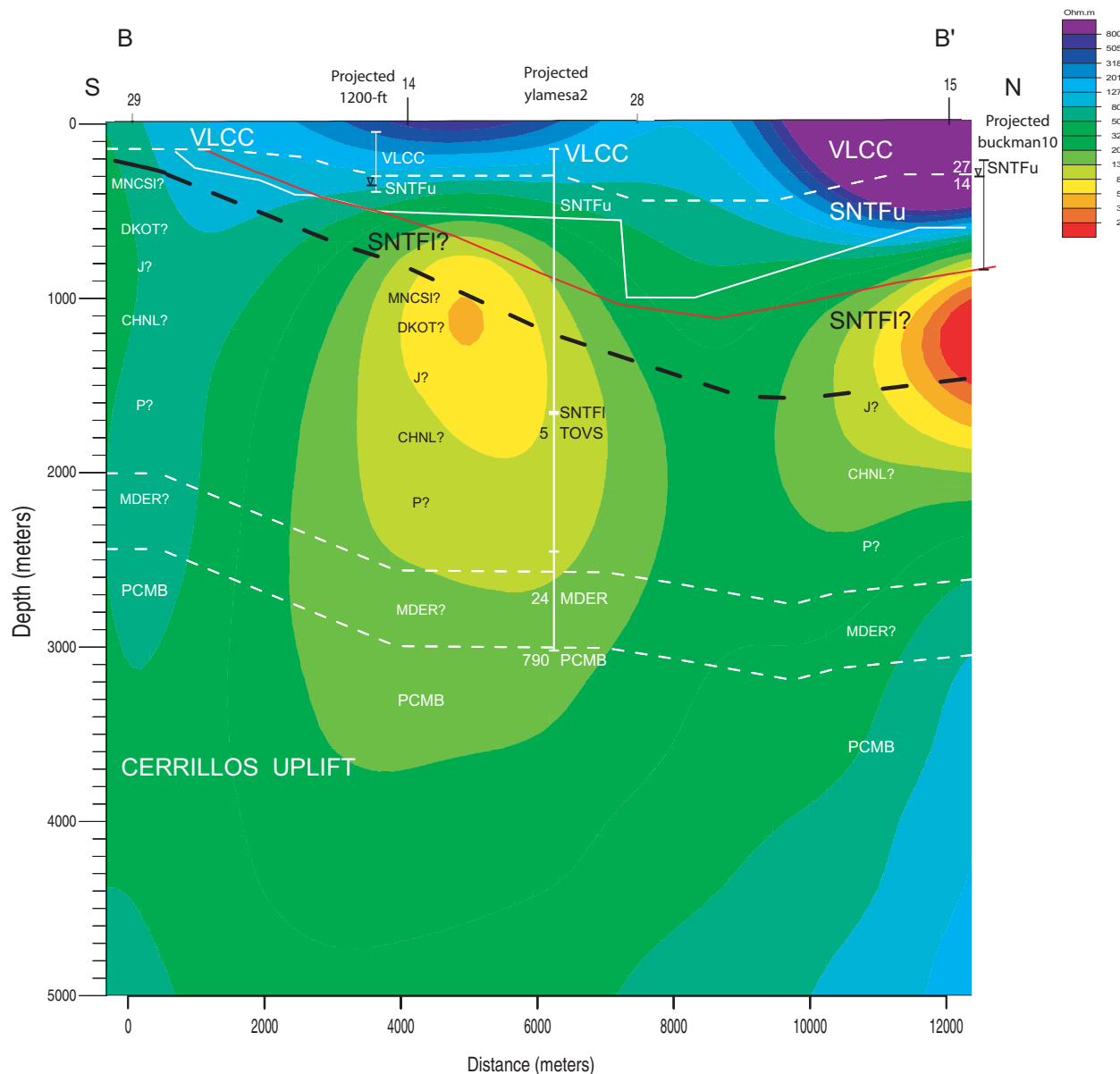


**Figure A32.** Profile B-B' (Fig. 2A) resistivity section extracted from 3-D inversion resistivity model with lithologic interpretation. Black solid lines are interpreted major geologic boundaries (dashed where poorly constrained by magnetotelluric data) from two-dimensional resistivity model (Fig. A12). Vertical exaggeration is about 3. All other details same as Figure A31.

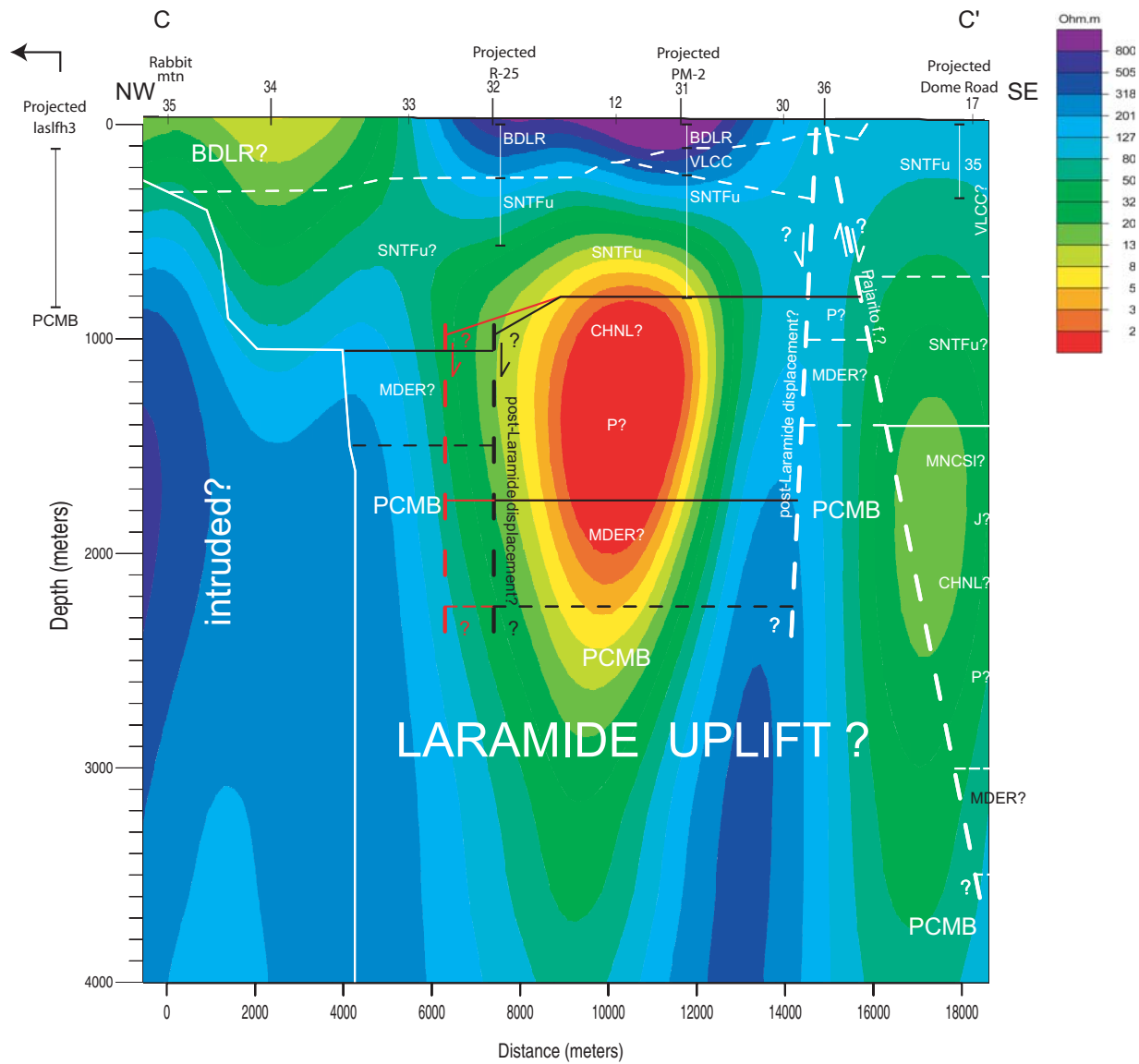


**Figure A33.** Profile C-C' (Fig. 2A) resistivity section extracted from 3-D inversion resistivity model with lithologic interpretation. Black solid lines are interpreted major geologic boundaries (dashed where poorly constrained by magnetotelluric data) from two-dimensional resistivity model (Fig. A13). Vertical exaggeration is about 5. All other details same as Figure A31.

For profile B-B' (Fig. A32), the 3-D inversion is in general agreement with the 2-D model and 3-D forward model for stations 14 and 15 (stations 28 and 29 are not included in the 3-D inversion). For profile C-C' (Fig. A33), the 3-D inversion is in general agreement with the 2-D model and 3-D forward model, except for shallow resistivities beneath stations 34 and 35 where one impedance component ( $Z_{yy}$  for station 34, Fig. A29;  $Z_{xx}$  for station 35, Fig. A28) is underfit at the smallest periods that may correlate with the model disagreement in the upper 500 m. The conductor beneath station 12 is thicker in the 3-D inversion than in the 2-D model or 3-D forward model, but the  $Z_{yy}$  impedance component is underfit in the 3-D inversion, so there is not justification to change the interpretations, described above, provided by the integration of the 2-D model and 3-D forward model.

### Borehole Data

Digitized induction logs for regional boreholes illustrated in figures A34-A61. Mean, minimum, and maximum resistivity values are given in Table 2 and stratigraphic groups and depth picks for all boreholes are given in Table A3 (oversized; see separate PDF file, Rodriguez\_Table\_A3.pdf).

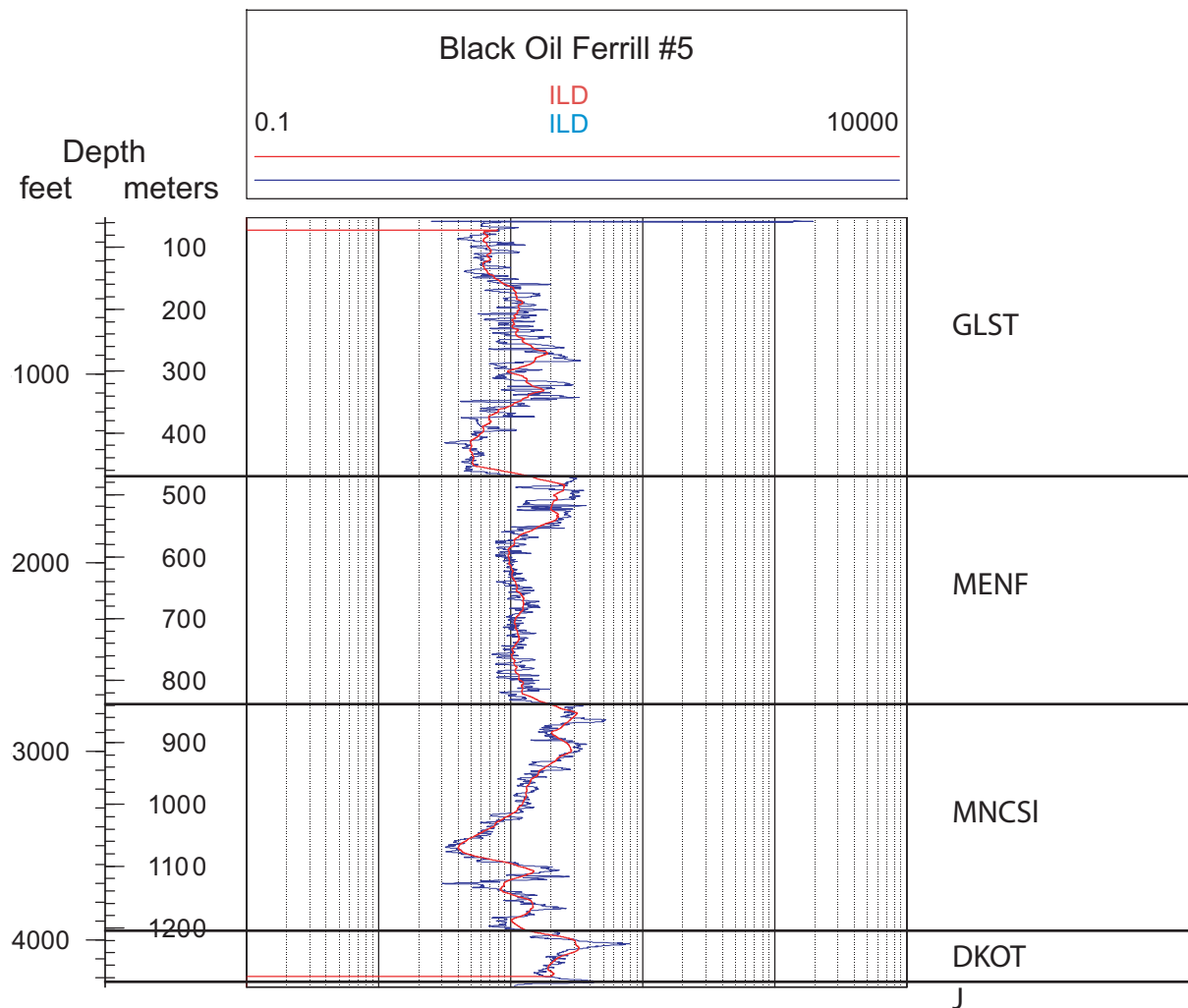


**Figure A34.** Wildcat well Black Oil Ferrill #5 (Fig. 2A, blkferl5 in Tables 1 and A3) deep induction log resistivity (ILD) (blue line) in ohm-m. Red line is 30-m moving average of ILD.

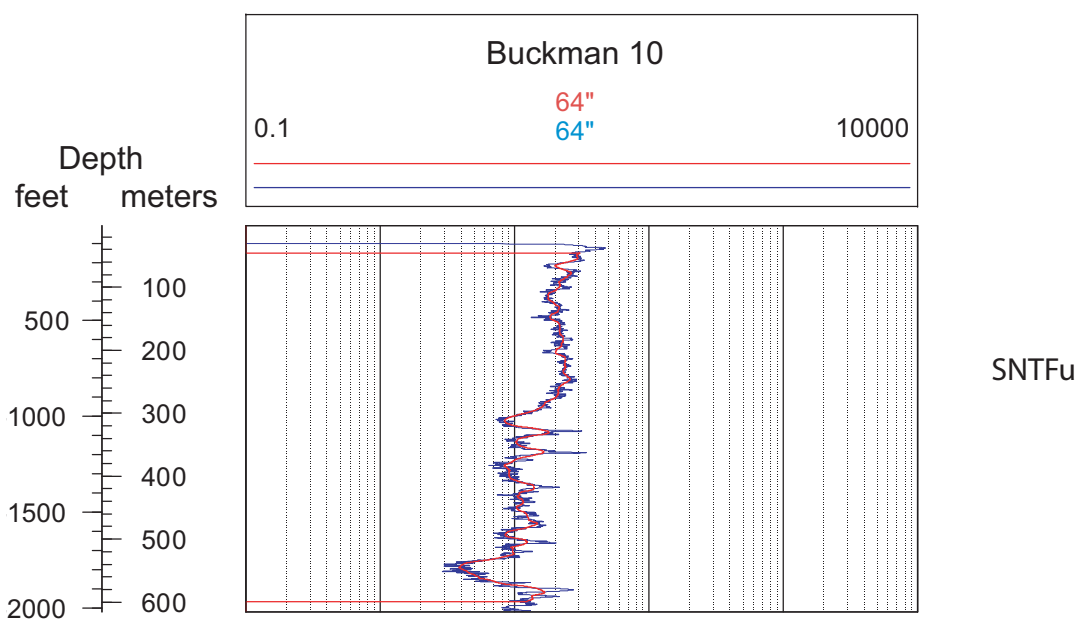


**Figure A35.** Water well Buckman R10 (Fig. 2A, buckman10 in Tables 1 and A3) 64" (1.6 m) deep log resistivity (blue line) in ohm-m. Red line is 30-m moving average of 64" resistivity.

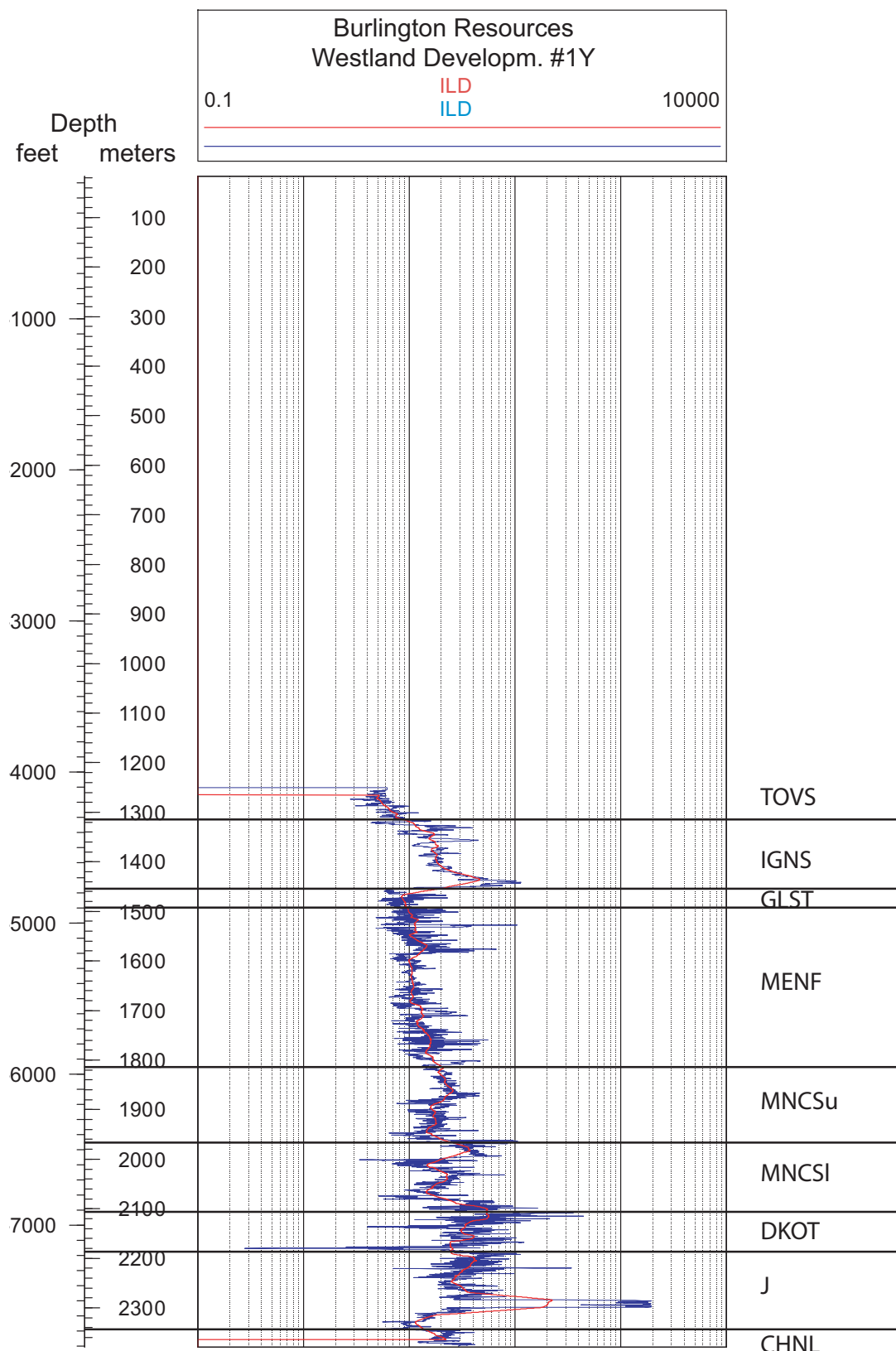


**Figure A36.** Wildcat well Burlington Resources Westland Development #1Y (Fig. 2B, burwes1y in Tables 1 and A3) deep induction log resistivity (ILD) (blue line) in ohm-m. Red line is 30-m moving average of ILD.

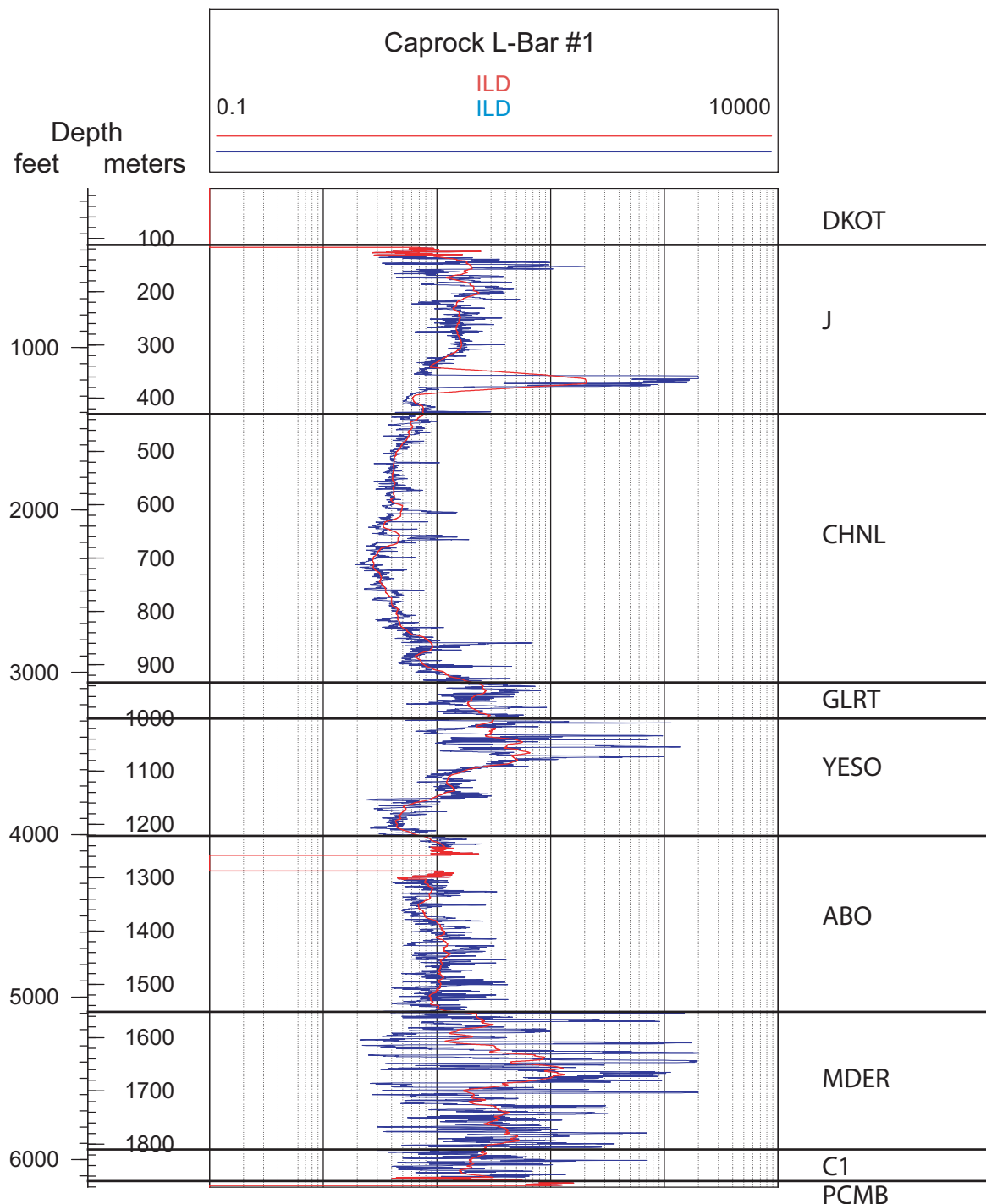


**Figure A37.** Wildcat well Caprock Pipe & Supply L-Bar #1 (Fig. 1, caplbar1 in Tables 1 and A3) deep induction log resistivity (ILD) (blue line) in ohm-m. Red line is 30-m moving average of ILD.

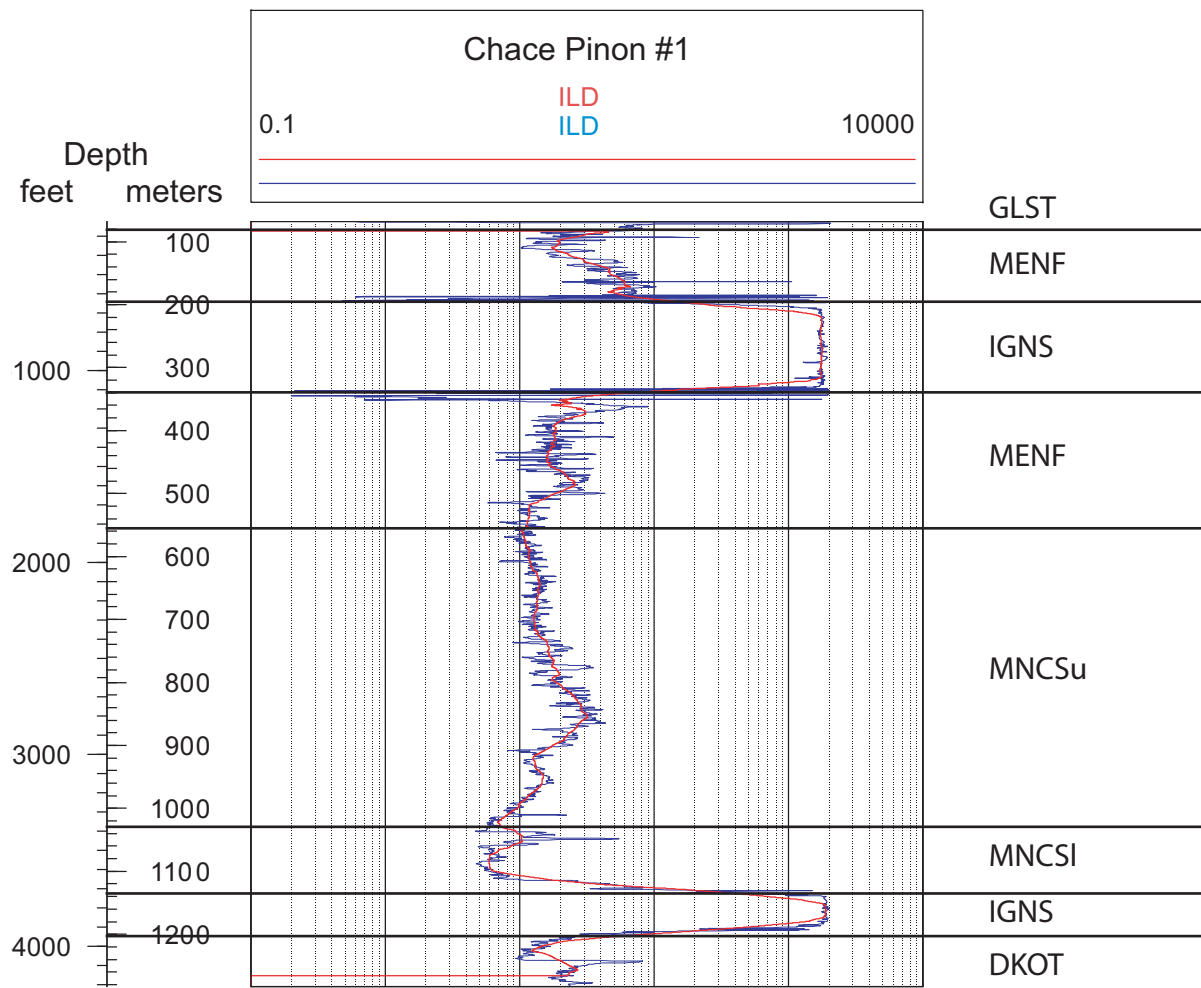


**Figure A38.** Wildcat well Chace Oil Pinon Unit #1 (Fig. 2A, *chacpin1* in Tables 1 and A3) deep induction log resistivity (ILD) (blue line) in ohm-m. Red line is 30-m moving average of ILD.

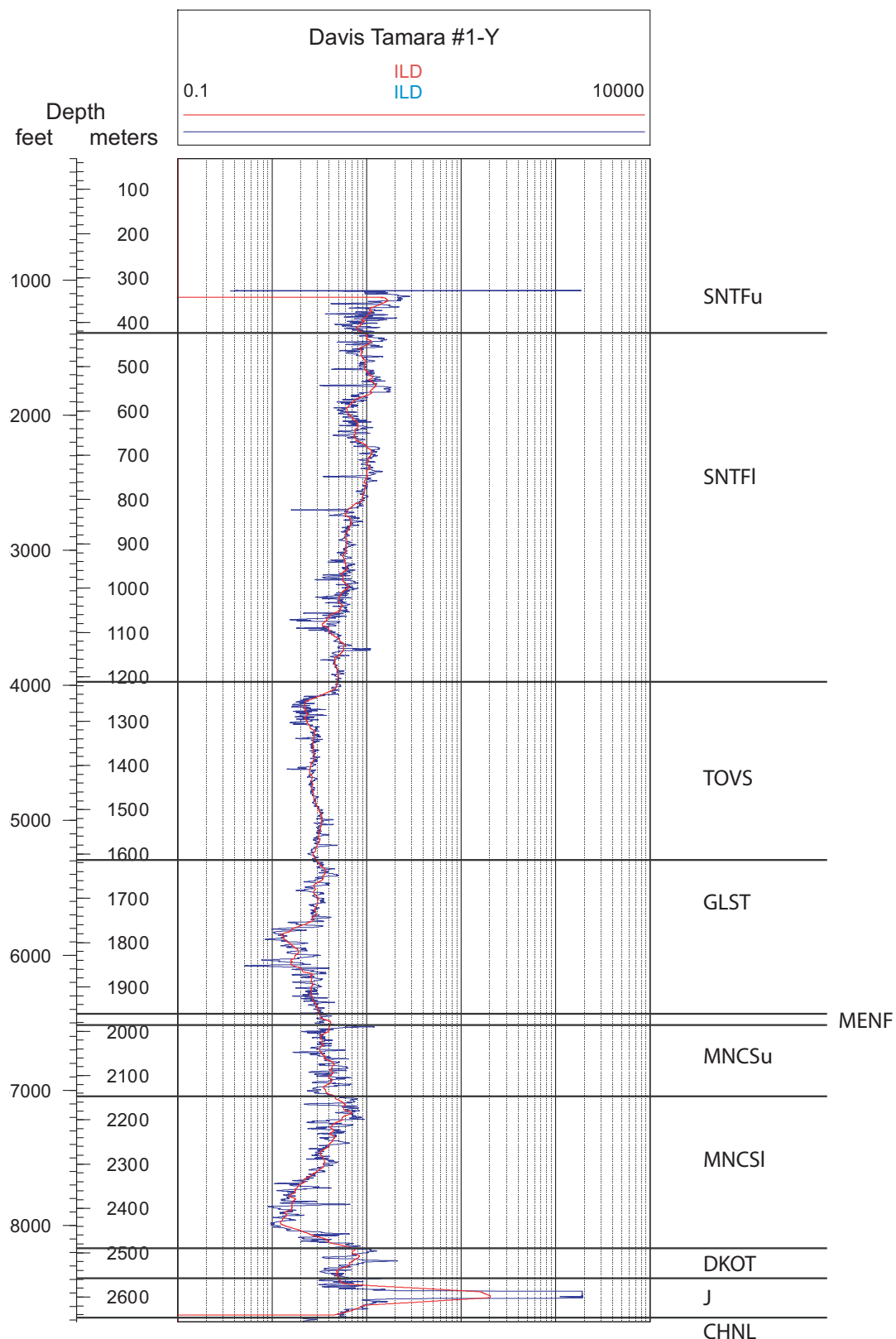


**Figure A39.** Wildcat well Davis Petroleum Tamara #1Y (Fig. 1, davtam1y in Tables 1 and A3) deep induction log resistivity (ILD) (blue line) in ohm-m. Red line is 30-m moving average of ILD.

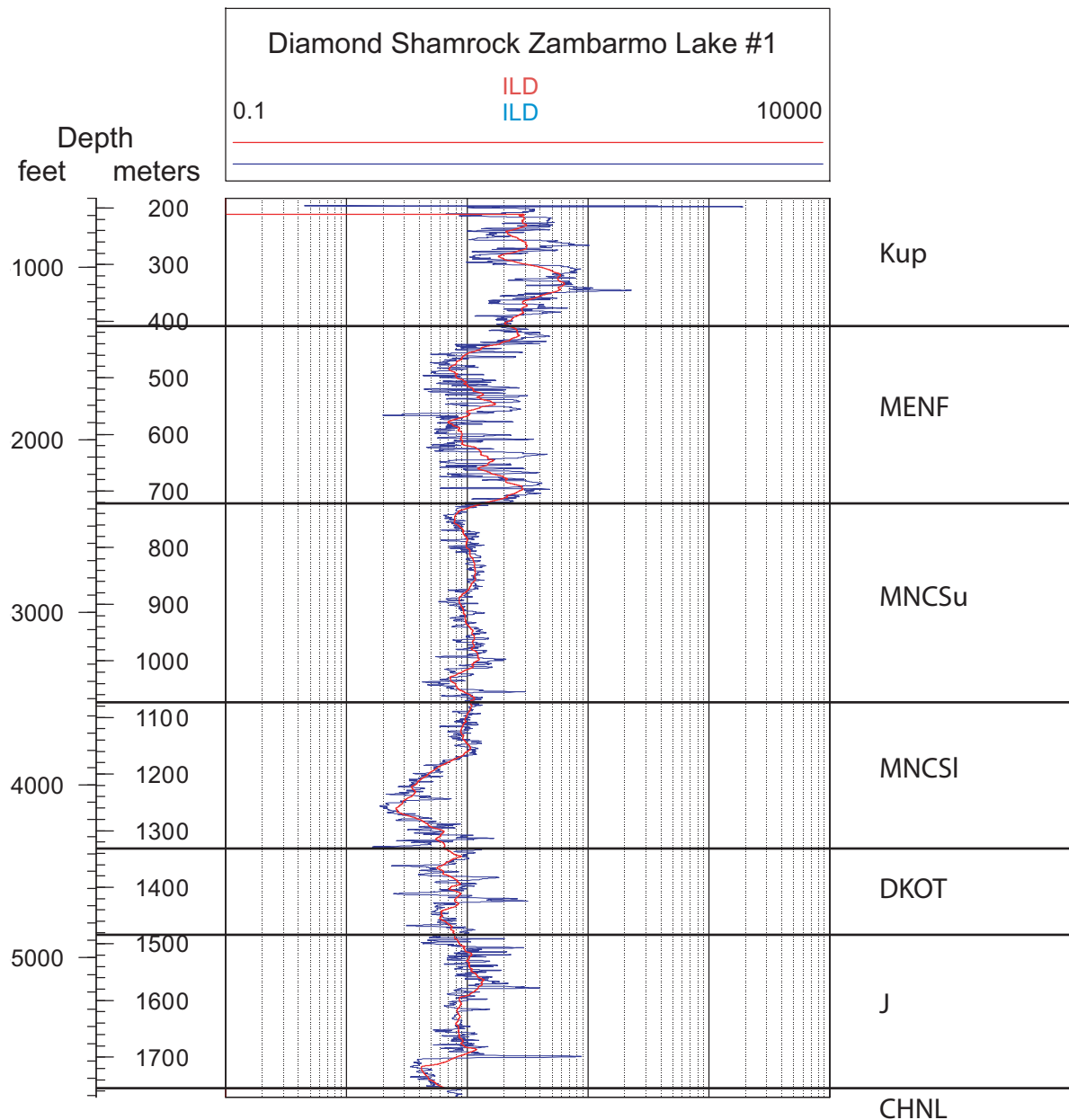


**Figure A40.** Wildcat well Diamond Shamrock Zambarmo Lake 41-18Y (Fig. 1, dszamlk1 in Tables 1 and A3) deep induction log resistivity (ILD) (blue line) in ohm-m. Red line is 30-m moving average of ILD.

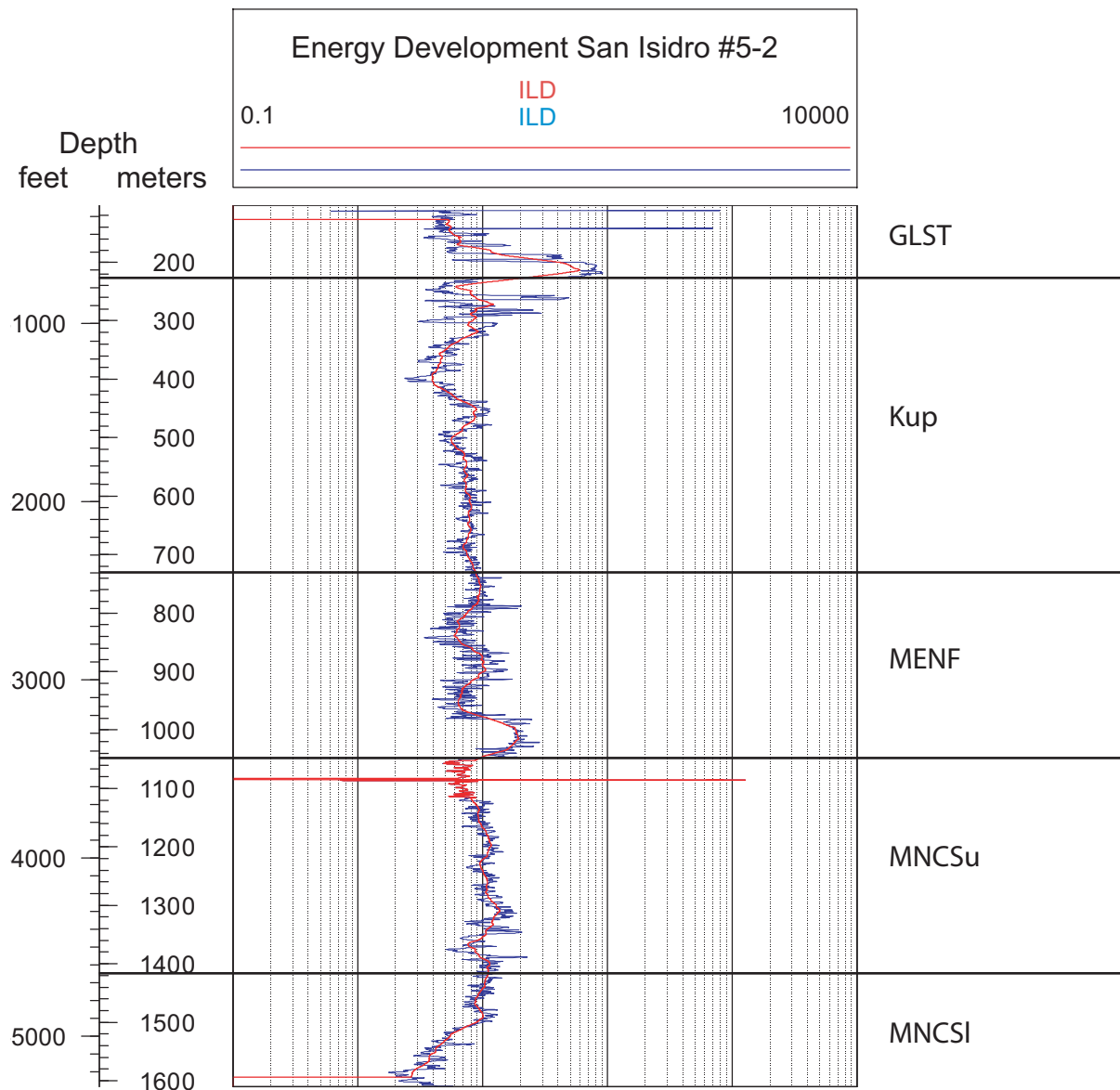


**Figure A41.** Wildcat well Energy Development San Isidro 5-2 (Fig. 1, edsani52 in Tables 1 and A3) deep induction log resistivity (ILD) (blue line) in ohm-m. Red line is 30-m moving average of ILD.

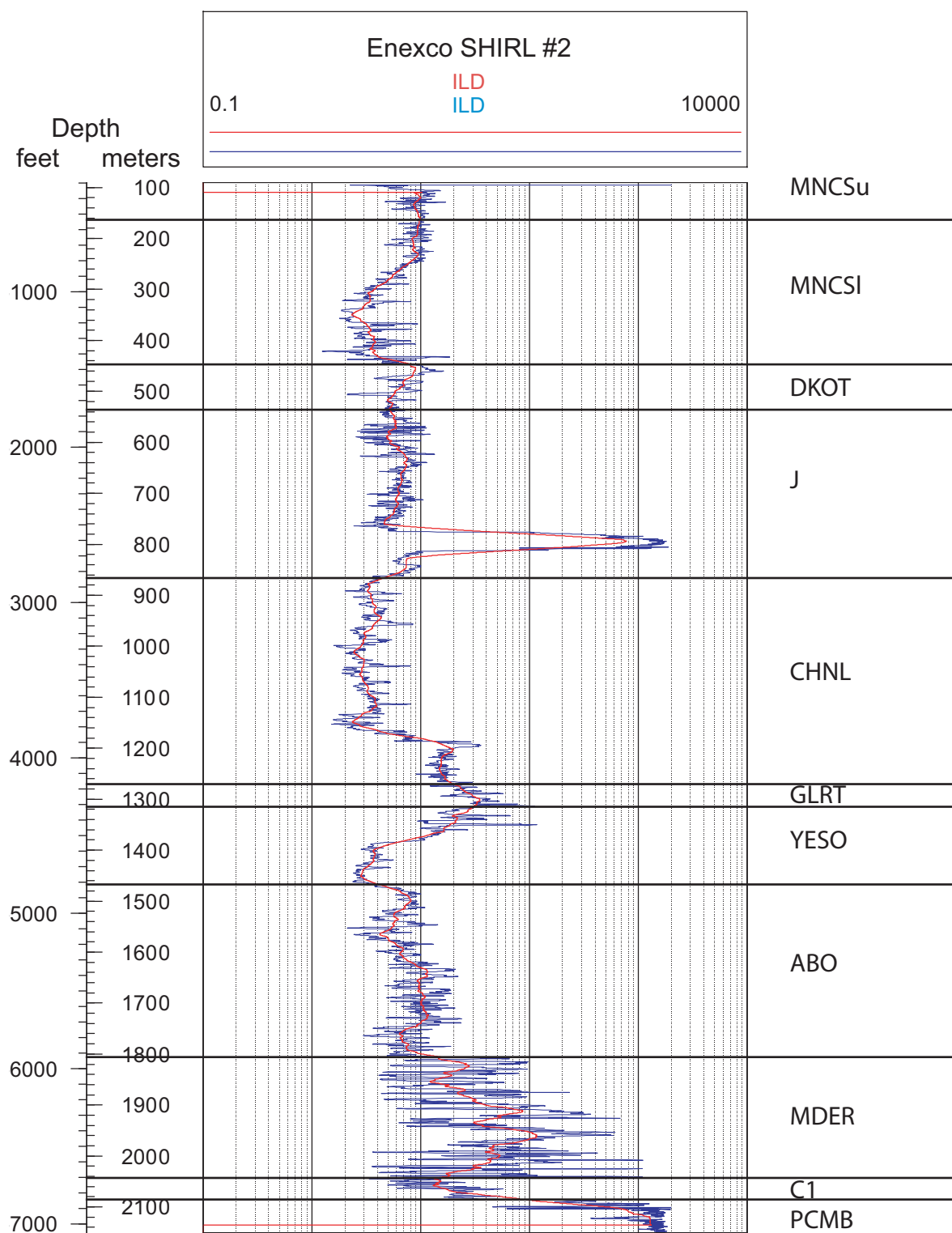


**Figure A42.** Wildcat well Enexco Shirl #2 (Fig. 1, enxshrl2 in Tables 1 and A3) deep induction log resistivity (ILD) (blue line) in ohm-m. Red line is 30-m moving average of ILD.

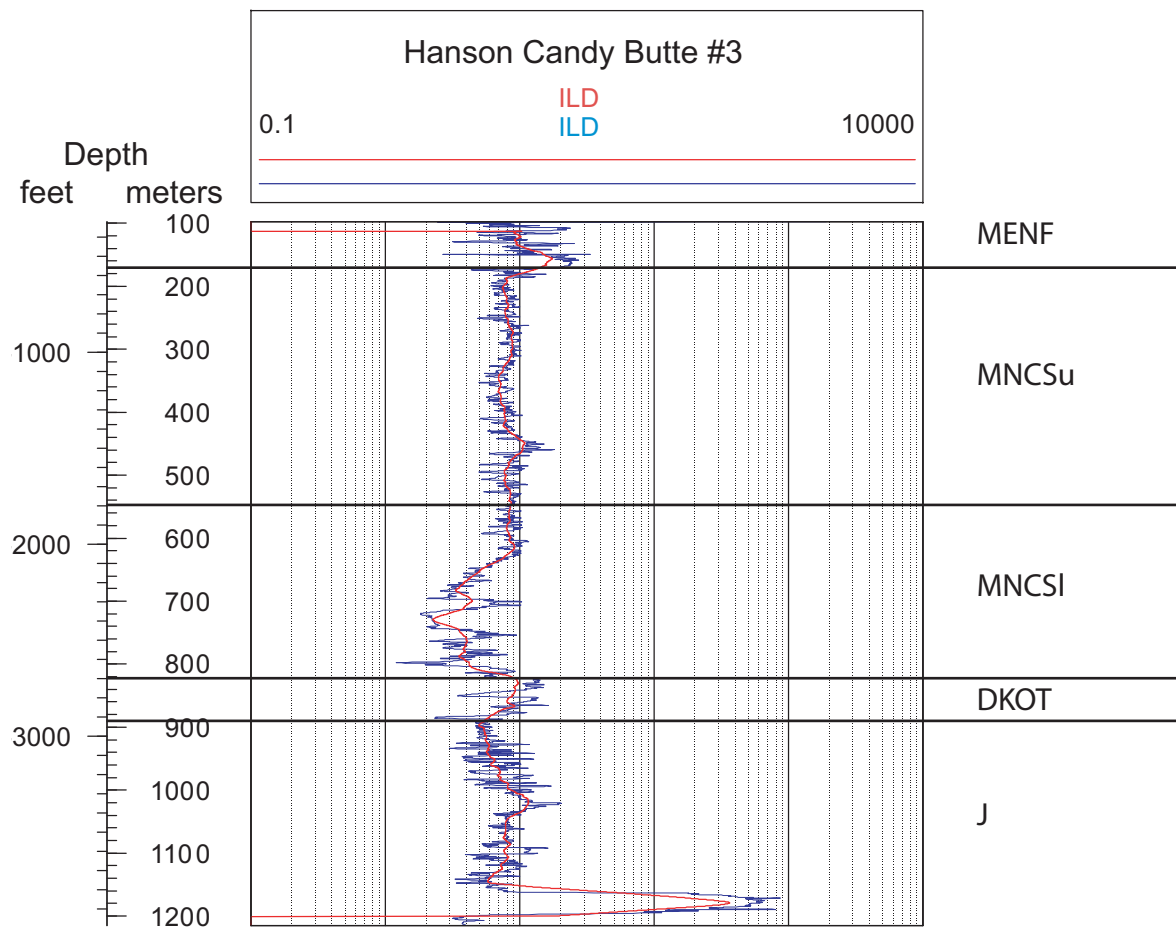


**Figure A43.** Wildcat well Hanson Candy Butte #3 (Fig. 1, hancanb3 in Tables 1 and A3) deep induction log resistivity (ILD) (blue line) in ohm-m. Red line is 30-m moving average of ILD.

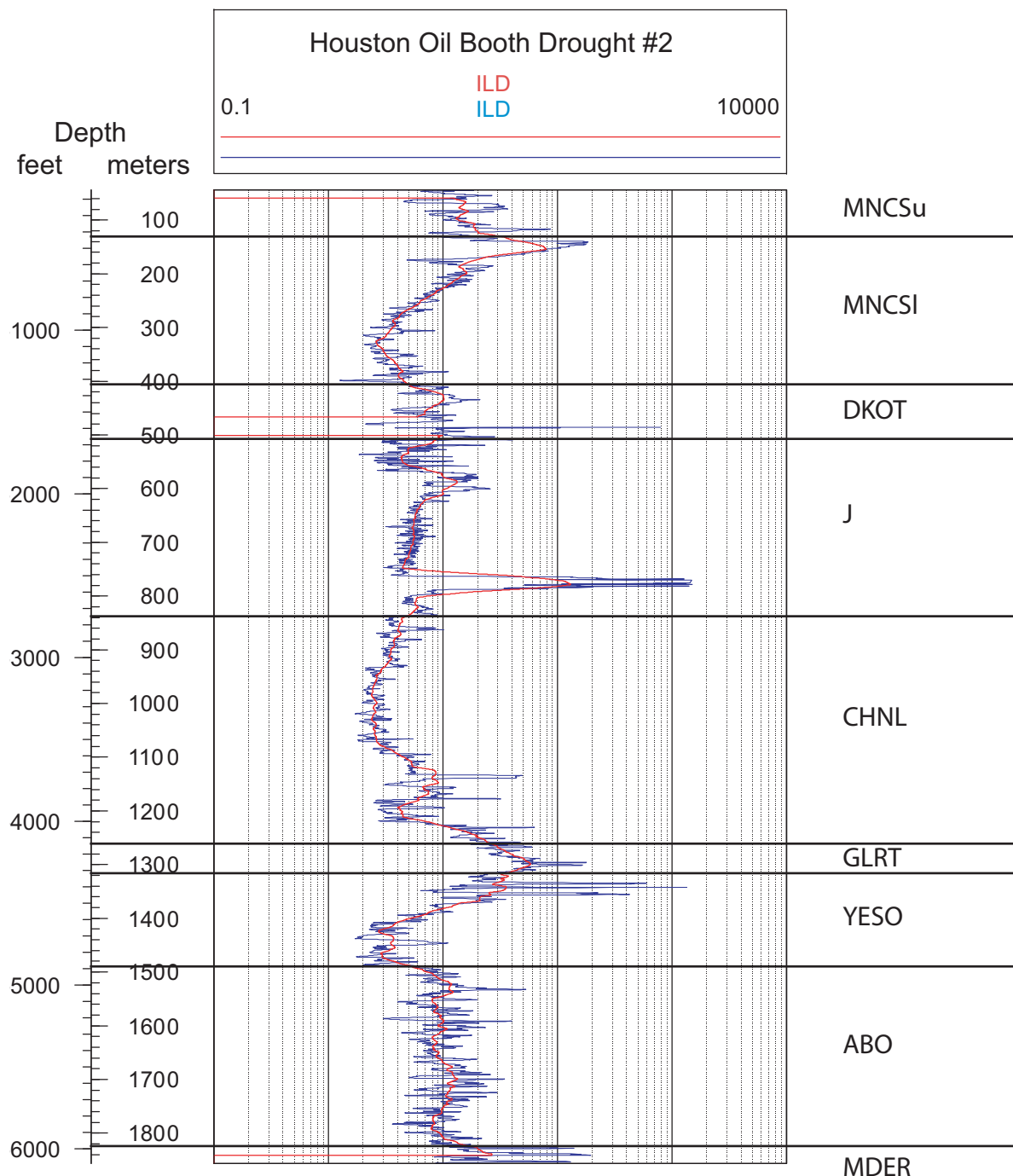


**Figure A44.** Wildcat well Houston Oil & M Booth Drought #2 (Fig. 1, hombdro2 in Tables 1 and A3) deep induction log resistivity (ILD) (blue line) in ohm-m. Red line is 30-m moving average of ILD.

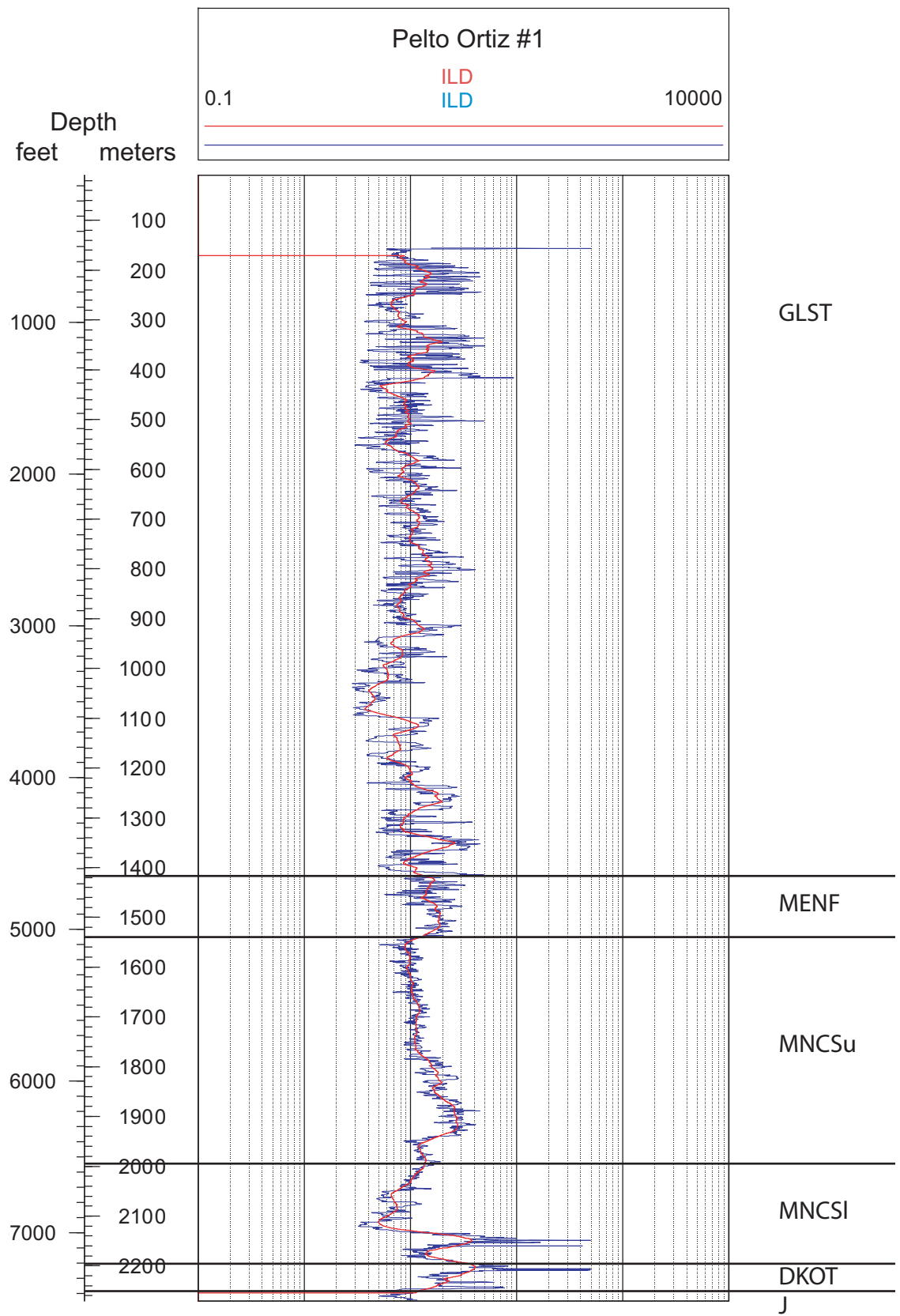


**Figure A45.** Wildcat well Pelto Oil Ortiz #1 (Fig. 2A, pelto\_ortiz1 in Tables 1 and A3) deep induction log resistivity (ILD) (blue line) in ohm-m. Red line is 30-m moving average of ILD.

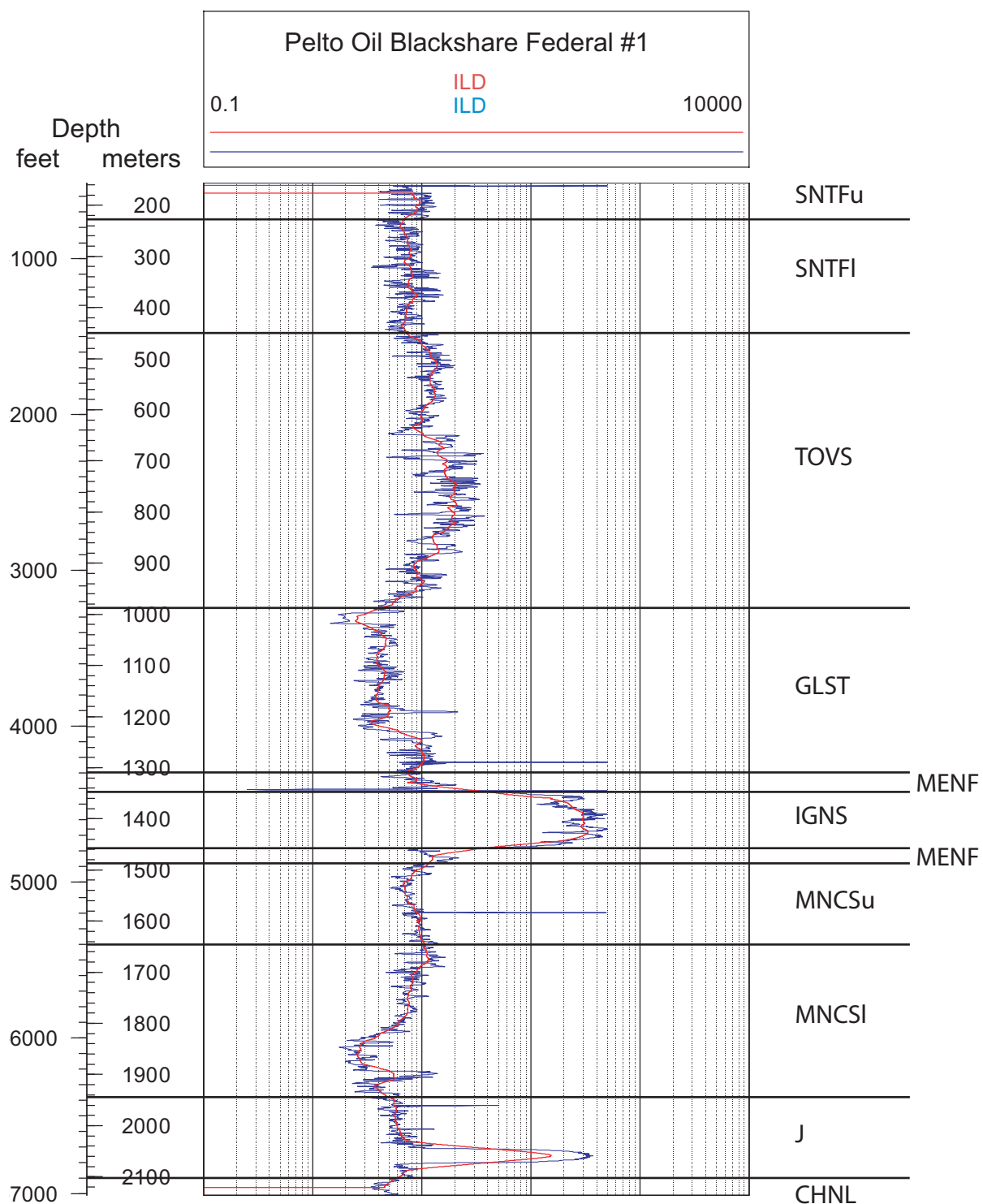


**Figure A46.** Wildcat well Pelto Oil Blackshare Federal #1 (Fig. 2A, pelto\_blk1 in Tables 1 and A3) deep induction log resistivity (ILD) (blue line) in ohm-m. Red line is 30-m moving average of ILD.

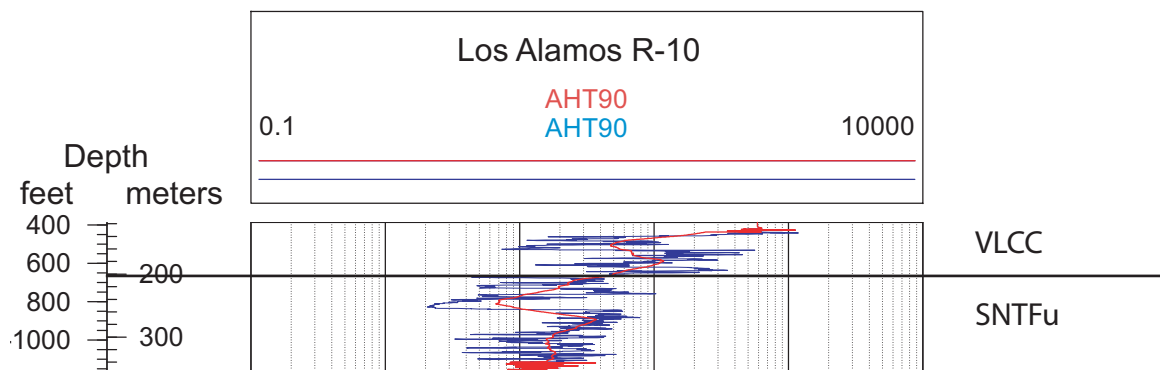


**Figure A47.** Los Alamos National Labs Regional Aquifer well R-10 (Fig. 2A, R-10 in Tables 1 and A3) array induction two foot (0.6 m) resistivity log (AHT90) (blue line) in ohm-m. Red line is 30-m moving average of AHT90.

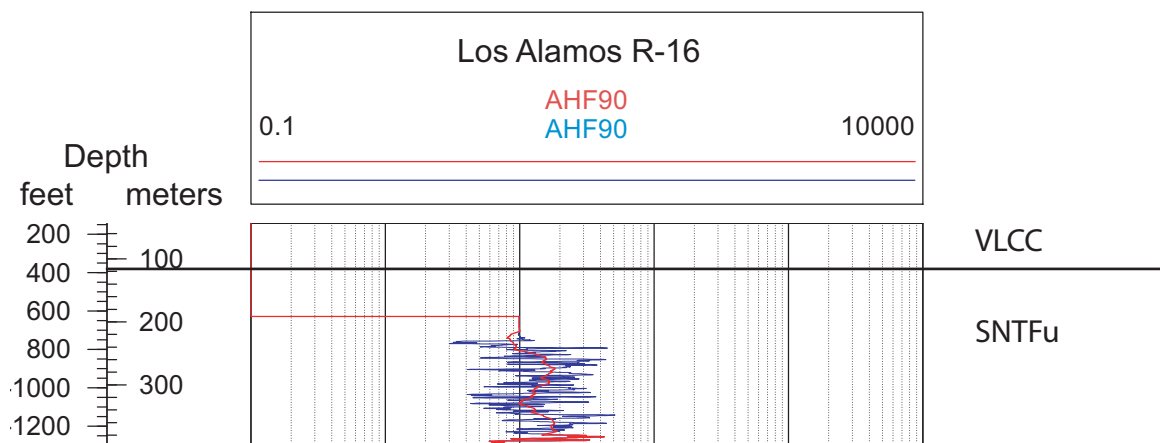


**Figure A48.** Los Alamos National Labs Regional Aquifer well R-16 (Fig. 2A, R-16 in Tables 1 and A3) array induction four foot (1.2 m) resistivity log (AHF90) (blue line) in ohm-m. Red line is 30-m moving average of AHF90.

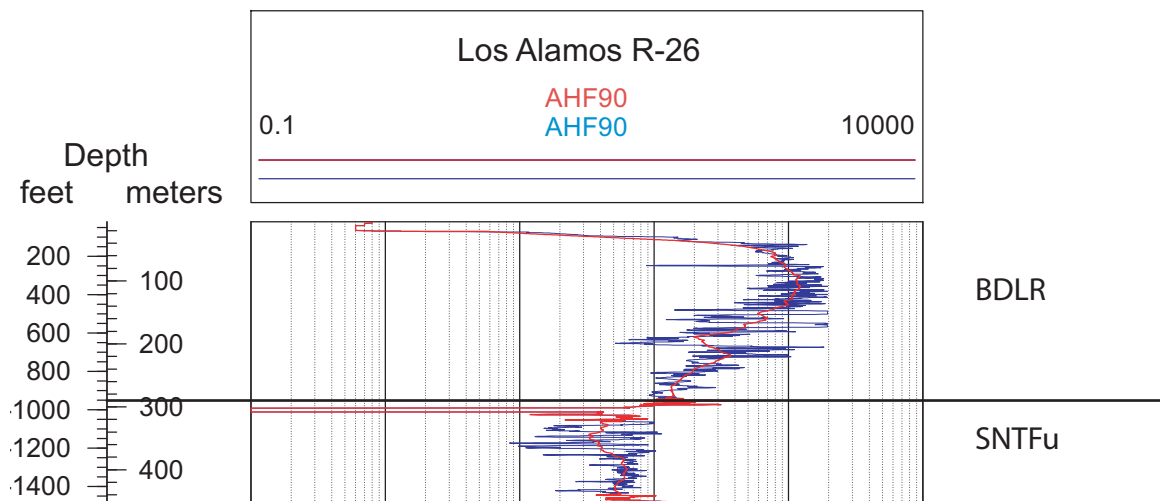


**Figure A49.** Los Alamos National Labs Regional Aquifer well R-26 (Fig. 2A, R-26 in Tables 1 and A3) array induction four foot (1.2 m) resistivity log (AHF90) (blue line) in ohm-m. Red line is 30-m moving average of AHF90.

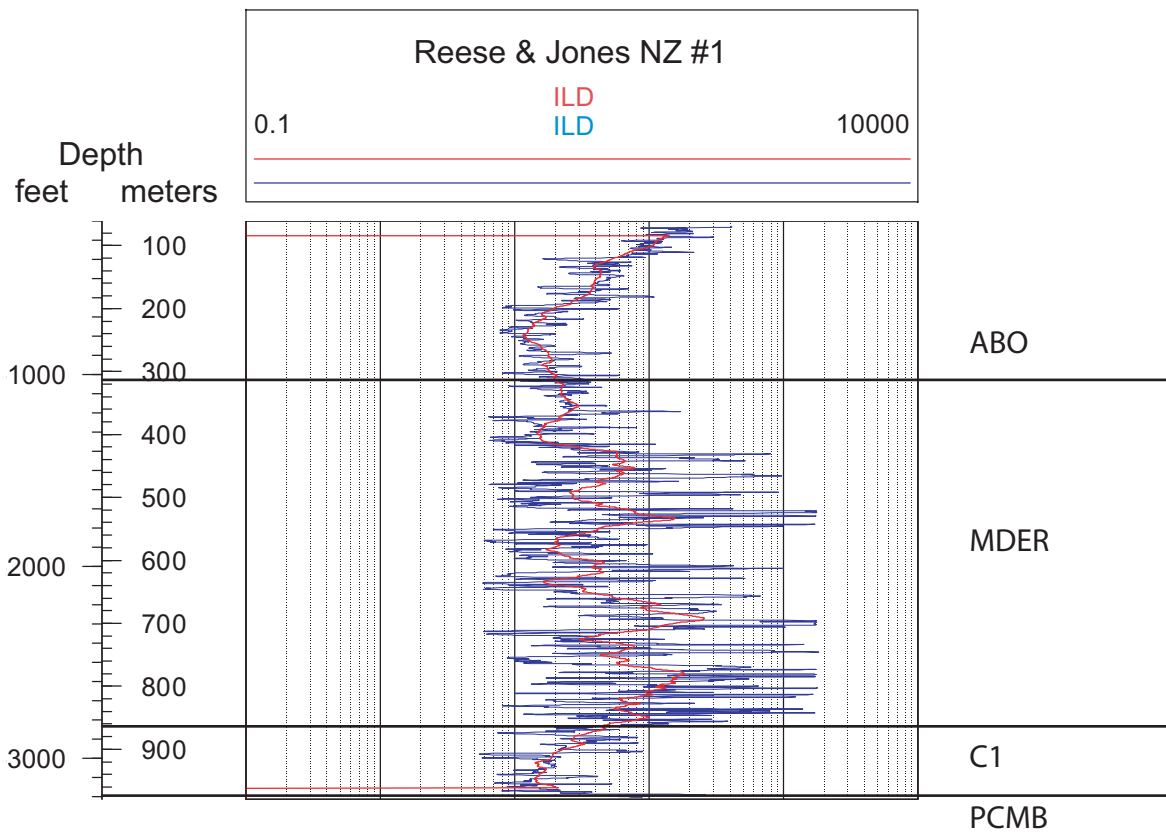


**Figure A50.** Wildcat well Reese & Jones NZ #1 (Fig. 2B, resjonz1 in Tables 1 and A3) deep induction log resistivity (ILD) in ohm-m. Red line is 30-m moving average of ILD.

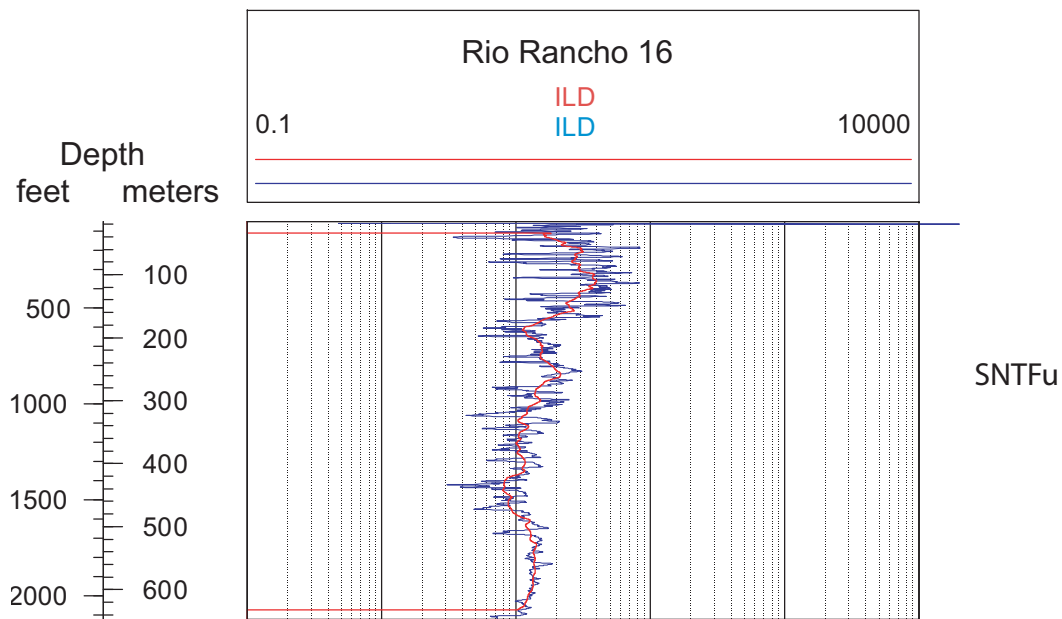


**Figure A51.** Water well Rio Rancho #16 (Fig. 1, RR16 in Tables 1 and A3) deep induction log resistivity (ILD) (blue line) in ohm-m. Red line is 30-m moving average of ILD.

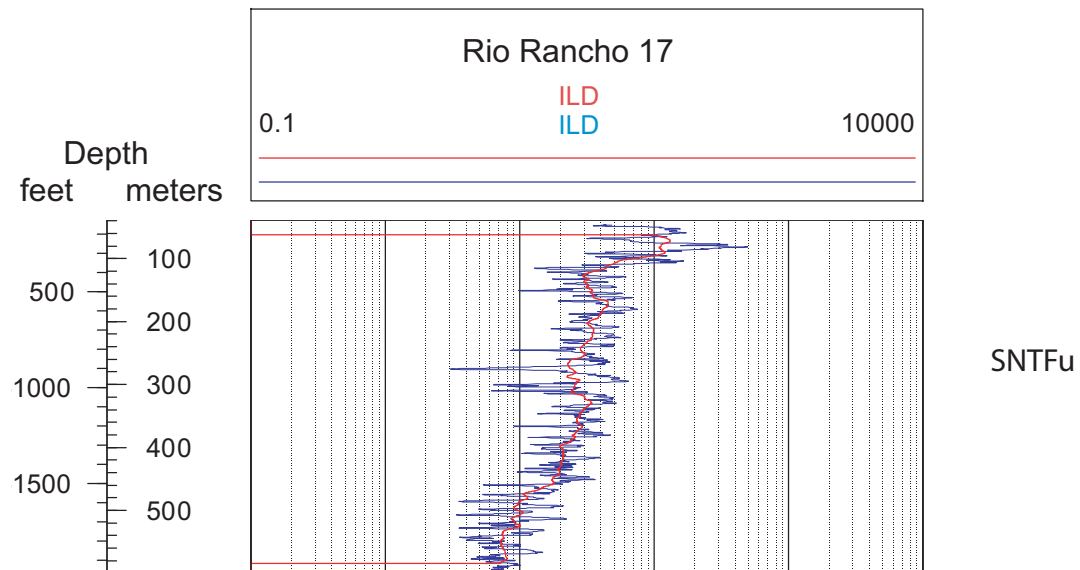


**Figure A52.** Water well Rio Rancho #17 (Fig. 1, RR17 in Tables 1 and A3) deep induction log resistivity (ILD) (blue line) in ohm-m. Red line is 30-m moving average of ILD.

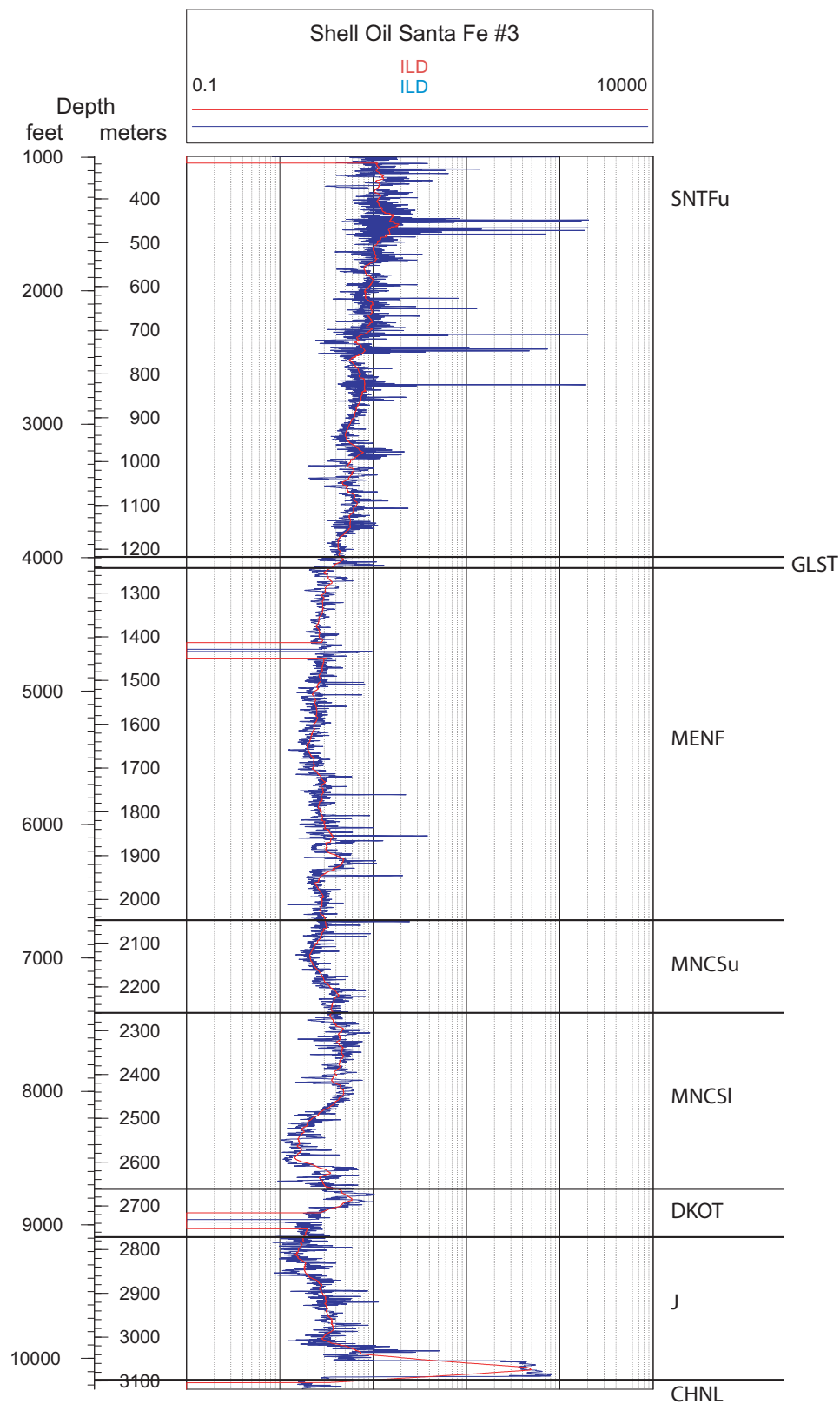


**Figure A56.** Wildcat well Shell Oil Santa Fe Pacific #3 (Fig. 1, shsfp3 in Tables 1 and A3) deep induction log resistivity (ILD) (blue line) in ohm-m. Red line is 30-m moving average of ILD.

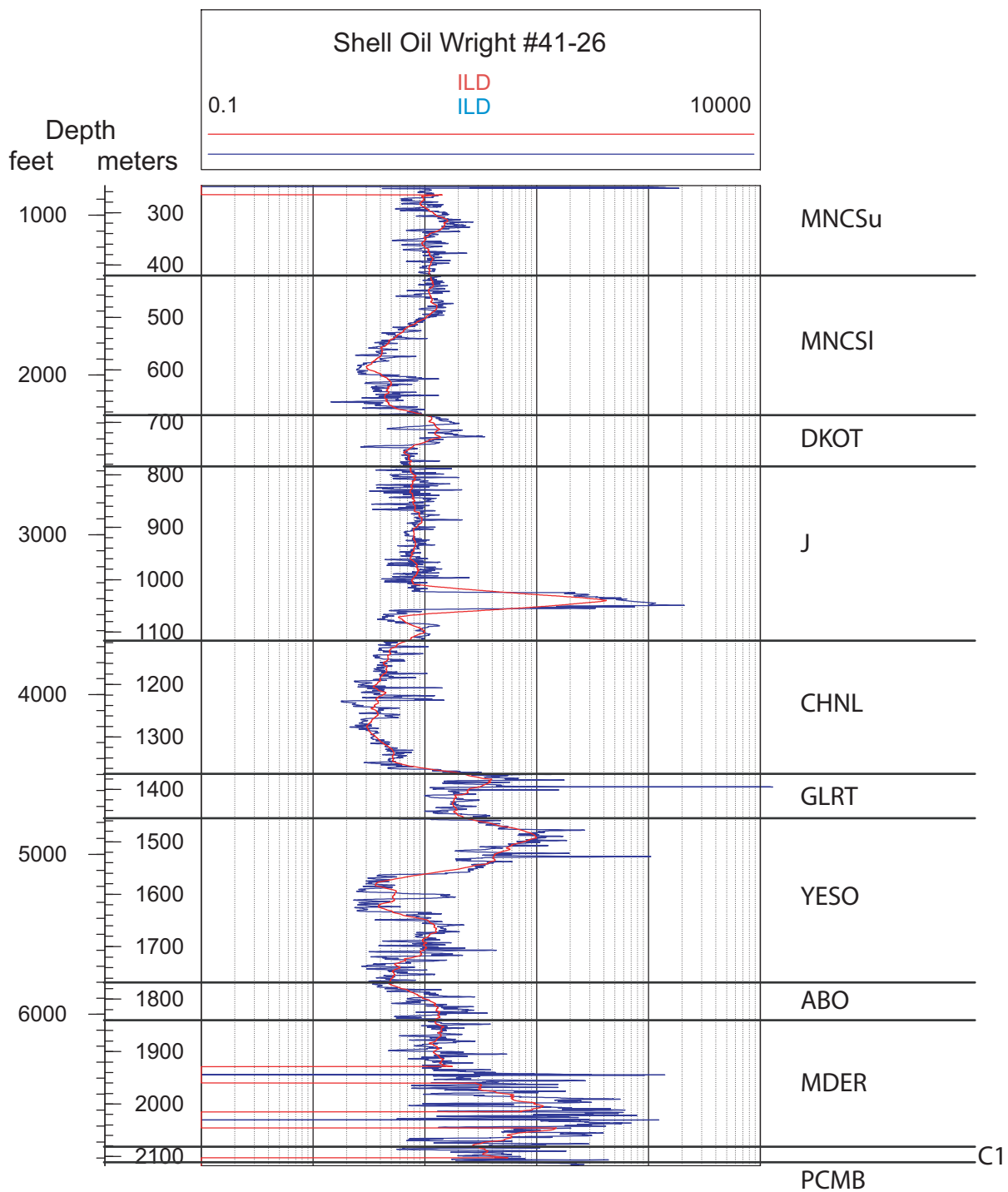


**Figure A57.** Wildcat well Shell Oil Wright #41-26 (Fig. 1, shwrit41 in Tables 1 and A3) deep induction log resistivity (ILD) (blue line) in ohm-m. Red line is 30-m moving average of ILD.

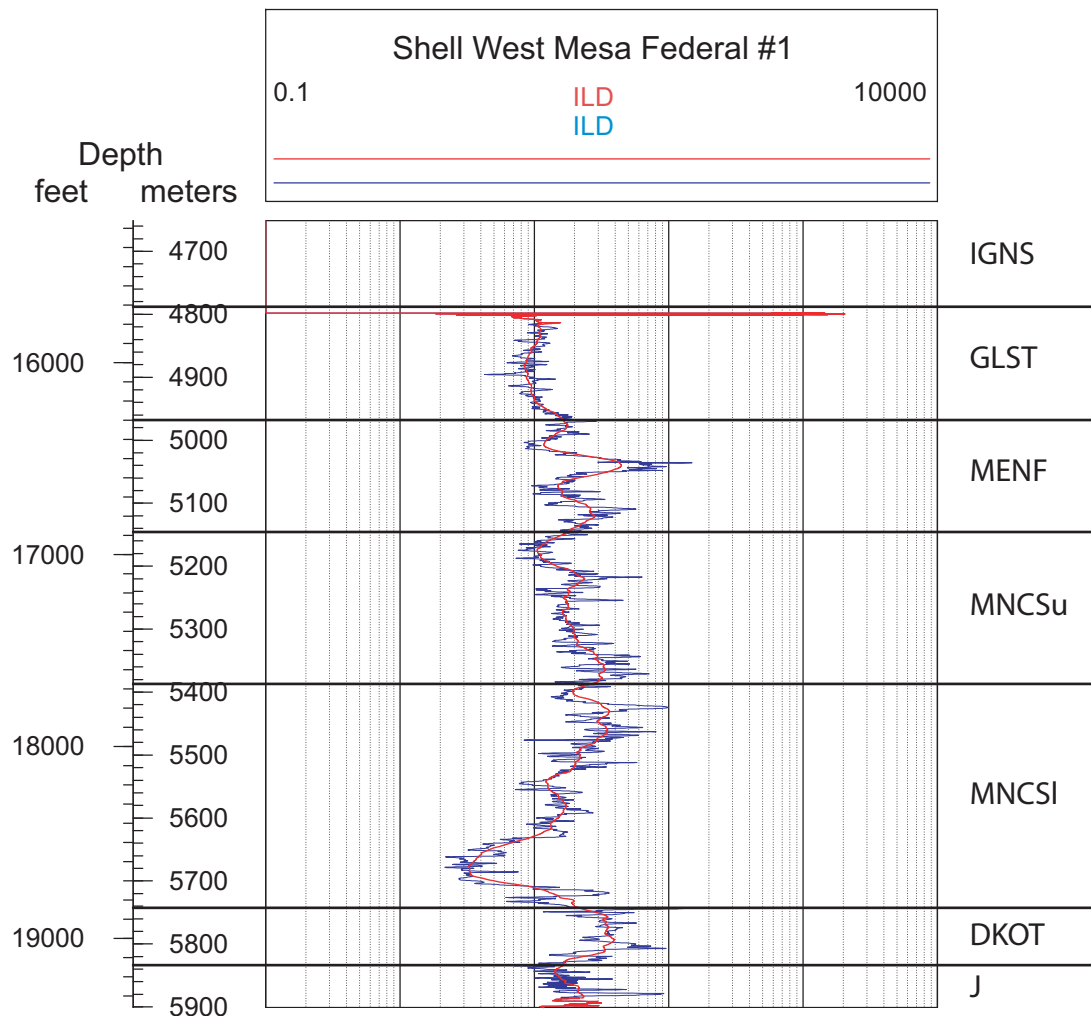


**Figure A58.** Wildcat well Shell Oil West Mesa Federal #1 (Fig. 2B, shelwmf1 in Tables 1 and A3) deep induction log resistivity (ILD) (blue line) in ohm-m. Red line is 30-m moving average of ILD.

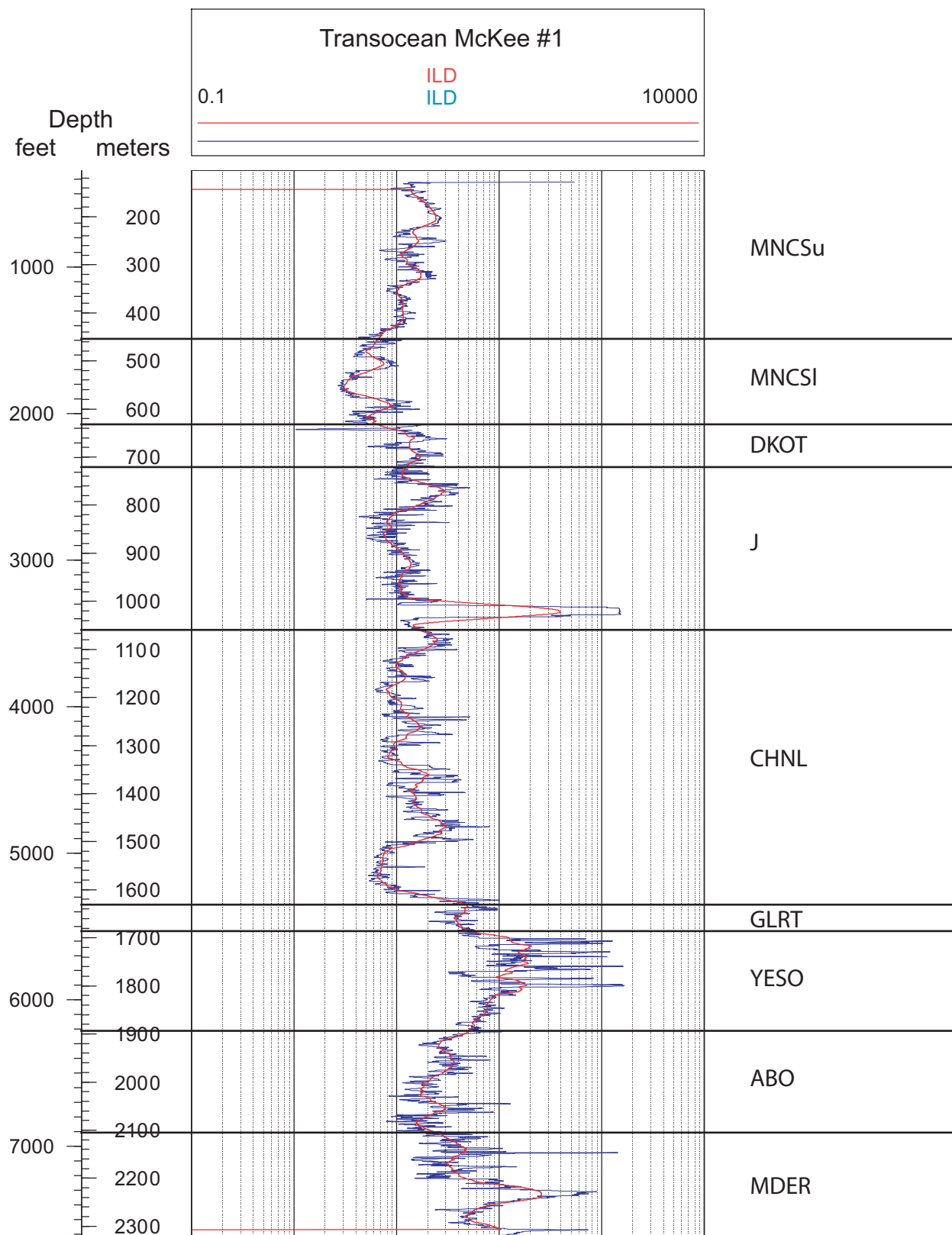


**Figure A59.** Wildcat well Transocean Oil McKee #1 (Fig. 2A, tomckee1 in Tables 1 and A3) deep induction log resistivity (ILD) (blue line) in ohm-m. Red line is 30-m moving average of ILD.

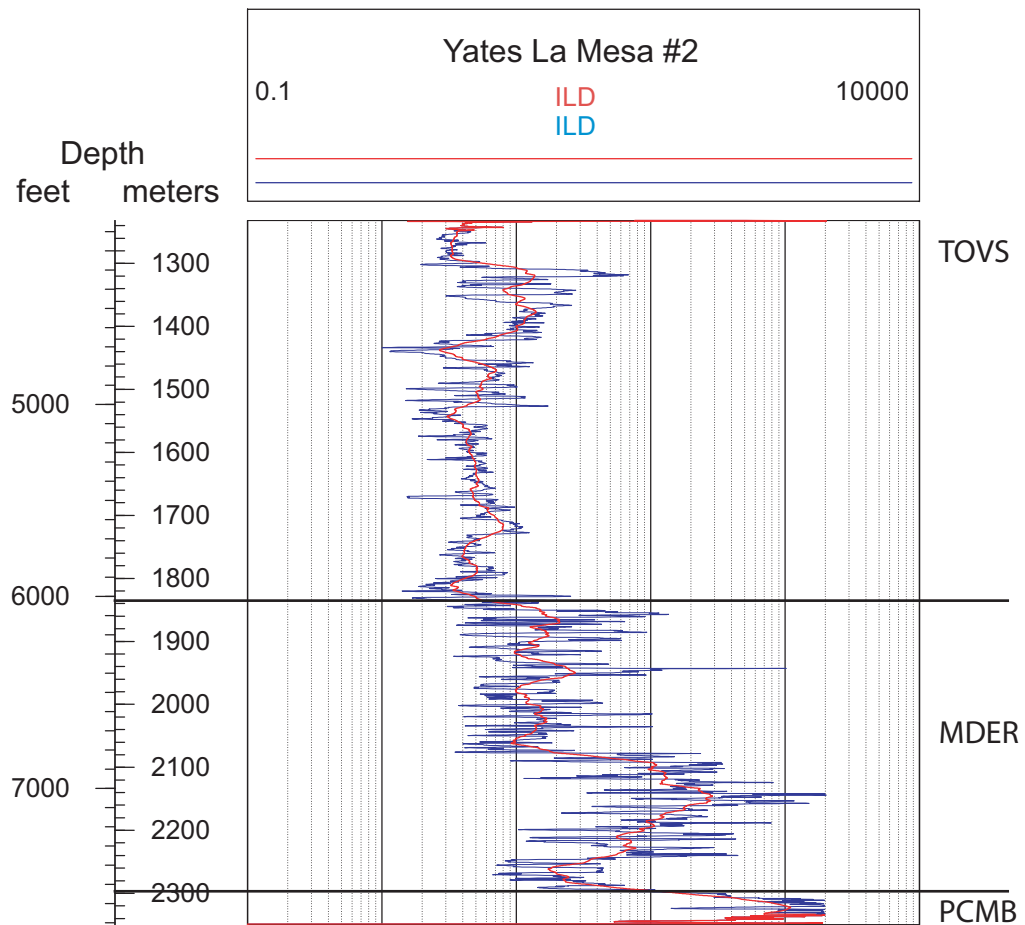


**Figure A60.** Wildcat well Yates Petroleum La Mesa #2 (Fig. 2A, ylamesa2 in Tables 1 and A3) deep induction log resistivity (ILD) (blue line) in ohm-m. Red line is 30-m moving average of ILD.

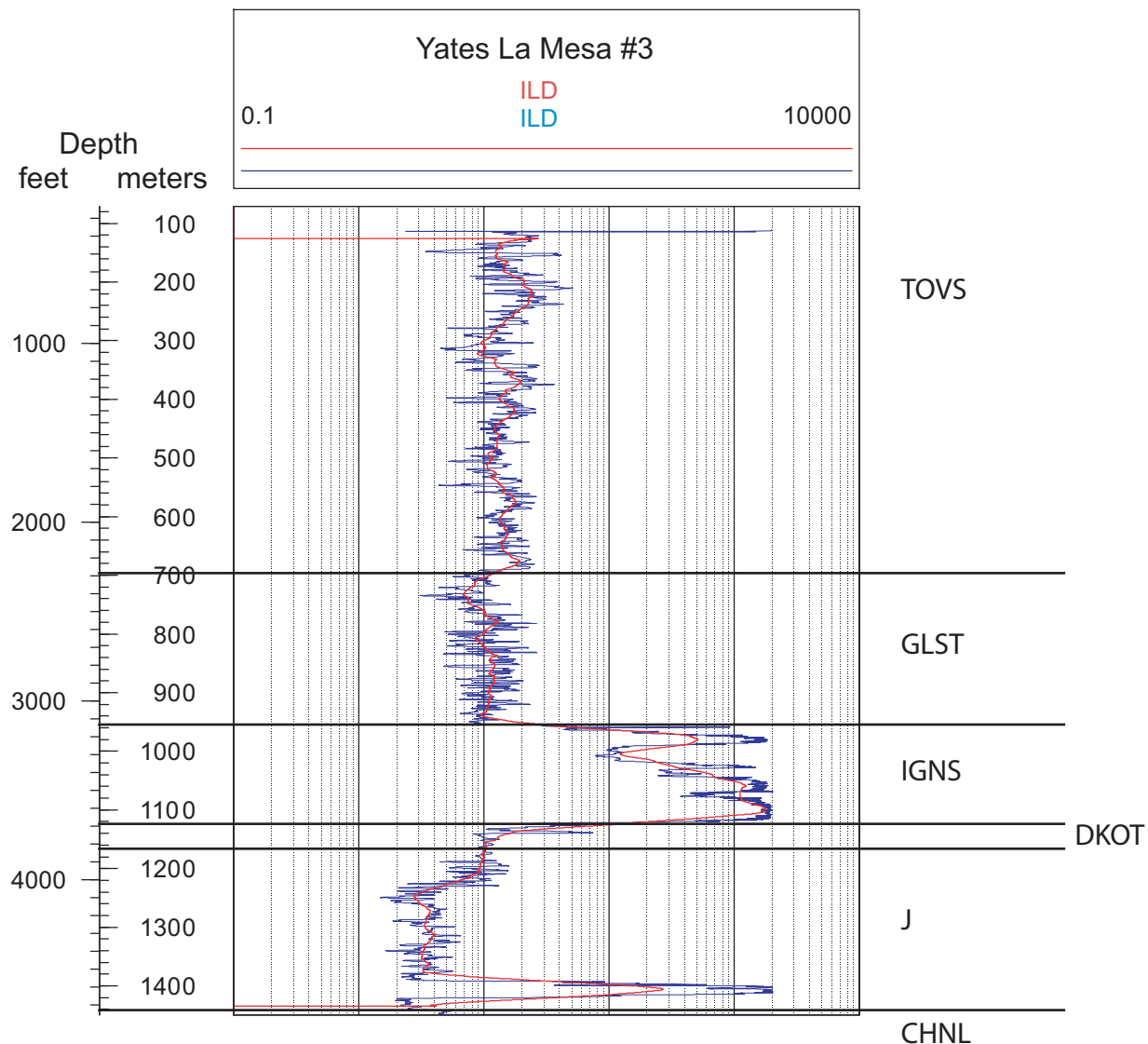


**Figure A61.** Wildcat well Yates Petroleum La Mesa #3 (Fig. 2A, *ylamesa3* in Tables 1 and A3) deep induction log resistivity (ILD) (blue line) in ohm-m. Red line is 30-m moving average of ILD.

## References Cited

- Bayliss, G.S., 1998, Hydrocarbon source facies character of sediments penetrated by Shell Oil Company Shell Oil Company, no. 1 Isleta central well Valencia County, New Mexico (Spot NW NW Sec. 7; T7N; R2E): New Mexico Bureau of Geology and Mineral Resources Open-File Report 449, 59 p.
- Biehler, S., Ferguson, J.F., Baldridge, W.S., Jiracek, G.R., Aldern, J.L., Martinez, M., Fernandez, R., Romo, J., Gilpin, B., Braile, L.W., Hersey, D.R., Luyendyk, B.P., and Aiken, C.L., 1991, A geophysical model of the Española Basin, Rio Grande rift, New Mexico: *Geophysics*, v. 56, no. 3, p. 340-353.
- Black, B.A., and Hiss, W.L., 1974, Structure and stratigraphy in the vicinity of the Shell Oil Co. Santa Fe Pacific No. 1 test well, southern Sandoval County, New Mexico: New Mexico Geological Society, Guidebook 25, p. 365-370.
- Carpenter, R., Borchert, C., and Finch, S., 2004, City of Santa Fe Buckman Well Nos. 10-13 Project, *in* Hudson, M.R., Geologic and Hydrogeologic Framework of the Española Basin --Proceedings of the 3rd Annual Española Basin Workshop, Santa Fe, New Mexico, March 2-3, 2004: U.S. Geological Survey Open-File Report 2004-1093, 32 p.
- Cather, S.M., Connell, S.D., Chamberlin, R.M., McIntosh, W.C., Jones, G.E., Potochnik, A.R., Lucas, S.G., and Johnson, P.S., 2008, The Chuska erg: Paleogeomorphic and paleoclimatic implications of an Oligocene sand sea on the Colorado Plateau: *Geological Society of America Bulletin*, v. 120, p. 13-33.
- Chamberlin, R.M., Jackson, P., and Connell, S.D., 1999, Field logs of borehole drilled for monitoring well at Dome Road site, Canada de Cochiti grant, Sandoval County, New Mexico: New Mexico Bureau of Mines and Mineral Resources Open-file Report 444c, 30 p.
- Connell, S.D., 2006, Preliminary Geologic Map Of The Albuquerque-Rio Rancho Metropolitan Area and Vicinity, Bernalillo And Sandoval County, New Mexico: New Mexico Bureau of Geology and Mineral Resources, Open-File Report 496, ver. 2, 2 pls., scale 1:50,000.
- Grauch, V.J.S., Phillips, J.D., Koning, D.J., Johnson, P.S., and Bankey, V., 2009, Geophysical interpretations of the southern Española basin, New Mexico, that contribute to understanding its hydrogeologic framework: U. S. Geological Survey Professional Paper 1761, 88 pp.
- Hermance, J., and Pedersen, J., 1980, Deep structure of the Rio Grande Rift: A magnetotelluric interpretation: *Journal of Geophysical Research*, vol. 85, no. B7, p. 3899-3912.
- Jiracek, G.R., 1990, Near-surface and topographic distortions in electromagnetic induction: *Surveys in Geophysics*, vol.11, p.163-203.
- Jiracek, G.R., Rodi, W.L., and Vanyan, L.L., 1987, Implications of magnetotelluric modeling for the deep crustal environment in the Rio Grande Rift: *Physics of the Earth and Planetary Interiors*, vol.45, no.2, p.179-192.
- Jones, F.W., and Vozoff, K., 1978, The calculation of magnetotelluric quantities for three-dimensional conductivity inhomogeneities: *Geophysics*, v. 43, no. 6, p. 1167-1175.
- Jupp, D.L.B., and Vozoff, K., 1976, Discussion on "The magnetotelluric method in the exploration of sedimentary basins" (Vozoff, 1972): *Geophysics*, v. 41, no. 2, p. 325-328.
- Kleinfelder, 2005, Final Well R-26 Completion Report, Revision No. 1: Los Alamos National Laboratory, Project No. 37151, Albuquerque, New Mexico, 26 p.

- Kleinfelder, 2006, Final Completion Report, Characterization Wells R-10a/R-10: Los Alamos National Laboratory, Project No. 49436, Albuquerque, New Mexico, 32 p.
- Los Alamos National Laboratory, 2006, Well Rehabilitation Pilot Study Execution Plan: Los Alamos National Laboratory document LA-UR-06-3874, Los Alamos, New Mexico, 37 p.
- Los Alamos National Laboratory, 2008, Completion Report for Well R-25c: Los Alamos National Laboratory document LA-UR-08-5878, Los Alamos, New Mexico, 43 p.
- Lozinsky, R.P., 1988, Stratigraphy and sedimentology of the Santa Fe Group in the Albuquerque Basin, north-central New Mexico [Ph.D. Thesis]: New Mexico Institute of Mining and Technology, Socorro, New Mexico, 298 p.
- Lozinsky, R.P., 1994, Cenozoic stratigraphy, sandstone petrology, and depositional history of the Albuquerque Basin, central New Mexico, in Keller, G.R., and Cather, S.M., eds., Basins of the Rio Grande Rift; structure, stratigraphy, and tectonic setting: Special Paper - Geological Society of America, vol. 291, p. 73-81.
- Mackie, R.L., Madden, T.R., and Wannamaker, P.E., 1993, Three-dimensional magnetotelluric modeling using difference equations; theory and comparisons to integral equation solutions: Geophysics, vol. 58, no. 2, p. 215-226.
- Mackie, R.L., Rieven, S., and Rodi, W., 1997, Users manual and software documentation for two-dimensional inversion of magnetotelluric data: GEOTOOLS User's Guide RLM2DI Supplement, 10 p.
- McLin, S.G., 2005, Analyses of the PM-2 Aquifer Test Using Multiple Observation Wells: Los Alamos National Laboratory report LA-14225-MS, Los Alamos, New Mexico, 73 p.
- Quesada, R.M., 2004, Continuous magnetotelluric profiling across the La Bajada Fault, Rio Grande Rift, New Mexico: San Diego State University, Thesis (M.S.), 214 p.
- Rodi, W., and Mackie, R.L., 2001, Nonlinear conjugate gradients algorithm for 2-D magnetotelluric inversion: Geophysics, v. 66, no. 1, p. 174-187.
- Rodriguez, B.D., and Sawyer, D.A., (this volume), Geophysical constraints on Rio Grande rift structure and stratigraphy from magnetotelluric models and borehole resistivity logs, northern New Mexico, in Grauch, V.J.S., and Hudson, M.R., eds., New perspectives on the Rio Grande rift: From Tectonics to Groundwater: Geological Society of America Special Paper.
- Romo, J.M., Gomez-Treviño, E., and Esparza, F.J., 1999, An invariant representation for the magnetic transfer function in magnetotellurics: Geophysics, v.64, no. 5, p. 1418-1428.
- Siripunvaraporn W., Egbert, G., Lenbury, Y., and Uyeshima, M., 2005, Three-dimensional magnetotelluric: data space method: Physics of the Earth and Planetary Interiors, v. 150, p. 3-14.
- Vozoff, K., 1991, The magnetotelluric method, in Nabighian, M.N., ed., Electromagnetic methods in applied geophysics, v. 2, Application, part B: Society of Exploration Geophysicists, Tulsa, Oklahoma, p. 641-711.
- Wannamaker, P.E., Hohmann, G.W., and Ward, S.H., 1984, Magnetotelluric responses of three-dimensional bodies in layered earths: Geophysics, v. 49, no. 9, p. 1517-1533.
- Wannamaker, P.E., Stodt, J.A., and Rijo, L., 1985, PW2D—finite element program for solution of magnetotelluric responses of two-dimensional earth resistivity structure (User documentation): Salt Lake City, Utah, Earth Science Laboratory, University of Utah Research Institute, 40 p.

- Wannamaker, P.E., Doerner, W.M., Stodt, J.A., Sodergren, T.L., and Rodriguez, B.D., 2002, Analysis of magnetotelluric profile data from the Ruby Mountains metamorphic core complex and southern Carlin Trend region, Nevada: U.S. Geological Survey Open-File Report 02-214, 50 p.
- Williams J.M., and Rodriguez, B.D., 2003a, Magnetotelluric data release across the Hubbell Springs fault area, Middle Rio Grande Basin, New Mexico: U.S. Geological Survey Open-File Report 03-115, 101 p.
- Williams, J.M., and Rodriguez, B.D., 2003b, Magnetotelluric data in the southwest Española basin, northern New Mexico: U.S. Geological Survey Open-File Report 03-199, 128 p.
- Williams, J.M., and Rodriguez, B.D., 2005a, Magnetotelluric data in the Española Basin, west of Santa Fe, New Mexico: U.S. Geological Survey Open-File Report 2005-1037, 263 p.
- Williams, J.M., and Rodriguez, B.D., 2005b, Magnetotelluric data along the Pajarito fault in the Española Basin, west of Santa Fe, New Mexico: U.S. Geological Survey Open-File Report 2005-1054, 173 p.
- Williams, J.M., and Rodriguez, B.D., 2006, Magnetotelluric data collected near geophysically logged boreholes in the Española and Middle Rio Grande Basins, New Mexico: U.S. Geological Survey Open File Report 2006-1120, 126 p.